Dye Sensitised Solar Cells:
A Computational Approach

Conn O'Rourke

A Thesis submitted for the degree of

Doctor of Philosophy

London Centre for Nanotechnology

Department of Physics & Astronomy

UCL

2013

I, Conn O'Rourke, confirm that the work presented in this thesis is my own. Where information has been derived from other sources, I confirm this has been indicated in the thesis.

Acknowledgements

Firstly I would like to express sincere thanks to David Bowler, my supervisor, for the guidance and support he has given me throughout this work. Sharing an office, and a coffee machine, with Umberto Terranova has been a pleasure and I'd like to thank him for entertaining discussions on the subject of dye sensitised solar cells, amongst many other things. I would also like to thank Lianheng Tong, for always being willing to help with CONQUEST, along with Yoshitaka Tateyama, Masato Sumita and Chunping Hu for an interesting time in Tsukuba.

Finally I would like to thank Beth, for always being there for me.

Abstract

Dye sensitised solar cells (DSSCs) mimic charge excitation and transfer processes found in natural photosynthesis to directly convert sunlight into electricity. Combining easy assembly with relatively cheap materials they offer a potentially cost effective solution to our energy requirements. Numerous physical processes are at work within a DSSC and the underlying complexity of these competing processes has meant that, despite considerable research effort, advances in obtaining a viable device efficiency have stagnated.

The aim of this thesis is to examine, by density functional theory calculations, some of the processes at work in DSSCs with the motivation being to provide insight that informs the design of more efficient devices by experimentalists. Our calculations study some of the key factors affecting device efficiency, in particular the interaction of binding moieties with TiO_2 surfaces, the role intrinsic and extrinsic defects have in defining the properties of semiconductors, the molecular design of sensitising dyes and the effect this has on both dye-dye and dye-semiconductor interactions. Finally we implement and test the excited state formalism of time dependent density functional theory (TDDFT) within the linear scaling DFT code CONQUEST, allowing excited state properties of large systems to be examined computationally. Our approach propagates the density matrix in real time (RT-TDDFT), and finally we use our implementation to model the real time response of TiO_2 clusters and dyes to external electric fields.

Contents

List of Publications

- C. O'Rourke and D. R. Bowler, "*DSSC Anchoring Groups: A Surface Dependent Decision*", In preparation
- C. O'Rourke and D. R. Bowler, "*Linear Scaling TDDFT in CONQUEST*", In preparation
- C. O'Rourke and D. R. Bowler, "*Intrinsic Oxygen Vacancy and Extrinsic Aluminium Dopant Interplay: A Route to the Restoration of Defective TiO_2*", In preparation
- K. Sodeyama, M. Sumita, C. O'Rourke, U. Terranova, A. Islam, L. Han, D. R. Bowler, and Y. Tateyama, "*Protonated Carboxyl Anchor for Stable Adsorption of Ru N749 Dye (Black Dye) on a TiO_2 Anatase (101) Surface*", J. Phys. Chem. Lett., 3 (2012), 472-477
- C O'Rourke and D. R. Bowler, "*Adsorption of Thiophene-Conjugated Sensitisers on TiO_2 Anatase (101)*", J. Phys. Chem. C, 2010, 114(47), 20240

List of Figures

List of Tables

Chapter 1

Introduction

Mimicking nature is no mean feat. Billions of years of trial and error underly an elegance to some of nature's problem solving that can bely the complexity of the processes involved. Picking apart these complex processes and understanding how nature works is at best challenging. Artificially replicating them is often considerably more so.

However, technological advances can be made when scientists and engineers take their cues from nature. Some examples of such *biomimicry* include self-cleaning super-hydrophobic surfaces inspired by the properties of lotus leaves [4, 5], carbon dioxide capture utilising the carbonic anhydrase enzymes used in biological respiration processes[6] and irridescent nanostructures mimicking those of butterfly wings[7].

Photosynthesis is one of the most fundamental of nature's processes. Increasing global energy requirements coupled with the environmental impact of fossil fuel combustion provide an excellent motivation for us to replicate it. Copying nature in this way would allow us to harness power from one of the most readily available sources of clean energy, the sun.

Natural photosynthesis involves the harvesting of light energy in a system of chlorophyll antenna by excitation of electrons. An electron transfer chain then provides efficient charge separation[8]. Dye sensitised solar cells (DSSCs) mimic this efficient charge excitation and transfer process in order to directly convert sunlight into electricity.

While first and second generation solar cells, based on crystalline silicon and thin film semiconductors, offer higher efficiencies ($\sim$ 20-30[9]), DSSCs combine easy assembly with relatively cheap materials to offer a potentially cost-effective solution to our energy requirements. However, wide-scale economic viability requires a balance between cost and the resulting device efficiency that, for the moment, is precluded by the current technology in the

field.

Numerous physical processes are involved in DSSC operation, such as molecule surface interaction, chromophore aggregation, the character of semiconductor defects, interactions at semiconductor solution interfaces and electron transfer, which have a range of applicability beyond that of DSSCs. While this makes them interesting candidates for investigation in their own right, it is the optimisation of the many properties of DSSCs to improve efficiency that provides the main driving force behind a very active research field.

Despite considerable interest in DSSCs, and much research effort, only small efficiency improvements have been made over the past 20 years; the current benchmark efficiency stands at 12.3% [10], while in 1993 the benchmark device already had an efficiency of 10% [11]. Computational processing power has increased dramatically over this period, and with it so too has the scope for utilizing computational physics to both predict and elucidate the physical behaviour of real systems.

In order to aid design and drive forward the efficiency of DSSC devices a deeper understanding of the physical processes at work is required. Presented in this thesis are computational studies examining some of the fundamental mechanisms that govern the efficiency of dye sensitised solar cells, with the aim of offering insight to experimentalists working in the field. Several key processes are at work in a DSSC and in particular the first half of the thesis focuses on some key themes not only in dye sensitised solar cell design but also in much of nanotechnology. These are the effect of molecular design on both interactions with semiconductor surfaces and molecular aggregation, and the role intrinsic and extrinsic defects have in defining the properties of semiconductors. Electron response and transfer has a major role in defining the properties of a material, and therefore its potential usefulness in any particular device. Computational modelling of electron excitations and transfer is extremely demanding and it is to this that the attention of the latter half of this thesis turns. Firstly implementing a methodology by which the study of the optical properties and transfer of electrons may be studied in large physically realistic systems, and finally using this implementaion to characterise and model the behaviour of electrons in semiconductor nanoclusters of direct relevance to dye sensitised solar cells.

In this chapter a brief review of some of the major research on dye sensitised solar cells is presented, along with an outline of the operating principles and the factors governing cell efficiency. Finally an overview of the remainder of the thesis is given.

1.1 Dye Sensitised Solar Cells

Optical absorption of wide band gap semiconductors is limited to the ultraviolet part of the solar irradiance spectrum. Sensitising these semiconductors to photons beyond the wide band gap range provides energetic access to the majority of photons arriving at the earth's surface from the sun. Early attempts to increase the sensitivity of semiconductor oxides employed flat single crystals, sensitised by the adsorption of perylene molecules [12].

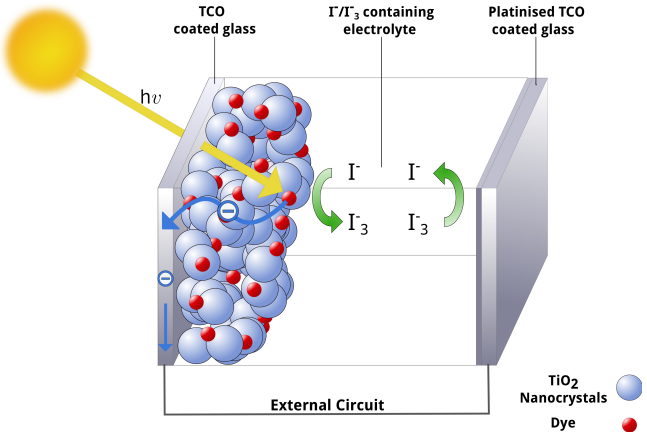

Figure 1.1: Typical dye sensitised solar cell schematic

Employing a sintered nanocrystalline TiO_2 electrode in 1991, O'Reagan and Grätzel dramatically increased the surface area and consequent dye molecule take up of the semiconductor[13]. Resulting high efficiencies of the device, as high as 7.9%, provided considerable motivation for further work in the field and it is generally taken as being the inception of modern dye sensitised solar cells. Indeed the majority of the current research on DSSCs continues to employ the main design traits of this O'Reagan/Grätzel cell.

A simple schematic for a typical DSSC can be seen in figure 1.1, in which a network of sintered nanocrystalline TiO_2 particles are screen printed onto a transparent conducting oxide (T.C.O.) front contact, such as fluorine doped SnO_2[14]. Upon the TiO_2 a dye, that absorbs strongly in the visible to near infrared part of the solar spectrum, is adsorbed. A platinum coated T.C.O. is used as a back contact electrode to seal the cell, within which an electrolyte is placed. Generally the electrolyte is composed of an iodide/tri-iodide couple in an acetonitrile containing solution.

Current generation by a DSSC proceeds by the photoexcitation of the adsorbed chromophore, followed by the rapid electron injection from its valence band into the conduction

band of the semiconductor. Electrons then percolate through the semiconductor network to be collected at the T.C.O. front contact. Electron collection at the front contact produces a flow of charge which passes through some external circuit to the T.C.O. back contact. I_3^- present in the electrolyte is then reduced to I^- by electron transfer from the back contact. Regeneration of the oxidised dye, and the complete cell, by the electrolyte proceeds by the conversion of I^- ions back to I_3^-.

Nanocrystalline TiO_2 sensitised by Ruthenium based dyes and utilsing an iodide/tri-iodide electrolyte have, up until recently, provided the benchmark efficiencies for DSSCs. Record efficiencies have been recorded with the so called black dye[15], the N3 dye[16] and its closely related doubly deprotonated form N719[17], as well as forms functionalised with extended ligands such as C101[18], all of which are based on Ruthenium. However a vast array of materials have been put to use in DSSCs, with numerous different dyes, electrolytes, electrode morphologies and co-adsorbants. In the next section we discuss device efficiency, and some of the factors affecting it along with several of the more recent developments and potential strategies for increasing it (for a more detailed review see for example [19]). It is important to remember that although the physics involved in DSSCs will, in general, have many common traits, given the breadth of materials used there will inevitably be fundamental working differences and it is important to consider each on a case by case basis. Computation can play a fundamental role in this respect, allowing the screening of potential materials for desirable characteristics *before* being used in experiment as well as discerning the physics at work in functioning DSSCs.

1.2 DSSC Efficiency

Cell conversion efficiency is measured as the ratio of the product of the open circuit voltage, V_{OC} with the short circuit current density, J_{SC} and the fill factor, FF to the total incident solar power:

$$\eta = \frac{V_{oc} J_{sc} FF}{P_{in}} \tag{1.1}$$

Open circuit voltage is the difference between the quasi Fermi energy of the TiO_2 electrode and the redox potential of the electrolyte (as seen in figure 1.2) and short circuit current density is that generated when there is zero load resistance. J_{SC} is calculated by integrating the incident

photon to current efficiency, IPCE, with the solar spectrum. IPCE is calculated as:

$$\mathrm{IPCE}(\gamma) = \mathrm{LHE}(\gamma) \times \Phi_{\mathrm{inj}} \times \eta_c \tag{1.2}$$

where $\mathrm{LHE}(\gamma)$ is the light harvesting efficiency for a particular wavelength, Φ_{inj} is the injection efficiency and η_c is the charge collection efficiency.

The fill factor gives some measure of the actual working power out with respect to the maximum theoretical power output, and is simply the ratio between the product of maximum operational voltage and current density with the product of V_{OC} and J_{SC}.

1.2.1 Charge Transfer

Many factors will affect the efficiency of a DSSC, not least of these are the charge dynamics within the cell. Several distinct charge transfer processes are at work, some of which are summarised in figure 1.2. Even from this simple schematic it is evident that charge transfer in dye sensitised solar cells is extremely complicated. Here we briefly summarise only a few key points (for fuller reviews see [20, 21]).

Desirable forward charge transfer processes include the dye photo-excitation, electron injection from the dye excited state into the TiO_2, charge collection in the TiO_2 electrode, reduction of the electrolyte and subsequent regeneration of the dye. In competition with these are undesirable, deleterous processes of non-radiative decay and quenching of the excited chromophore, recombination of electrons from the TiO_2 with the dye and the interception of the injected electrons by the electrolyte. Direct competition exists between these forward and deleterous transfer processes, and the materials used will define the relative rates and the efficiency of the charge transfer mechanisms, and therefore of the cell.

For example, from equation (1.2) it can be seen that the efficiency of charge injection from the dye excited state will directly affect the IPCE, and therefore the J_{SC}. Efficient electron injection from the dye to the titania electrode will proceed provided that the rate of injection is large relative to the rate of excited state decay and other quenching processes. Electron injection rates will be dependent on several factors, such as the driving force provided by injection overpotential shown in figure 1.2, the coupling between the dye excited state and the TiO_2 acceptor states and the density of the acceptor states. Each of these properties can be tuned with careful selection of materials.

Highlighting the role device materials have on charge injection is the extensive number of dyes used, which can have fundamentally different characters. Even among very similar dyes charge injection can differ significantly, with the classic example being the N3 dye and

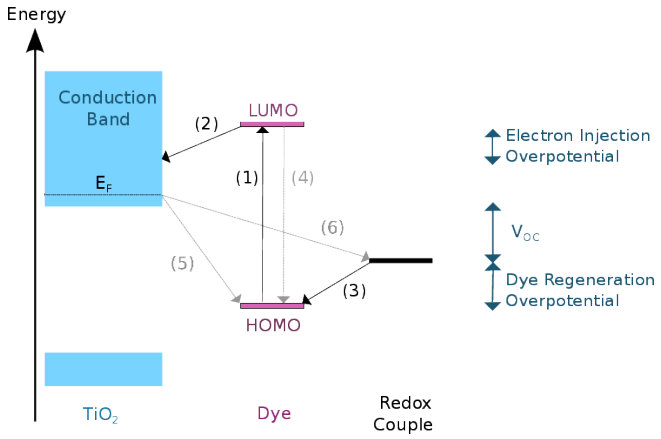

Figure 1.2: **DSSC energy schematic**: Schematic of selected charge transfer processes in a DSSC, with the Fermi energy (E_F) and the open-circuit voltage (V_{OC}) labelled. Desirable processes are illustrated by black arrows: (1) Photo-excitation, (2) Injection, (3) Regeneration. Undesirable processes adversely affecting the cell efficiency are illustrated by grey dashed arrows: (4) Non-radiative decay, (5) Recombination, (6) Interception.

its closely related doubly deprotonated salt N719. N719 has been reported to have a 30-fold increase in injection time compared to N3, due to the effect of protons from the carboxylic groups of N3 on the TiO_2 conduction band[22]. Despite the increased injection time, N719 provides higher efficiencies due to an increase in V_{OC}[23].

A vast range of dye structures will also lead to very different intermolecular interactions on the semiconductor surface. A tendency of organic molecules to form aggregates, for example, can have a significant bearing on the device efficiency. Formation of aggregates has been shown to reduce injection efficiency, due to an increase in quenching pathways; for example in squarine dyes a Förster like resonant energy transfer leads to singlet-singlet exciton annihilation in aggregates[24, 25]. However in some cases the formation of aggregates can lead to efficiencies equivalent to or better than in monomer form [26, 27, 28], hinting that work is needed in order to understand fully the role of aggregates in DSSCs and providing an obvious role for computational work to broaden understanding. Routes have been taken to reduce aggregation in sensitisers, such as design of non-planar dyes and addition of co-adsorbants. Co-adsorbants have been shown in many cases to increase device efficiencies, but also add further considerations to an already complicated device mechanism. Addition of a popular co-adsorbant, chenodeoxycholate, for example can shift the conduction band of the electrode, resulting in an increased V_{OC}, but also to an increase the rate of recombination[29].

Similarly to the competition between injection and excited state decay, efficient regeneration will proceed provided that the rate of recombination of injected electrons is slow relative to that of dye regeneration. Recombination is reported as being directly linked to the electron density in the electrode, however other factors can also have an impact such as the addition of co-adsorbants[29], dye structure [30, 31], defective states in the TiO_2 electrode[32, 33] and the addition of dopants [34, 35].

1.2.2 Dye Design & Optical Response

Optical response of sensitising dyes will influence the short-circuit current density, J_{SC}, as from equation (1.2) we can see that the IPCE depends directly upon the light harvesting efficiency at any given wavelength. Efficient Ruthenium based sensitisers such as N3 and N719 adsorb over a wide range ($\sim$ 350-700 nm.), up to the near infrared part of the spectrum where absorption quickly tails off[16, 17]. Low molar extinction coefficients of these Ruthenium dyes[36, 37] coupled with this low absorption in the infrared part of the solar spectrum motivates the search for new sensitising dyes[38]. Broadening the absorption spectra would increase the IPCE, while using dyes with increased molar extinction coefficients allow thinner electrodes to be used[39], which can improve the charge collection efficiency.

Organic dyes have two main advantages over their Ruthenium based counterparts, much higher molar extinction coefficients and a lack of expensive noble metals[19, 40, 41]. However, organic chromophores will typically have a more narrow absorption spectrum[19].

Molecular design of sensitisers forms one of the main avenues of research in the field of DSSCs, with considerable effort put into designing dyes with suitable properties. For example, engineering chromophores with intramolecular charge transfer can produce enhanced coupling of the excited state and the substrate. Typically this has been achieved through the separation of an electrophobic donor and electrophilic acceptor group within the dye by way of a π linker, in D-π-A structures[19, 42, 43]. Dye design in this manner can also be used to control the optical response, with extension of the π linker used to induce a red-shift in absorption spectra, and a subsequent increase in J_{SC}[44]. Dye design also forms one of the pathways taken to reduce aggregation in sensitisers, by the design of non-planar dyes exploiting steric hindrance to prevent overpacking on the TiO_2 surface.

1.2.3 Current Developments

Many different approaches to improving cell efficiency have been explored, and in this subsection we briefly describe a select few of the current avenues of research.

One of the most obvious places to start with altering device properties is with the electrode. TiO_2 is the predominant semiconductor used in dye sensitised solar cells, and the properties of its two most stable polymorphs, rutile and anatase, are therefore extremely important. Controlling the size, structure and the ratio of exposed surfaces provides one of the areas of research for achieving increased cell efficiencies. Forcing growth of the nanoparticles along one crystal direction can be used to create nanorod, nanowire and nanotube electrode structures[45, 46, 47], and has been shown to improve charge collection and reduce recombination[48]. Another approach which focuses on the electrode is to alter its electronc structure by doping[49], or using plasma based treatments to reduce the number of defect recombination centres[50]. Being able to properly characterise the electrode, and the effect of these changes on its properties, is of clear interest to researchers in the field.

Engineering dyes with desirable properties is another approach for improving cell efficiency. As mentioned in the previous section this can offer significant control over the aggregation and optical properties. Obtaining a single dye to absorb strongly across the whole spectral range $\sim$350-950 nm remains a challenge which can be side-stepped by employing a dual sensitising mechanism. Using two or more dyes with high molar extinction coefficients allows this entire spectral width to be covered. Similarly this can be achieved by employing dipole coupled energy transfer through the use of energy relay dyes. Again these approaches highlight the potential benefits of being able to characterise the optical properties of dyes individually, as well as model the electronic response in coupled dye-TiO_2 systems in real time.

1.3 Overview

The unifying theme of this thesis is to exploit computational methods to illuminate the processes at work in DSSCs, with the aim of providing useful insights towards improving device efficiency. The computational approach employed is density functional theory, and in chapter 2 we introduce the method and briefly review some of the fundamental background theory.

Dye anchoring to the semiconductor surface has an extremely important role in DSSCs, having a major influence on charge transfer and device stability. An overwhelming majority of dyes used in DSSCs utilise carboxylic anchor groups to bind to the semiconductor surface, and the interaction between it and the majority face of the most popular semiconductor, anatase

(101) TiO_2, is an important one. However, several recent approaches to improving device efficiency rely on increasing the exposed area of less stable surfaces of anatase, or using the rutile polymorph of TiO_2. In chapter 3, following an introduction to TiO_2 and several important surfaces, we contrast the binding of the carboxylic acid anchor group to several alternatives. Our aim is to address the question of whether carboxylic acid is universally the most suitable binding moiety, irrespective of the TiO_2 surface.

We have already mentioned the importance of dye design and aggregation in DSSCs. Chapter 4 investigates the effects of two common dye design mechanisms on the dyes, their aggregation properties and the interaction with the substrate.

Defects have an important role in defining the properties of semiconductors, and therefore DSSCs. In chapter 5 we investigate the efficiency improvements of DSSCs brought about by introducing aluminium defects into the TiO_2 electrodes. In particular we examine the interplay between these extrinsic defects and one of the intrinsic defects typically found in TiO_2, the oxygen vacancy.

Throughout this introductory chapter an emphasis has been placed on the importance of being able to characterise the optical properties of dyes as well as the potential benefits of being able to model charge dynamics within physically realistic DSSC systems. Chapters 6 and 7 address this problem and focus on the closely related excited state counterpart to density functional theory, time dependent functional theory (TDDFT). In 6 we discuss our implementation of real time TDDFT in the linear scaling DFT code CONQUEST. Results of the testing of our implementation are presented and discussed. Following the validation of our method, chapter 7 proceeds to use our implementation to calculate the optical properties of TiO_2 nanoclusters. Finally we study three coumarin based dye employed in DSSCs, and as a test model system we examine the interaction of the smallest of these dyes with a TiO_2 cluster.

Chapter 2

Density Functional Theory

2.1 Introduction

The work presented in this thesis uses extensively an *ab initio* computational method known as density functional theory (DFT). In this chapter we provide an overview of the theoretical foundations behind the method, and highlight some key points for consideration when carrying out calculations in practice. This will allow the focus of the remaining chapters to be on the results obtained and their analysis.

2.2 The Schrödinger Equation & Many-Body Systems

Ab initio, meaning "from the beginning", refers in our context to computational methods based upon the first principles of quantum mechanics. The fundamental equation governing the behaviour of matter at the quantum scale is the non-relativistic Schrödinger equation[1] :

$$\hat{H}|\Psi(\mathbf{r},\mathbf{R},t)\rangle = i\frac{\partial}{\partial t}|\Psi(\mathbf{r},\mathbf{R},t)\rangle \tag{2.1}$$

with the Hamiltonian operator $\hat{H}$, given by:

$$\hat{H} = -\sum_i \frac{1}{2}\nabla^2_{\mathbf{r}_i} + \sum_i \sum_{j>i} \frac{1}{|\mathbf{r}_i - \mathbf{r}_j|} - \sum_I \frac{1}{2M_I}\nabla^2_{\mathbf{R}_I} + \sum_I \sum_{J>I} \frac{Z_I Z_J}{|\mathbf{R}_I - \mathbf{R}_J|} - \sum_{i,I} \frac{Z_I}{|\mathbf{r}_i - \mathbf{R}_I|} \tag{2.2}$$

[1] Atomic units in use. Nuclear and electronic indices are indicated here by upper and lower case respectively. Spin is included within the coordinate, such as $\mathbf{r} = \{\mathbf{r}\}_i = \{x, y, z, \sigma\}_i$. Z is the atomic number and M the ionic mass.

The term *many-body* refers to the many-body wavefunction that results due to the coupling of the equations of motion for many particles through some interaction, in our case electrons and nuclei coupled through the Coulomb terms of the Hamiltonian. Coupled equations of this sort are impossible to solve analytically for anything but the simplest systems. Dirac is quoted as famously stating, with regard to many-body quantum mechanics[51]:

> *"...the difficulty is that the exact application of these laws leads to equations much too complicated to be soluble."*

Our first step in simplifying the problem is to note that the nuclei are much more massive than electrons, and on the time scale of electronic motion can be considered stationary. Known as the Born-Oppenheimer approximation, this allows the nuclear and electronic equations of motion to be decoupled:

$$\Psi(\mathbf{r}, \mathbf{R}, t) = \Psi(\mathbf{r}, t; \mathbf{R})\Phi(\mathbf{R,t}) \tag{2.3}$$

The electronic wavefunction now has a parametric dependence upon the nuclear positions and the Coulomb interaction can be treated as a static external potential. Then assuming that the electrons relax instantaneously to the ground state configuration, a similar decoupling can be obtained for the time and spatial degrees of freedom, providing us with the following electronic time independent Schrödinger equation (TISE):

$$\hat{H}_{el}|\Psi(\mathbf{r};\mathbf{R})\rangle = E_{el}|\Psi(\mathbf{r};\mathbf{R})\rangle \tag{2.4}$$

$$\text{where} \qquad \hat{H}_{el} = -\sum_i \frac{1}{2}\nabla^2_{\mathbf{r}_i} + \sum_i \sum_{j>i} \frac{1}{|\mathbf{r}_i - \mathbf{r}_j|} - \sum_{i,I} \frac{Z_I}{|\mathbf{r}_i - \mathbf{R}_I|} \tag{2.5}$$

Density functional theory is one computational approach to solve this equation for the ground state of electronic system, although many approaches exist.

2.3 Hartree-Fock

The Hartree-Fock method is another numerical method for solving the electronic TISE. It has several parallels to density functional theory, and here we include a brief discussion of its theoretical background, as it can help elucidate some of the finer points of DFT.

Rather than consider the full many electron wavefunction $\Psi(\mathbf{r})$, we consider the wavefunction for an isolated electron in an external potential, $\phi(\mathbf{r}_\mathrm{i})$, which is a solution to the eigenvalue equation for the corresponding non-interacting Hamiltonian h_i:

$$\hat{h}_i = -\frac{1}{2}\nabla^2_{\mathbf{r}_i} + V(\mathbf{r}_i) \tag{2.6}$$

Considering now a many-electron system made up of *non-interacting* electrons, the many body Hamiltonian will simply be the sum of each of the single-electron Hamiltonians:

$$\hat{H}^{NI} = \sum_i -\frac{1}{2}\nabla^2_{\mathbf{r}_i} + V(\mathbf{r}_i) \tag{2.7}$$

and the solution to the corresponding eigenvalue equation is the product of the isolated electron wavefunctions, known as a Hartree-product.

The variational principle states that the expectation value of a Hamiltonian calculated with a trial wavefunction will be equal to or greater than that calculated with the true wavefunction. Invoking this principle, we can make an ansatz that the functional form of the true many-body wavefunction will be a properly antisymmetric linear combination of Hartree-products, known as a Slater determinant:

$$\Psi^{NI}(\mathbf{r}) = \frac{1}{\sqrt{N!}} \begin{vmatrix} \phi_1(\mathbf{r}_1) & \phi_1(\mathbf{r}_2) & \dots & \phi_1(\mathbf{r}_N) \\ \phi_2(\mathbf{r}_1) & \phi_2(\mathbf{r}_2) & \dots & \phi_2(\mathbf{r}_N) \\ \vdots & \vdots & \ddots & \vdots \\ \phi_N(\mathbf{r}_1) & \phi_N(\mathbf{r}_2) & \dots & \phi_N(\mathbf{r}_N) \end{vmatrix} \tag{2.8}$$

The Hartree-Fock method proceeds by using this properly antisymmetric wavefunction form as a trial wavefunction, and minimisng with respect to the single particle orbitals.

As an example consider a simple two electron system, and operate with upon the corresponding Slater determinant with the full two electron Hamiltonian including the electron-electron interaction. It can be shown (using the assumed orthonormality of our single electron orbital states) that the one-electron operators acting on the Slater determinant will give:

$$\left\langle \Psi^{NI} \middle| \hat{h}_1 + \hat{h}_2 \middle| \Psi^{NI} \right\rangle = \left\langle \phi_1(\mathbf{r}_1) \middle| \hat{h}_1 \middle| \phi_1(\mathbf{r}_1) \right\rangle + \left\langle \phi_2(\mathbf{r}_2) \middle| \hat{h}_2 \middle| \phi_2(\mathbf{r}_2) \right\rangle \tag{2.9}$$

Considering now the two electron term, we have:

$$\left\langle \Psi^{NI} \middle| \frac{1}{|\mathbf{r}_1 - \mathbf{r}_2|} \middle| \Psi^{NI} \right\rangle$$
$$= \int d\mathbf{r}_1\, d\mathbf{r}_2 \Big[\frac{\phi_1^*(\mathbf{r}_1)\phi_2^*(\mathbf{r}_2)\phi_1(\mathbf{r}_1)\phi_2(\mathbf{r}_2)}{|\mathbf{r}_1 - \mathbf{r}_2|} - \frac{\phi_1^*(\mathbf{r}_1)\phi_2^*(\mathbf{r}_2)\phi_1(\mathbf{r}_2)\phi_2(\mathbf{r}_1)}{|\mathbf{r}_1 - \mathbf{r}_2|} \Big] \tag{2.10}$$

The first term in the brackets is simply the probability of finding electron one at $\mathbf{r}_1$ by the probability of finding electron two at $\mathbf{r}_2$, over their separation. Integrating this gives the Coulombic interaction between the two electrons, and this first term is known as the Hartree energy. This exact same term would arise if the many-electron Hamiltonian were to act upon a simple Hartree product. The second term however would not, and it occurs as a result of the antisymmetric form of the Slater determinant. It is known as the exchange integral, as on moving from one side of the integrand to the other the electrons exchange their positions.

So in a similar manner, it is possible to write the generalised expression for the energy of a Slater determinant as

$$\left\langle \Psi^{NI} \middle| H_{el} \middle| \Psi^{NI} \right\rangle = \sum_i \left\langle \phi_i \middle| \hat{h}_i \middle| \phi_i \right\rangle + \sum_i \sum_{j>i} \langle ij|ij\rangle - \langle ij|ji\rangle \tag{2.11}$$

Minimising this expression involves the construction of a Lagrangian and, using the orthonormality of the orbitals as a constraint, minimising with respect to the single particle orbitals. The resulting set of equations are known as the Hartree-Fock equations:

$$h(i)\phi_i(\mathbf{r}_1) + \sum_j J_j(\mathbf{r}_1)\phi_i(\mathbf{r}_1) - \sum_j K_{ij}(\mathbf{r}_1)\phi_j(\mathbf{r}_1) = \epsilon_i \phi_i(\mathbf{r}_1) \tag{2.12}$$

where

$$J_j(\mathbf{r}_1) = \int d\mathbf{r}_2 \Big[\phi_j^*(\mathbf{r}_2) \frac{1}{|\mathbf{r}_1 - \mathbf{r}_2|} \phi_j(\mathbf{r}_2) \Big] \tag{2.13}$$

$$K_{ij}(\mathbf{r}_1)\phi_j(\mathbf{r}_1) = \left(\int d\mathbf{r}_2 \Big[\phi_j^*(\mathbf{r}_2) \frac{1}{|\mathbf{r}_1 - \mathbf{r}_2|} \phi_i(\mathbf{r}_2) \Big] \right) \phi_j(\mathbf{r}_1) \tag{2.14}$$

J_j and K_j are known as the Coulomb and exchange operators respectively. A point worth noting is that for the Coulomb operator the above expression will include a self-interaction, when i=j. This term is exactly cancelled by the equivalent i=j case of the exchange operator.

2.3.1 Exchange & Correlation I

Explicitly writing our single electron wavefunction as a product of a spin orbital and a spatial orbital we have, for two electrons with opposite spins:

$$\phi(\mathbf{r}_1) = \theta(\mathbf{r}_1)\alpha(\omega_1) \tag{2.15}$$

$$\phi(\mathbf{r}_2) = \theta(\mathbf{r}_2)\beta(\omega_2) \tag{2.16}$$

Now considering the properly antisymmetric wavefunctions for a system of two electrons in two separate cases, with **S**=0,-1, we have:

$$\Psi_{\uparrow\uparrow} = \frac{1}{\sqrt{2}}\Big[\theta_1(\mathbf{r}_1)\alpha(\omega_1)\theta_2(\mathbf{r}_2)\alpha(\omega_2) - \theta_1(\mathbf{r}_2)\alpha(\omega_2)\theta_2(\mathbf{r}_1)\alpha(\omega_1)\Big] \tag{2.17}$$

$$\Psi_{\uparrow\downarrow} = \frac{1}{\sqrt{2}}\Big[\theta_1(\mathbf{r}_1)\theta_2(\mathbf{r}_2) + \theta_1(\mathbf{r}_2)\theta_2(\mathbf{r}_1)\Big]\frac{1}{\sqrt{2}}\Big[\alpha(\omega_1)\beta(\omega_2) - \alpha(\omega_2)\beta(\omega_1)\Big] \tag{2.18}$$

If we consider the probability of finding electron 1 at $\mathbf{r}_1$ and the probability of finding electron 2 at $\mathbf{r}_2$ for both cases we have:

$$\begin{aligned} P_{\uparrow\downarrow}(\mathbf{r}_1,\mathbf{r}_2) &= \int d\omega_1\, d\omega_2 |\Psi|^2_{\uparrow\downarrow} \\ &= \frac{1}{2}\Big[|\theta_1(\mathbf{r}_1)|^2|\theta_2(\mathbf{r}_2)|^2 + |\theta_1(\mathbf{r}_2)|^2|\theta_2(\mathbf{r}_1)|^2\Big] \end{aligned} \tag{2.19}$$

$$\begin{aligned} P_{\uparrow\uparrow}(\mathbf{r}_1,\mathbf{r}_2) &= \int d\omega_1\, d\omega_2 |\Psi|^2_{\uparrow\uparrow} \\ &= \frac{1}{2}\Big[|\theta_1(\mathbf{r}_1)|^2|\theta_2(\mathbf{r}_2)|^2 + |\theta_1(\mathbf{r}_2)|^2|\theta_2(\mathbf{r}_1)|^2 - \\ &\qquad \theta_1^*(\mathbf{r}_1)\theta_2(\mathbf{r}_1)\theta_2^*(\mathbf{r}_2)\theta_1(\mathbf{r}_2) - \theta_1(\mathbf{r}_1)\theta_2^*(\mathbf{r}_1)\theta_2(\mathbf{r}_2)\theta_1^*(\mathbf{r}_2)\Big] \end{aligned} \tag{2.20}$$

We can see that the probability for anti-parallel spins is the average of the combined probability of finding electron one at $\mathbf{r}_1$ and electron two at $\mathbf{r}_2$ and vice-versa. For parallel spins there is an extra cross-term, due to the particle exchange. This term reduces the probability of two electrons with the same spin approaching one another, and there is zero probability that they occupy the same space. This behaviour can be described as electrons of like spin having an exchange *correlation*. Avoidance of electrons of like spin results in a stabilisation of the system, and the formation of what is known as an exchange hole; a volume of reduced probability density surrounding electrons of like spin.

Through the exchange operator Hartree-Fock treats exchange exactly and correctly describes the associated correlation. However a further correlation will exist due to the Coulomb

interaction between electrons repelling one another. This interaction is treated in a mean-field manner within Hartree-Fock, meaning that each electron will feel an average Coulomb response from all the others. This results in the Coulomb correlation being incorrectly described, and an associated error in the energy.

2.4 Density Functional Theory

Density functional theory is an alternative approach to obtaining the solution of the electronic TISE (equation 2.5) in which the variable of interest is not the many-body wavefunction but the electronic density. The power of this approach can be seen when considering a system of N electrons; the full many-body wavefunction is a function of 3N variables, the electronic density is a function of 3.

2.4.1 The Hohenberg-Kohn Theorems

Reducing the problem of solving for a 3N dimensional wavefunction to that of solving for a 3 dimensional density is a spectacular improvement. The first question we must ask is; will knowing the electron density of a system be sufficient to define its properties? Two theorems from Hohenberg and Kohn [52] prove that this is indeed the case.

Writing the electronic Hamiltonian of equation 2.5 as

$$\hat{H}_{el} = \hat{T} + \hat{U} + \hat{V}_{ext} \tag{2.21}$$

where

$$\hat{T} + \hat{U} = -\sum_i \frac{1}{2}\nabla^2_{\mathbf{r}_i} + \sum_i \sum_{j>i} \frac{1}{|\mathbf{r}_i - \mathbf{r}_j|} \tag{2.22}$$

$$\hat{V}_{ext} = -\sum_i V_{ext}(\mathbf{r}_i) \tag{2.23}$$

where the nuclei-electron interaction is treated as a static external potential. We can see that for every N electron system $\hat{T} + \hat{U}$ is identical. Therefore the Hamiltonian, and as a result the energy, is defined by N and $\hat{V}_{ext}$.

The first Hohenberg and Kohn theorem relates this external potential to the electronic density:

Theorem 1. *The ground state density of an interacting electronic system, $n_0(\boldsymbol{r})$ will uniquely define the external potential, $V_{ext}(\boldsymbol{r})$. $n_0(\boldsymbol{r})$ therefore uniquely defines the ground state energy.*

Proof. Taking an electronic Hamiltonian, $\hat{H}$, defined by V_{ext}, we have an associated ground state Ψ_0 and electronic density $n_0(\mathbf{r})$. Consider a second different external potential, V'_{ext}, with Ψ'_0 and $n'_0(\mathbf{r})$.

From the variational principle we have that:

$$E_0 = \langle \Psi_0 | \hat{H} | \Psi_0 \rangle < \langle \Psi'_0 | \hat{H} | \Psi'_0 \rangle \tag{2.24}$$

$$E_0 < \langle \Psi'_0 | \hat{T} + \hat{U} + \hat{V}_{ext} + \hat{V}'_{ext} - \hat{V}'_{ext} | \Psi'_0 \rangle \tag{2.25}$$

$$E_0 < \langle \Psi'_0 | \hat{H}' | \Psi'_0 \rangle + \langle \Psi'_0 | \hat{V}_{ext} - \hat{V}'_{ext} | \Psi'_0 \rangle \tag{2.26}$$

$$E_0 < E'_0 + \int d\mathbf{r}\, n'_0(\mathbf{r})[V_{ext} - V'_{ext}] \tag{2.27}$$

Using the variational principle again, we have from the expectation value of $\hat{H}'$ acting on Ψ_0:

$$E'_0 < E_0 - \int d\mathbf{r}\, n_0(\mathbf{r})[V_{ext} - V'_{ext}] \tag{2.28}$$

Proof by reductio ad absurdium can proceed by assuming that two different potentials, namely V_{ext} and V'_{ext}, produce the same density such that $n_0(\mathbf{r}) = n'_0(\mathbf{r})$. Substituting this into the inequalities above, and then adding them gives the apparent contradiction:

$$E'_0 + E_0 < E'_0 + E_0 \tag{2.29}$$

□

Theorem 2. *Minimising an unique energy functional defined by a v-representable density, $n(\boldsymbol{r})$, with respect to variations in the density produces the ground state energy for the Hamiltonian.*

Proof. Having proven that the density uniquely defines the external potential, and by extension the Hamiltonian, we can write the energy as a functional of the electronic density $E[n(\mathbf{r})]$. For a given potential we have the associated wavefunction, Ψ'. Calculating the expectation value for Ψ' with the correct ground state Hamiltonian, H_0, and employing the variational principle gives:

$$\langle \Psi' | H_0 | \Psi' \rangle > \langle \Psi | H_0 | \Psi \rangle \tag{2.30}$$

$$E[n(\mathbf{r})] > E[n_0(\mathbf{r})] \tag{2.31}$$

□

2.4.2 The Kohn-Sham Approach

The Hohenberg-Kohn theorems provide the fundamental foundation for a method of solving the electronic many body Schrödinger equation, based on a minimisation of the energy functional with respect to the density. However in order to proceed we need a practical framework for carrying out this minimisation. Kohn-Sham density functional theory (KS-DFT) provides this framework [53].

The primary ansatz of the Kohn-Sham approach is that the full many body density can be represented by an auxiliary system of non-interacting single electron orbitals, with the same ground state density as that of the interacting system.

$$n(\mathbf{r}) = \sum_{i}^{N} \psi_i^*(\mathbf{r})\psi_i(\mathbf{r}) \tag{2.32}$$

Writing the energy as a functional of the density we have:

$$E[n(\mathbf{r})] = T_{KS}[n(\mathbf{r})] + E_{ext}[n(\mathbf{r})] + E_H[n(\mathbf{r})] + E_{xc}[n(\mathbf{r})] \tag{2.33}$$

The kinetic energy functional for the full interacting density, $T[n(\mathbf{r})]$ is unknown. However the kinetic energy of our non-interacting auxiliary Kohn-Sham single particle system can be calculated as:

$$T_{KS}[n(\mathbf{r})] = -\sum_{i} \frac{1}{2}\langle\psi_i|\nabla_i^2|\psi_i\rangle \tag{2.34}$$

.

noting that, as written, the kinetic energy of our system is a functional of the single electron Kohn-Sham wavefunction and therefore implicitly a functional of the density.

Similarly the full electron-electron interaction as a functional of the density is unknown, so here we use the now familiar classical Hartree energy functional, written in terms of the density:

$$E_H[n(\mathbf{r})] = \frac{1}{2}\int d\mathbf{r}\, d\mathbf{r}' \frac{n(\mathbf{r})n(\mathbf{r}')}{|\mathbf{r}-\mathbf{r}'|} \tag{2.35}$$

$E_{ext}[n(\mathbf{r})]$ gives the contribution to energy from the interaction with an external potential, including the stationary nuclei:

$$E_{ext}[n(\mathbf{r})] = \int d\mathbf{r}\, V_{ext} n(\mathbf{r}) \tag{2.36}$$

The final term in equation 2.33 is known as the exchange-correlation energy functional. Evaluating the kinetic energy using the Kohn-Sham single particle orbitals, through equation 2.34, will be incorrect. Similarly our classical treatment of the electron-electron interaction through the Hartree energy functional is incorrect, equation 2.35. The exchange correlation functional rolls up the induced errors due to the neglect of the many-body correlation and exchange effects and it can be defined implicitly as:

$$E_{XC}[n(\mathbf{r})] = (T[n(\mathbf{r})] - T_{KS}[n(\mathbf{r})]) + (E_{e-e}[n(\mathbf{r})] - E_H[n(\mathbf{r})]) \tag{2.37}$$

where $T[n(\mathbf{r})]$ and $E_{e-e}[n(\mathbf{r})]$ are the full interacting many-body kinetic and Coulomb energy functionals respectively.

This expression for the energy must now be minimised. Imposing the constraint that the Kohn-Sham states are orthonormal, we obtain the following Lagrangian:

$$L_{KS}[n] = T_{KS} + E_H + E_{ext} + E_{XC} - \sum_{ij} \epsilon_{ij} \Big[\int d\mathbf{r} \psi_j^* \psi_i - \delta_{ij} \Big] \tag{2.38}$$

Minimising with respect to the orbitals requires that:

$$\frac{\delta L_{KS}}{\delta \psi_j^*} = 0 \tag{2.39}$$

So employing the chain rule we have that:

$$\frac{\delta T_{KS}}{\delta \psi_j^*} + \Big[\frac{\delta E_H}{\delta n} + \frac{\delta E_{ext}}{\delta n} + \frac{\delta E_{XC}}{\delta n} \Big] \frac{\delta n}{\delta \psi_j^*} = \epsilon_i \psi_i \tag{2.40}$$

Taking the functional derivative of the Hartree energy gives us an equation for the Hartree potential:

$$V_H = \frac{\delta E_H}{\delta n} = \int d\mathbf{r}' \frac{n(\mathbf{r}')}{|\mathbf{r} - \mathbf{r}'|} \tag{2.41}$$

We therefore obtain the final Kohn-Sham equations:

$$\Big[-\frac{\nabla^2}{2} + V_H + V_{ext} + V_{XC} \Big] \psi_i = \epsilon_i \psi_i \tag{2.42}$$

where

$$V_{XC} = \frac{\delta E_{XC}}{\delta n} \tag{2.43}$$

Our final Kohn-Sham equations can be seen to resemble that of a set of single electron Schrödinger equations, in which the electrons are subject to an effective potential (here the

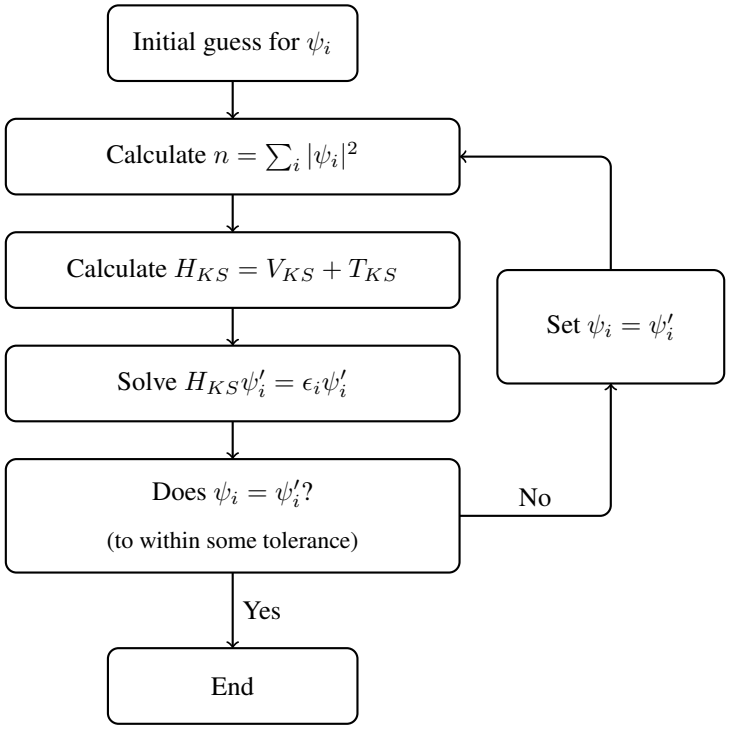

Figure 2.1: A simplistic schematic for a self-Consistent DFT loop

Kohn-Sham potential $V_{KS} = V_H + V_{ext} + V_{XC}$). This effective potential couples our single electron equations through the Hartree and exchange-correlation potentials. Impressively, the Kohn-Sham approach has taken the solution of an N electron problem and cast it onto that of N single electron problems - a much less daunting task.

An important point to note is that the solution of the Kohn-Sham system is dependent upon the effective potential, which is in turn dependent upon the electronic density. Solving a system of equations with this chicken and egg circular dependency must be done self-consistently, as simplistically illustrated in figure 2.1.

2.4.3 Exchange & Correlation II

In the previous section on exchange and correlation in Hartree-Fock 2.3.1, we saw that particle exchange was treated exactly for the single particle orbitals of our Slater determinant. Correlation effects as a result of the Coulomb interaction are inadequately described by Hartree-Fock, as a result of the mean-field treatment of the Coulomb operator and the single particle approach to the kinetic energy, and there will be an associated error.

Density functional theory results in single particle like equations, with the Coulomb interaction treated in a mean-field manner and the approximation that the kinetic energy is adequately described by the sum over single particle kinetic energies. A difference between Hartree-Fock and density functional theory is that in DFT no particle exchange correction arises in our equations, as we evaluate the Hartree energy directly from the density, and there will also be this exchange error.

Density functional theory attempts to account for these correlation and exchange errors through the use of the exchange-correlation functional of equation 2.37. It is worth noting that if the exact form of this exchange-correlation functional were known DFT would be formally exact. However the exact form of this functional is unknown, and approximations must be made.

The simplest approach is to assume that the exchange and correlation at each point is adequately described by that of a uniform electron gas of the same density, known as the local density approximation (LDA) [53]:

$$E_{XC}^{LDA}[n(\mathbf{r})] = \int d\mathbf{r}\, \epsilon_{XC}^{LDA}(n) n(\mathbf{r}) \tag{2.44}$$

where $\epsilon_{XC}^{LDA}(n)$ is the exchange-correlation energy per electron for a uniform electron gas of density n. The exchange term for the uniform electron gas is known exactly, and is given by[54]:

$$\epsilon_X = -\frac{3}{4}\left(\frac{3}{\pi}\right)^{\frac{1}{3}} n(\mathbf{r})^{\frac{1}{3}} \tag{2.45}$$

Analytically the correlation term is unknown, but can be obtained to high accuracy from quantum Monte Carlo calculations[55]. We have a final expression for the LDA exchange correlation potential:

$$V_{XC}^{LDA} = \epsilon_{XC}^{LDA}(\mathbf{r}) + n(\mathbf{r})\frac{\delta \epsilon_{XC}^{LDA}(\mathbf{r})}{\delta n} \tag{2.46}$$

The LDA approximation works remarkably well, considering the simplicity of the idea. As you would expect, it tends to perform better for systems in which the electrons approach that of a slowly varying, uniform electron gas, such as metallic systems. Similarly it performs better for extended solids, and not as well for finite systems such as molecules. LDA has a tendency to overbind atoms, leading to errors in the calculated lattice parameters and cohesive energies.

One approach to improving on the local density approximation is to include some degree of non-locality through a dependence upon the gradient of the density:

$$E_{XC}^{GGA} = [n(\mathbf{r})] = \int d\mathbf{r}\, n(\mathbf{r}) \epsilon_{XC}^{GGA}[n, \boldsymbol{\nabla} n] \tag{2.47}$$

Known as generalised gradient approximations (GGAs), the inclusion of the gradient allows for a more accurate description of systems in which the density varies rapidly. For example GGAs have shown significant improvements over the LDA approximation for molecular systems[56, 57]. Several different forms of the GGA functiona exist, with two of the most widely used being the PW91[56] and the PBE[58] functionals.

While density functional theory is in itself exact, the exact form of the exchange-correlation energy functional is not known. Looking at our expression for the Hartree energy, equation 2.35, we can see an apparent problem; even for a single electron system we will still obtain a Hartree interaction, and thus every electron interacts with itself. If the exact exchange-correlation functional were known, this self-interaction would be exactly cancelled. This is one of the systematic failings of DFT within the LDA/GGA approach, *self-interaction* of the electron density. This self-interaction leads to overly delocalised Kohn-Sham states, and contributes to an underestimation of the band-gap of solids.

Several approaches exist to try and corrrect for this self-interaction error, such as orbital effective potentials, self-interaction corrections[59] and the so called DFT+U method[60, 61]. As mentioned at the end of section 2.3, Hartree-Fock does not suffer from this problem, as the self-interaction resulting from the Coulomb operator is exactly cancelled by an equivalent term in the exchange operator. One popular approach to counter the self interaction, and include a description particle exchange, is to directly mix Hartree-Fock exchange into the exchange correlation functional. Known as hybrid functionals, one of the most popular is the B3LYP functional [62, 63, 64] which mixes expressions for Hartree-Fock exchange with exchange and correlation from GGA and LDA through three empirically fitted parameters.

Hybrid functionals such as the B3LYP have shown improvements over GGA & LDA in the description of band gaps of solids, and in capturing the physics of localised defect states. However the use of these hybrid functionals is more computationally demanding, due to the need to evaluate the orbital dependent Hartree-Fock exchange.

2.5 Practical DFT Calculations

Now that we have presented some of the basic theory behind DFT we now move onto a discussion of how the calculations are performed in practice. We wish to briefly highlight the tricks of the trade for DFT calculations as performed by physicists, and give a brief idea of the nuts and bolts that make up a DFT code, while highlighting points to be taken into consideration to obtain reliable results.

2.5.1 Periodicity

Ostensibly the modelling of a bulk crystal system requires the treatment of an infinite number of atoms within the bulk, and the corresponding infinite number of electrons. Exploiting the periodicity of the crystal along with Bloch's theorem allows us to bypass this problem and replace it with that of modelling the system within one repeating unit cell.

Bloch's theorem states that for a periodic potential the eigenstates of a one-electron Hamiltonian (such as our Kohn-Sham Hamiltonian) may be expressed as:

$$\psi_{n\mathbf{k}}(\mathbf{r}) = u_{n\mathbf{k}}(\mathbf{r})\, e^{\imath \mathbf{k}\cdot\mathbf{r}} \tag{2.48}$$

where $u_{n\mathbf{k}}(\mathbf{r})$ is a function which exhibits the periodicity of the lattice, i.e.:

$$u_{n\mathbf{k}}(\mathbf{r}) = u_{n\mathbf{k}}(\mathbf{r}+\mathbf{R})$$

where

$$\mathbf{R} = N_1\mathbf{a}_1 + N_2\mathbf{a}_2 + N_3\mathbf{a}_3$$

where $\mathbf{a}_i$ are the primitive lattice vectors, and N_i are the number of primitive cells in the crysal along direction *i*.

In general the plane wave $e^{\imath\mathbf{k}\cdot\mathbf{r}}$ will not exhibit this periodicity. However if we impose the boundary condition that $\psi(\mathbf{r}) = \psi(\mathbf{r}+\mathbf{R})$ we see that $e^{\imath\mathbf{k}\cdot\mathbf{r}}$ will also necessarily be lattice periodic, and a resulting restriction of allowed values of $\mathbf{k}$ will follow:

$$\begin{aligned}\psi(\mathbf{r}+\mathbf{R}) &= e^{\imath\mathbf{k}\cdot(\mathbf{r}+\mathbf{R})}u(\mathbf{r}) \\ &= e^{\imath\mathbf{k}\cdot\mathbf{R}}e^{\imath\mathbf{k}\cdot\mathbf{r}}u(\mathbf{r}) \\ &= e^{\imath\mathbf{k}\cdot\mathbf{R}}\psi(\mathbf{r})\end{aligned} \tag{2.49}$$

We can write $\mathbf{k}$ in the basis of primitive reciprocal lattice vectors, $\mathbf{b}_i$ (defined such that $\mathbf{b}_i \cdot \mathbf{a}_j = 2\pi\delta_{ij}$):

$$\mathbf{k} = y_1\mathbf{b}_1 + y_2\mathbf{b}_2 + y_3\mathbf{b}_3 \tag{2.50}$$

and can therefore see that in order for the last line in equation 2.49 to hold we require that $e^{\imath\mathbf{k}\cdot\mathbf{R}} = 1$, and the following restriction on allowed values of $\mathbf{k}$ is obtained:

$$\mathbf{k} = \sum_{i=1}^{3} \frac{m_i}{N_i}\mathbf{b}_i \qquad , m_i \in \mathbb{Z} \tag{2.51}$$

and as the limit of an infinite crystal is approached (i.e. $N_i \to \infty$), the k-space becomes continuous.

For each value of $\mathbf{k}$, substitution of the Bloch wavefunction form into the single electron Hamiltonian results in an eigenvalue equation, to which there is an infinite set of discrete solutions (labelled by the band index n). So our problem has been transformed from solving an infinite number of wavefunctions, to solving a finite number of wavefunctions for an infinite number of $\mathbf{k}$

Our first simplification comes from a consequence of the Bloch theorem that, for any wave vector $\mathbf{k}'$ outside of the first Brillouin zone (1BZ) there is an equivalent $\mathbf{k}$ within it. This can be observed by taking $\mathbf{k}' = \mathbf{k}+\mathbf{K}$, where $\mathbf{K}$ is a reciprocal lattice vector, and noting $e^{\imath\mathbf{K}\cdot\mathbf{R}} = 1$. It is therefore possible to restrict ourselves exclusively to solutions within the 1BZ.

Secondly the eigenvalue equation resulting from the substitution of our Bloch wave function into the one-electron Hamiltonian contains the value of $\mathbf{k}$ as a parameter (see for example [65]). This has the consequence that the values of corresponding eigenvalues vary continuously with $\mathbf{k}$, and integrals over the infinite values of $\mathbf{k}$ can be approximated by sums over finite, special and carefully selected k-points. One popular method for discretising the k-space is due to Monkhorst and Pack[66]. This brings us to the first consideration for carrying out DFT calculations in practice, in order to ensure that the sum over these special k-points is accurate, the grid of k-points must be sufficiently dense.

A second consideration arises as a result of the system we are interested in being treated as a replication of a periodically repeating cell. In order to treat surfaces and isolated systems, for example a water molecule shown in 2.2, we must extend a region of vacuum within our periodic unit cell in order to minimise interaction, known as the supercell approach.

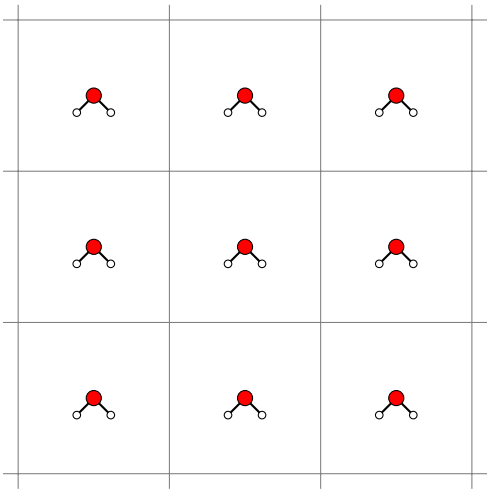

Figure 2.2: Two dimensional illustration of the supercell approach for simulating a water molecule within periodic boundaries.

2.5.2 Plane-Waves

The typical approach taken to solve the set of Kohn-Sham equations is to expand the Kohn-Sham states in some basis, from which the matrix equation can be constructed and solved efficiently (although other approaches exist; for example the direct minimisation of system energy through using the density matrix, addressed in chapter 6). This leaves us with a choice of which basis set to use.

One choice[2] becomes obvious if we examine our wavefunction represented as a cell periodic function modulated by a plane wave:

$$\psi_{n\mathbf{k}}(\mathbf{r}) = e^{i\mathbf{k}\cdot\mathbf{r}} u_{n\mathbf{k}}(\mathbf{r}) \tag{2.52}$$

we know that the $u_{n\mathbf{k}}(\mathbf{r})$ is cell periodic, so we can expand it in a Fourier series such that:

$$u_{n\mathbf{k}}(\mathbf{r}) = \sum_{\mathbf{K}} c_{n\mathbf{K}} e^{i\mathbf{K}\cdot\mathbf{r}} \tag{2.53}$$

Substituting our plane wave expansion of equation 2.53 into equation 2.52 gives us the

[2]There are again, of course, other choices one example is pseudo atomic orbitals, which are briefly introduced in chapter 6

expression for our Kohn-Sham state represented in a plane wave basis:

$$\psi_{n\mathbf{k}}(\mathbf{r}) = \sum_{\mathbf{K}} c_{n,\mathbf{k}+\mathbf{K}} e^{i(\mathbf{k}+\mathbf{K})\cdot\mathbf{r}} \tag{2.54}$$

Thus for each k-point our Kohn-Sham state is expanded in a basis of plane-waves. Large wave-vector plane waves will contribute less to the expansion of the Bloch function, so to a good approximation we can truncate the series at an arbitrary but suitably high point. The cut-off point is typically defined by some kinetic cut-off energy, below which the plane waves are included.

In practice this cut-off energy will define the accuracy of the calculation; as the basis set is reduced the quality of the wavefunction is also reduced, meaning that a higher energy is obtained. In practice it is important to converge calculations with respect to this energy cut-off in order to ensure the validity of results. A point to note is that the incomplete basis set will vary discretely at each k-point if the cell-shape is varied, and discrete changes in the energy will occur. The simplest approach to solving this problem (although others exist [67]) is to employ an energy cut-off sufficiently high so that energies are converged over the full range of the volume change.

2.5.3 Pseudopotentials

Orthonormality demands, for systems with several inner core electron shells, that close to ionic cores the wavefunctions for the valence electrons are rapidly varying. Representing these oscillating wavefunctions accurately requires a large number of plane-waves in the basis, and hence more computational effort. Other computational difficulties exist in the form of the ionic core potential tending to infinity as $\mathbf{r} \to 0$.

A simplification can proceed from the fact that many properties are determined by the valence electrons, with the inner core electrons providing little contribution. Thus the ionic core may grouped with the inner electrons and the combined effect represented by a finite pseudopotential. Outside of some critical radius from the ionic core, r_c, the pseudopotential and corresponding pseudo-wavefunction are chosen to follow the all electron potential and wavefunction.

Inside r_c the pseudopotential diverges from the correct potential, varying smoothly and staying finite at $\mathbf{r} = 0$. The resulting pseudo-wavefunction has fewer nodes and is more smoothly varying within this critical radius than the all electron wavefunction. As a consequence it is much more efficiently described in a plane wave basis.

Pseudopotentials are not unique and numerous methods exist for their construction, although generally they all satisfy the same set of criteria:

- All-electron and pseudo wavefunctions must coincide for all points outside the cut off radius.
- Eigenvalues must coincide for both all-electron and pseudo wavefunctions.
- Logarithmic derivatives of the all-electron and pseudo wavefunctions agree at r_c
- First derivative w.r.t. energy of the logarithmic derivative agree for the all-electron and pseudo wavefunctions for $r \geq r_c$

From the first criterion the implication is that the charge for all-electron and pseudo wavefunctions within the cut off radius are equal. Pseudopotentials which adhere to this are known as norm-conserving. It is possible to relax this constraint to provide a smoother wavefunction, in what is known as ultrasoft pseudopotentials [68], the benefit of which is that the pseudowavefunctions are smoother and fewer plane waves are required for their accurate description.

In practice constructing a pseudopotential usually proceeds by the numerical solution for the radial atomic Schrödinger equation for the atom in question. Generating pseudowavefunctions which satisfy the necessary criteria, with respect to this numerical solution, it is then possible to insert them into the Schrödinger equation and solve for the pseudopotential.

2.6 Chapter Summary

In this chapter we have discussed the difficulty of solving the many-body Schrödinger equation, and introduced two methods which can be used to tackle the problem. We have presented the fundamental background of density functional theory (DFT), the computational approach which we will use to perform the calculations in the remaining chapters. Finally, we have discussed some aspects of performing these calculations in practice and points to consider in order to obtain meaningful results with minimal computational expense.

Chapter 3

Adsorption of Acidic Binding Groups on TiO_2 Surfaces

3.1 Introduction

Titanium dioxide (TiO_2) has a wide range of practical applications; for example in photocatalysis [69, 70], as a white pigment [71], photo-degradation of molecules at its surface make it useful as an anti-bacterial agent[72] and in waste water treatment[73], and of course it is used in dye sensitised solar cells. Due to the number of technological uses, considerable effort has been expended in characterising the properties of TiO_2(for a review see [74]). TiO_2 surface structure and its interaction with molecules is of fundamental importance to many potential applications, not least DSSCs. This fact has acted as the driving force behind the characterisation of titania surfaces, and the study of how these surfaces and molecules interact.

Dye sensitised solar cells' efficiency relies heavily on the interplay between sensitising dye and the TiO_2 surface to which it binds. A strong interaction will ensure the dye remains bound to the surface, and good electronic overlap between the surface and dye is essential for efficient charge transfer [75]. This stresses the importance played by the anchoring moiety in a sensitising dye. Ruthenium based record efficiency dyes (N719, N3, black dye [76, 77, 78]) all contain one or more carboxylic acid binding groups, and the vast majority of sensitising dyes have followed this anchoring strategy.

Titanium dioxide exists in several polymorphs, two of which are used in DSSCs, anatase and rutile. TiO_2 in nanocrystalline form is most thermodynamically stable in its anatase phase [79], with the (101) face dominating more than 94% of the crystal surface [80]. Coupling this

with the fact that most sensitising dyes use a carboxylic binding moiety, highlights the importance of the (101)-carboxylic acid interaction. Several experimental and theoretical studies have been devoted to examining the interaction of carboxylic anchors with the TiO_2 (101) surface[81, 82].

However, carboxylic acid groups are not the only choice for anchoring dyes to TiO_2 surfaces, and bias towards them may be at the expense of other potentially useful candidates being neglected. Examples include phosphonic acid [83, 84], boronic acid[85], and cyanobenzoic acid[86], all of which have been used as binding groups in DSSCs. Notably dyes utilising phosphonic acids have shown a stronger binding interaction with TiO_2 than carboxylic acids[84, 87], suggesting an advantage over those utilising carboxylic acids. Increased binding strength could lead to higher dye uptake and enhanced longevity over carboxylic acid bound dyes, as these tend to slowly desorb from the TiO_2 surface.

In a similar vein, while the prevalence of the anatase (101) surface make it extremely important, the interaction of dyes with other TiO_2 surfaces and polymorphs should not be neglected. For example, the use of nanostructured rutile TiO_2 exposing the (110) surface has been explored as a potential avenue for increased electron transport rates through the electrode, resulting from reduced grain boundaries [88, 89, 90]. Also interest in the less stable (001) anatase surface is increasing due to recent work showing that electrodes exposing the (001) face significantly improves device performance as a result of enhanced light scattering and increased surface activity [91, 92, 93].

Interactions between any particular anchor group and TiO_2 will necessarily differ depending on the surface. The aim of this chapter, therefore, is to assess the relative merits of three potential anchor groups when binding to these less utilised, but increasingly important, surfaces. Firstly we introduce the two most important polymorphs of TiO_2, rutile and anatase, and calculate the bulk properties of both. Following this we move on to an examination of the three mentioned surfaces; anatase (101), anatase (001) and rutile (110). Finally we investigate the adsorption of two potential anchoring groups, phosphonic acid and boronic acid, at these surfaces and contrast to that of carboxylic acid.

3.2 Computational Details

All the calculations in this chapter have been performed using the plane wave DFT code VASP[94]. Electron exchange and correlation was treated within the generalised gradient approximation of Perdew and Wang[95] and the pseudopotential method was utilised in the

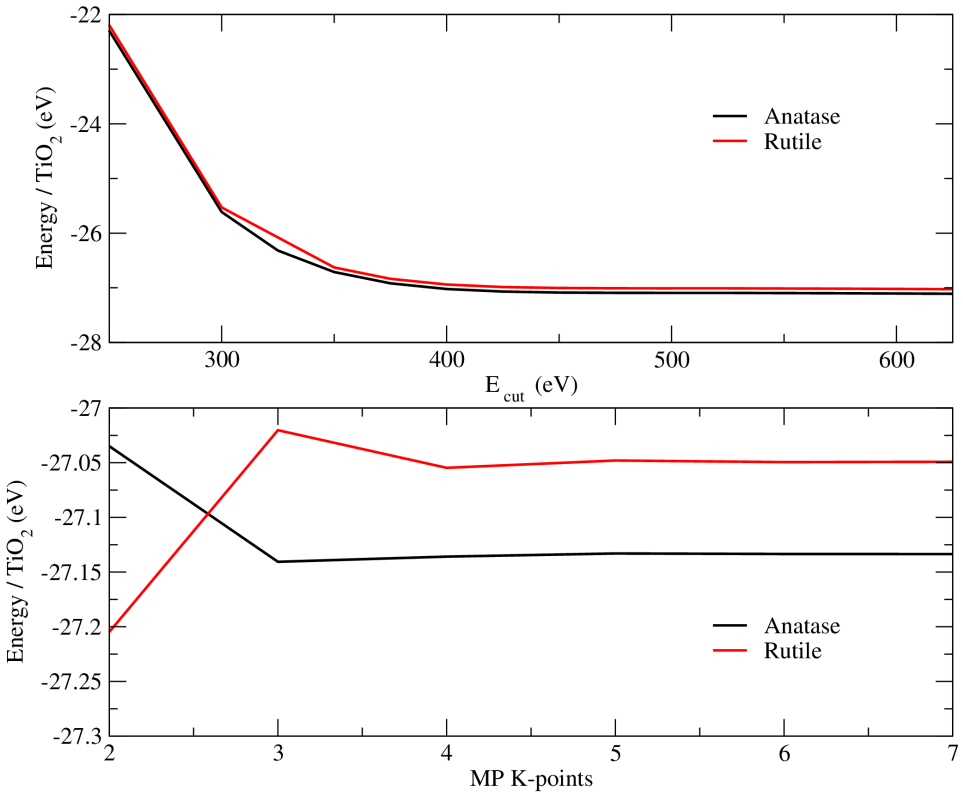

Figure 3.1: Total energy variation with respect to Monkhorst-Pack k-point mesh density along the minor axis (bottom) and energy cut-off (top) for bulk TiO_2 rutile and anatase. For the variation in K-point mesh density the number of K-points along the major axis is held constant.

form of ultrasoft Vanderbilt pseudopotentials[96] to treat core electrons. For Titanium atoms the $4s^2 3d^2$ electrons are treated as valence electrons, for boron, oxygen, carbon and nitrogen the 1s electrons are treated as being in the core. Phosphorous atoms are treated with the $1s^2 2s^2 2p^6$ electrons considered to be in the core.

Convergence of results with respect to the input parameters is one of the most important points to consider when performing DFT calculations. Our goal is to obtain meaningful results through a suitable level of accuracy in our approximations, but at minimum computational expense. As discussed in the previous chapter, two of the most important parameters in a DFT calculation are the size of the basis set and the reciprocal space sampling. In order to gauge the level of accuracy required for our systems we have varied both of these parameters and examined the dependence of the total energy both, the results of which can be seen in Figure 3.1.

In the case of the k-point sampling the variation shown is with respect to the Monkhorst-Pack k-point grid density along the minor axis, and the total energy is converged to 2meV and 3meV at 6 k-points with respect to that at 5 k-points for anatase and rutile respectively. For the bulk calculations we have employed a k-point mesh of $(6 \times 6 \times 3)$ and $(3 \times 3 \times 6)$ for anatase and rutile respectively.

Variation of basis set size, or equivalently the energy cut-off, is also shown in Figure 3.1. Total fixed-volume energies at a cut-off of 450 eV are found to be converged to within 17 meV of those obtained at a cut-off of 650 eV for both rutile and anatase. Variation in cell volume will cause discontinous changes in the basis set, as discused in the previous chapter, and during the calculation of the lattice parameters and bulk modulii the higher cut-off of 650 eV has been used to ensure accuracy. Structural relaxation is performed using the RMM-DIIS[97] method until the forces on free ions were less than 0.005 eV/Å for bulk calculations.

3.3 Bulk TiO_2 Properties

As mentioned, TiO_2 exists in several polymorphs, and two of particular interest in the field of DSSCs are anatase and rutile. The unit cells for both crystals are shown in figure 3.2.

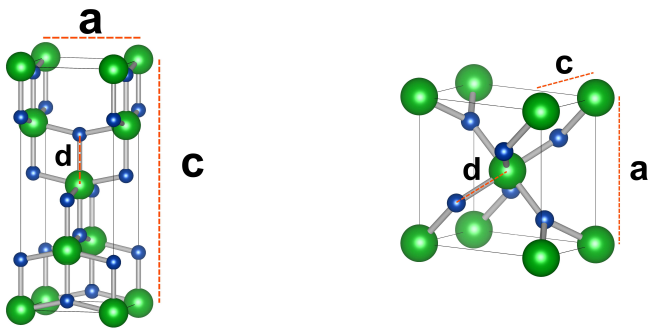

Figure 3.2: Anatase (left) and Rutile (right) TiO_2 unit cells. Oxygen atoms are blue, Titanium atoms are green. Lattice parameters (a & c) and bond length (d), as described in the text, are labelled.

Bulk anatase TiO_2 has a unit cell composed of four TiO_2 units, containing sixfold-coordinated titanium (Ti(6)) bonded to threefold-coordinated oxygen (O(3)) atoms. Differing Ti(6)-O(3) equatorial and apical bond lengths of 1.932Å and 1.979Å [98] produce distorted TiO_6 tetrahedra which can seen in figure 3.2. Lattice parameters a and c along with d, the apical Ti-O bond length, define the bulk structure.

	Anatase			Rutile		
	Expt. [98]	PBE [80]	This Work	Expt. [98]	PBE [80]	This Work
Lat. Param.						
a (Å)	3.782	3.786	3.817 (+0.9%)	4.587	4.587	4.602(+0.33%)
c (Å)	9.502	9.737	9.710 (+2.2%)	2.954	2.963	2.949(-0.17%)
d (Å)	1.979	2.002	1.954 (+1.1%)	1.976	1.999	2.005(+1.46%)
B_0 (GPa)	190	199	195(+2.6%)	210	204	212(+1.29%)
Ω (Å^3)	135.912	139.568	141.470(+4.1%)	62.154	62.248	62.448(+0.47%)

Table 3.1: Calculated and experimental lattice parameters and bond lengths of bulk anatase and rutile TiO_2. Values in brackets give the errors with respect to experiment.

Table 3.1 exhibits the calculated lattice parameters and bond lengths for the bulk anatase system. Good agreement can be seen between the experimental and calculated data, with the over-estimation of $\sim$1-2% typical of the GGA approximation within DFT.

Rutile has a smaller unit cell containing 2 $(TiO)_2$ units, and is also composed of distorted tetrahedra, with Ti(6) again bonded to six O(3) atoms. Differing equatorial and apical bond lengths of 1.946Å and 1.976Å respectively produce less distorted terahedra than in the anatase phase. Calculated rutile bond lengths and bulk parameters can also be seen in table 3.1.

Variation of the cell lattice parameters, by a simple multiplicative scaling in each direction, allows us to calculate the energy as a function of the volume, $E(V)$. Using $E(V)$ we can obtain the bulk modulus of the structure as:

$$B_0 = (V\frac{\partial^2 E}{\partial V^2}) \tag{3.1}$$

where B_0 is evaluated at the minimum value of $E(V)$. A plot of the function $E(V)$, obtained by varying the cell volume and fitting a cubic spline, for both phases can be seen in figure 3.3. The calculated bulk modulus of 195 GPa and 204 GPa for anatase and rutile are in very good agreement with experiment and previous studies.

Experimentally rutile is predicted to be the more stable of the two phases, however our results predict anatase to be more stable by around 0.05 eV per TiO_2 unit. This agrees with other studies[80], and has been suggested to be due to an incorrect description of correlation effects [99].

Having verified our method for the TiO_2 phases in bulk, the surface structures can now be examined with confidence.

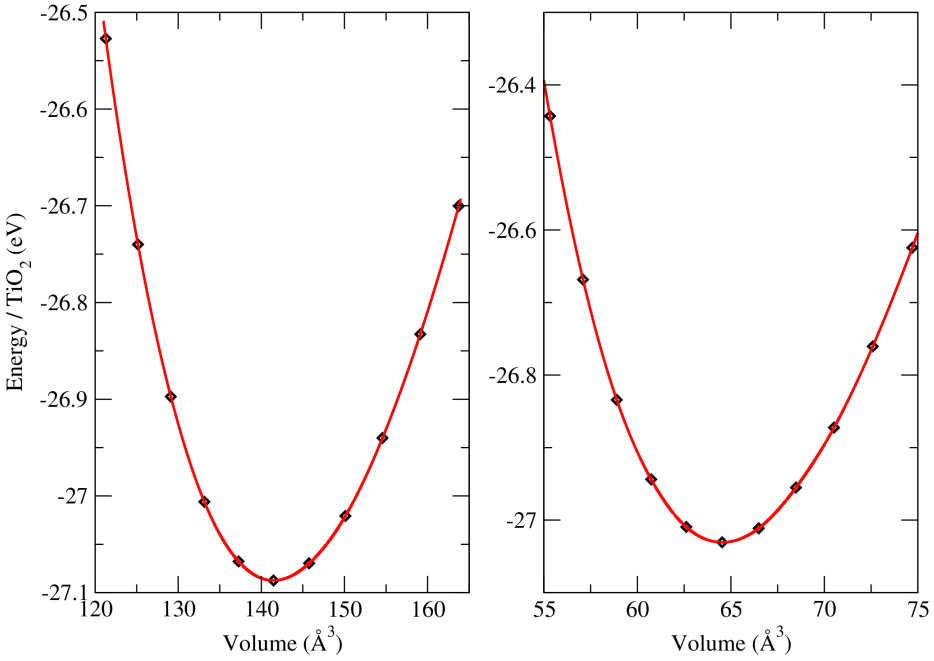

Figure 3.3: TiO_2 energy dependence on unit cell volume (Anatase left, rutile right), with cubic spline fitting of data.

3.4 TiO_2 Surfaces

Modelling surfaces within a plane wave DFT context requires the consideration of a few further points. In order to replicate a surface we wish reduce the periodicity in the direction parallel to its normal. By truncating the material along the surface plane, and extending the lattice in the normal direction we create a *slab* model of the surface. Increasing the size of the vacuum, and reducing the number of k-points in the corresponding reciprocal lattice direction, ensures that spurious interactions between periodic repetitions of the surface are minimised.

The same idea is true when wishing to model isolated molecules on this surface; using the supercell approximation and increasing the dimensions of the lattice in all three dimensions ensures interactions between periodic images of the molecule are reduced. In all surface and adsorption calculations the cell size is such that at least 9Å of vacuum separates periodic slab images (and adjacent molecules in adsorption calculations).

In order to obtain an accurate picture of the molecular adsorption at TiO_2 surfaces, it is important to converge the surface properties with respect to the number of layers in our slab model. In this section we characterise the anatase (101), anatase (001) and rutile (110) surfaces and converge the surface properties to an acceptable level so as to accurately examine the more computationally demanding molecular adsorptions yet to be performed with minimum computational effort.

For the surface and molecular adsorption calculations the lesser 450 eV cut-off has been used, along with a less stringent maximum force criterion of 0.03 $eV\text{Å}^{-1}$. Similarly the k-point mesh density has been reduced to 1 perpendicular to the surface. In order to replicate the bulk the bottom layer of the slab in all cases has been restrained to remain in the bulk position.

3.4.1 Anatase (101)

On formation of the stoichiometric (101) surface both fivefold-coordinated titanium (Ti(5)) and twofold-coordinated oxygen (O(2)) atoms become exposed. Also present in the topmost layer are O(3) and the less exposed Ti(6) atoms, figure 3.4.

The displacements resulting from surface relaxation in the [101] and $[10\bar{1}]$ directions of the topmost atoms for three and six layer slabs can be seen in figure 3.2. Most notable are the large outward displacement of the O(3ii) and inward displacement of the Ti(5) atoms in the [101] direction. A more jagged surface along the [010] direction, with the O(3ii) atom protruding beyond the Ti(5) atom, results.

Important also is the reduction in length and change of direction of the O(2)-Ti(6) bond,

from 1.95 (Å) to 1.87 (Å), as a result of the substantial outward [101] relaxation of the Ti(6) atom and large displacement in the $[10\bar{1}]$ direction of the O(2) atom. These surface characteristics reproduce well those found in other studies using the PBE functional [80].

Surface formation energies have been calculated by the subtraction of the bulk energy per layer times the number of layers from the total energy obtained, and dividing by the total exposed area, 2A (3.2a). Relaxed surface energies are then computed by subtraction of the energy change on relaxation per unit area from this unrelaxed surface energy (3.2b). Both relaxed and unrelaxed surface energies for slabs of varying thickness are presented in table 3.2(i).

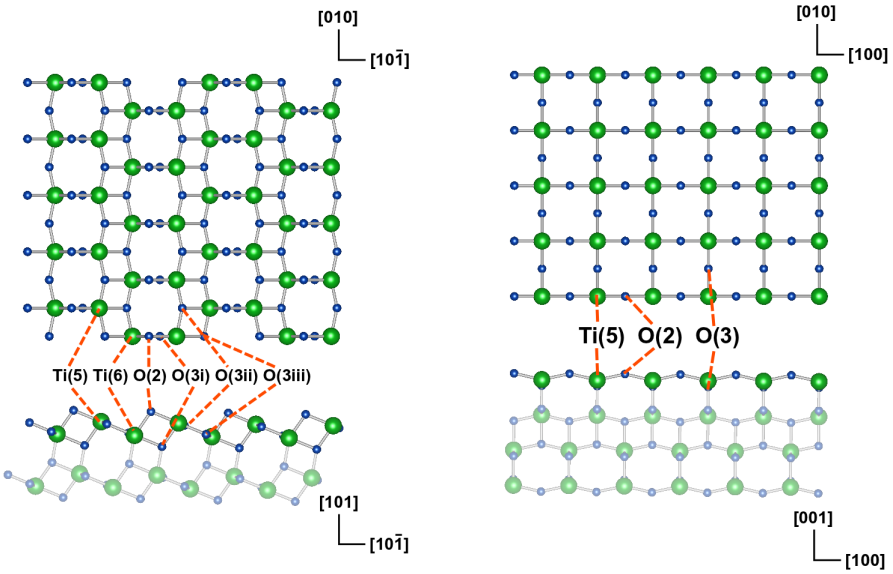

Figure 3.4: Anatase surfaces: (101) left and (001) right. Titanium atoms are green, oxygen atoms are blue. Both top views (top) and side views (bottom) are included, with coordination of surface atoms labelled.

$$E_{unrel} = \frac{1}{2A}[E_{un}^{Tot} - nE_{bulk}] \tag{3.2a}$$

$$E_{rel} = [E_{unrel} - \frac{\Delta E}{A}] \tag{3.2b}$$

For the six layer slab good agreement is found between the calculated unrelaxed (relaxed) surface energies of 1.267 J/m^2 (0.537 J/m^2) and that of previous work using the PBE functional, 1.28 J/m^2 (0.49 J/m^2) [80].

Unrelaxed (relaxed) surface formation energies for the three layer slab are found to be

converged to within 0.01 J/m^2 (0.015 J/m^2) with respect to that of the six layer slab. Although the convergence of relaxation displacements for the three layer representation are not as tight, it can be seen that the three layer model does qualitatively reproduce to a good degree the characteristic displacements found in the six layer slab. As a trade-off between computational ease and accuracy we have opted for the three layer TiO_2 (101) slab for the calculations involving adsorption of molecules.

	Surface Energy	
N_{lay}	E_{unrel} (J/m^2)	E_{rel} (J/m^2)
3	1.259	0.522
4	1.260	0.514
5	1.260	0.534
6	1.267	0.537

(i)

	Atomic Disp. (Å)	
Label	$[10\bar{1}]$	[101]
Ti(5)	-0.114 (-0.131)	-0.101 (-0.140)
Ti(6)	0.027 (0.012)	0.207 (0.154)
O(2)	0.140 (0.117)	0.017 (0.031)
O(3i)	0.031 (0.030)	-0.005 (-0.051)
O(3ii)	0.051 (0.030)	0.262 (0.219)
O(3iii)	-0.002 (-0.020)	0.081 (0.034)

(ii)

Table 3.2: **Anatase (101) Surface: (i)** Relaxed and unrelaxed surface energies for different layer anatase slabs **(ii)** Displacements from bulk position on relaxation of Anatase (101) surface for 3 layer slab (values for 6 layer slab are shown in brackets)

3.4.2 Anatase (001)

The unreconstructed (001) surface is reported to be much less stable than the (101) surface[80, 100]. However based on a Wulff construction it has been shown that for anatase nanocrystals, although comprising a much smaller area than the majority (101) surface, the (001) crystal face will still be exposed[80] in agreement with experiment.

Cleaving the anatase lattice perpendicular to the (001) surface exposes both two-fold and three-fold coordinated oxygen atoms, as seen in figure 3.4. In contrast to the (101) surface however, the O(2) atoms number ½ of those oxygen atoms exposed in the surface (for the (101) surface O(2) atoms make up ⅓). Similarly the (001) surface exposes only Ti(5) atoms, as opposed to the (101) surface which expose equal numbers of Ti(5) and Ti(6), as seen in 3.4. The high proportion of undercoordinated atoms in the (001) surface goes some way to explain its reported high reactivity[101, 102].

It is this high reactivity that makes the (001) surface of interest for many applications

such as photocatalysis and photo-degradation of organic molecules [102, 103, 104]. Recent work has shown that it is possible to increase the exposed percentage of the (001) surface by, for example, using hydrofluoric acid as a capping agent, thus improving its photocatalytic properties[103]. Similarly increasing the percentage of the exposed (001) face has been shown to improve DSSC performance[105]. Several reasons for this improvement have been suggested, such as the increased reactivity leading to higher dye adsorption, improved light scattering properties, and improved crystallinity leading to lower recombination rates [105, 106, 107].

Calculated surface energies for the (001) surface are presented in figure 3.3, and can be seen to be significantly higher than those of the (101) surface, as expected. Our calculated value of 1.145 J/m^2 (1.06 J/m^2) for the unrelaxed (relaxed) surface energy of the 4 layer slab is in good agreement with the result of 1.12 J/m^2 (0.98 J/m^2) reported elsewhere [80]. It can be seen that the relaxed surface energies are converged to within 0.004 J/m^2 for a four layer slab compared to those calculated for a seven layer slab, and we employ the four layer slab for the calculations involving molecular adsorption.

	Surface Energy	
N_{lay}	E_{unrel} (J/m^2)	E_{rel} (J/m^2)
2	1.172	1.053
3	1.220	1.054
4	1.145	1.060
5	1.146	1.060
6	1.144	1.055
7	1.144	1.056

(i)

	Atomic Disp. (Å)
Label	[001]
Ti(5)	-0.047 (+0.048)
O(2)	+0.046 (+0.034)
O(3)	+0.020 (-0.010)

(ii)

Table 3.3: **Anatase (001) Surface: (i)** Relaxed and unrelaxed surface energies for different layer anatase slabs **(ii)** Displacements from bulk position on relaxation of Anatase (001) surface for 3 layer slab (values for 7 layer slab are shown in brackets)

Atomic displacements for the surface atoms in the [001] direction are also given in figure 3.3, and agree well with previous work[80]. However the displacements reported for our ($1 \times 1 \times 3$) representation in the [100] direction are markedly different than those reported elsewhere; Selloni et al report a symmetry breaking of the Ti(5)-O(2)-Ti(5) bonds, with one Ti(5) bond extending to 2.20 Å and the other shortening to 1.76 Å. However, on increasing our

supercell for the adsorption of acidic binding groups (to $4 \times 3 \times 3$) we also find this symmetry breaking with the Ti(5)-O(2) bond lengths change to 2.20 and 1.78 Å. This symmetry breaking was seen for all cells used in molecular adsorption calculations and was not present in the smaller cell due to the reduced cell size.

3.4.3 Rutile (110)

Typical DSSC electrodes are composed of nanocrystalline TiO_2 particles, in anatase form. Grain boundaries between the crystals can lead to high rates of recombination and low electron diffusion coefficients. One potential approach to minimise this effect has been to construct single crystalline rutile nanorods, reducing the grain boundaries and improving electron transport[45] and also leading to increased surface areas, thereby improving dye take-up[46]. Grown along the [001] direction these nanorods expose a majority (110) surface for dye adsorption[89, 108], highlighting the importance of the interaction between the (110) surface and potential dye anchors.

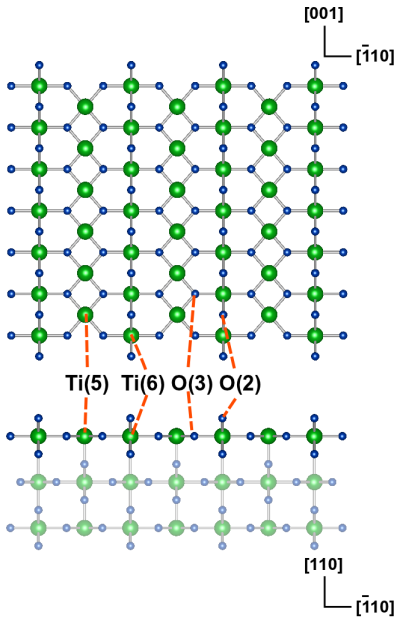

Figure 3.5: Rutile (110) surfaces: Titanium atoms are green, oxygen atoms are blue. Both top view (top) and side view (bottom) are included, with coordination of surface atoms labelled.

Forming a stoichiometric surface by truncating the bulk rutile structure along the [110] direction exposes both fully coordinated O(3) and undercoordinated O(2) atoms, as can be seen in figure 3.5. Similarly both fully coordinated and under-coordinated Ti(5) and Ti(6)

atoms are exposed. Calculated surface energies can be seen in 3.4. Our values for the 6 layer relaxed and unrelaxed surface energies of 1.298 and 0.254 J/m^2 are in good agreement with values of 1.38 and 0.35 J/m^2 reported elsewhere [80]. Significantly lower relaxed surface energies than that of both anatase faces suggest that the rutile (110) surface is considerably more stable, in agreement with other studies[80].

Convergence of surface energies with respect to slab thickness is seen to be much slower than is the case for both anatase surfaces. This can in part be attributed to an alternating bi-periodic layer structure; in the bottom of figure 3.5 it can be seen that the inclusion of each additional layer causes the position of the exposed O(2) along the [1$\bar{1}$0] direction to alternate, such that they coincide by layer with period two. It can be seen that the relaxed surface energies converge in an oscillating fashion, also with period two, as a result of this fact.

	Surface Energy	
N_{lay}	E_{unrel} (J/m^2)	E_{rel} (J/m^2)
3	1.384	0.290
4	1.338	0.255
5	1.321	0.418
6	1.298	0.254
7	1.277	0.324
8	1.282	0.210
9	1.233	0.268
10	1.210	0.210
11	1.189	0.235
12	1.165	0.193

(i)

	Atomic Disp. (Å)		
Label	[110]	Expt[109]	[1$\bar{1}$0]
Ti(6)	+0.125 (+0.217)	+0.25 ±0.03	0.000 (0.000)
Ti(5)	-0.211 (-0.190)	-0.19 ±0.03	0.000 (0.000)
O(2)	+0.076 (+0.003)	+0.10 ±0.05	0.000 (0.000)
O(3)	+0.112 (+0.143)	+0.17 ±0.08	+0.063 (+0.050)

(ii)

Table 3.4: **Rutile (110) Surface: (i)** Relaxed and unrelaxed surface energies for different layer rutile slabs **(ii)** Displacements from bulk position on relaxation of Rutile (110) surface for 3 layer slab (values for 11 layer slab are shown in brackets)

Comparing the relaxed surface energies for the three layer and eleven layer slab we can see that, although not as well converged as the anatase surfaces, convergence of 0.055 J/m^2 is obtained. Looking at the atomic displacements in table 3.4 we see that the three layer slab captures to a reasonable extent the significant Ti(5), Ti(6) and O(3) displacements in the [110] direction and as such we opt for the three layer slab model in the molecular adsorption

calculations in order to ensure a manageable computational load.

Rutile (110) is also known to form a 1×2 reconstruction following annealing at ~1100K[110]. However, in the formation of (110) dominated rutile nanorod DSSCs, the electrodes are annealed at $\sim$ 400-700K [89, 108] and thus we restrict our examination to the 1×1 surface.

3.5 Adsorption of Acidic Anchors

As mentioned previously the dye-semiconductor interaction is of fundamental importance to the science of DSSCs. Strong binding of the sensitising dye to the TiO_2 is essential for device stability, and this interaction proceeds mainly through the anchoring moiety. Similarly for efficient charge injection good electronic overlap of the dye and TiO_2 electronic states is required, upon which the anchoring group will have a significant bearing. Typically DSSCs utilise a carboxylic acid binding strategy, and while other anchoring groups have been used (and in some cases shown more desirable traits than their carboxylic acid analogues) the interaction of other anchoring groups with the increasingly important rutile (110) and anatase (001) surfaces have been much less rigorously examined. Previous works have examined formic acid adsorption on all three of these surfaces[111, 112, 113] and previous theoretical work has been done examining the adsorption of phosphonic acid on anatase (101) and rutile (110)[114, 115]. To the best of our knowledge at the time of writing no reports have been made on the binding of phosphonic acid to the (001) surface, and no reports have been made on the adsorption of the boronic acid group on any of these three surfaces.

In this section we study the interaction of three acidic binding groups with the anatase (101), the rutile (110) and the anatase (001) surfaces. Formic acid, the small molecule analogue of the carboxylic acid group most sensitising dyes utilised to anchor to the TiO_2, is examined along with the phosphonic and boronic acid groups, both of which have been used to bind dyes to TiO_2 electrodes. All three of these acidic binding groups can be seen in figure 3.6. While previous theoretical works have examined formic and phosphonic anchors on some of these surfaces, we repeat all of the calculations so that direct comparisons may be made between systems that have already been examined and those that have not.

All of these anchoring groups will have several different possible binding motifs with the TiO_2 surfaces, and in order to gauge the strength of interaction and find the most stable structure we must survey several of these possiblities. Some of the potential binding mechanisms of acidic anchors to TiO_2 are schematically illustrated in figure 3.7. Several of the binding motifs require the dissociation of the acid, in which case the dissociated hydrogen is adsorbed

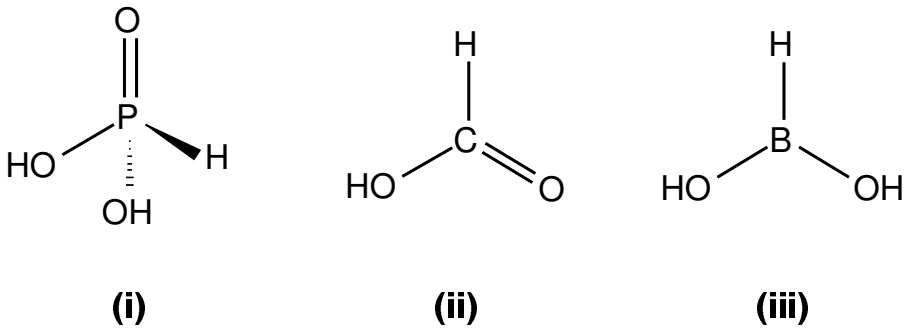

Figure 3.6: Acidic binding groups examined: (i) Phosphonic acid, (ii) Formic acid and (iii) Boronic acid.

on a nearby undercoordinated surface oxygen atom (not shown in the figure).

Calculation of binding energy between the acidic groups and the TiO_2 surfaces proceeds by taking a clean, relaxed surface slab and introducing the anchor molecule in an appropriate binding motif. The strength of the interaction is then calculated by subtracting the energy of the clean surface and the molecule from that of the total system:

$$E_{ADS} = E_{TOT} - (E_{SURF} + E_{MOL}) \tag{3.3}$$

In all instances the molecular energy is calculated for the molecule in isolation residing in a cell of dimensions the same as that of the composite system. Similarly the K-point sampling and energy cut-off are maintained constant for each of these calculations.

3.5.1 Anatase (101)

Calculated adsorption energies for all three acidic binding groups in several of the binding structures on the anatase (101) surface can be seen in table 3.5.

Our results illustrate that formic acid binds most strongly in the bidentate bridging mode, with the oxygens bonding to two adjacent Ti(5) surface atoms. An almost equivalent binding energy is obtained for the monodentate binding mode with a hydrogen bond (MON-H) to the nearest O(2) atom. A second monodentate binding mode is reported in which the hydrogen forms a weak bond with a O(3) surface atom (MON), with the adsorption energy being comparatively reduced. Finally the bidentate chelating mode (BIC) is found to be stable, but considerably less so than the monodentate and bridging modes.

Experimentally Fourier transform infrared spectroscopy report the coexistence of two dif-

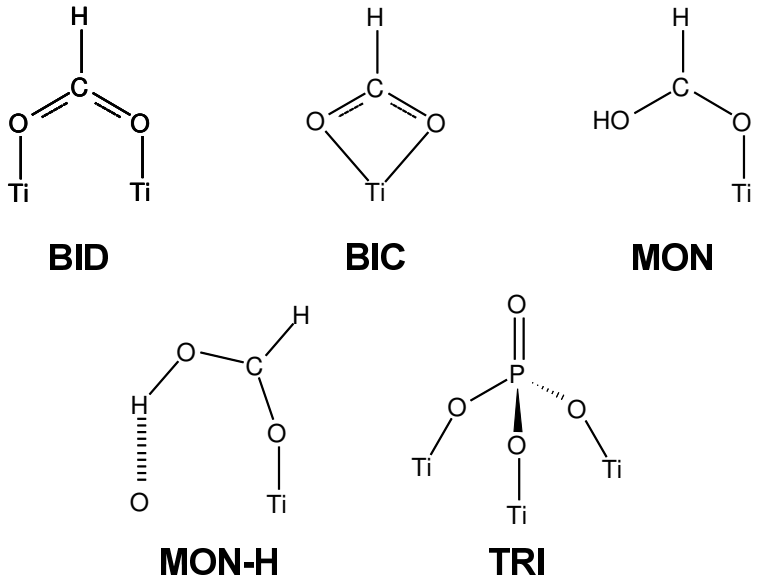

Figure 3.7: Binding Structures for Acidic Groups: Bidentate (BID), Bidentate-chelating (BIC), Monodentate (MON), Monodentate with hydrogen bond (MON-H) and Tridentate (TRI)(Phosphonic acid is the only anchor for which the tridentate mode is possible)

ferent adsorption structures, a bidentate mode and an unsymmetrical structure [116]. This is in agreement with our result that the monodentate and bidentate bridging modes are energetically similar and likely to coexist. Previous theoretical work has found the most stable structure to be the bidentate bridging mode, with the interaction of the hydrogen bonded monodentate mode extremely similar energetically[111].

Adsorbate	MON	MON-H	BIC	BID
Boronic	N/A	-0.72	+0.12	-0.82
Formic	-0.71	-1.02	-0.12	-1.03
Phosphonic	-1.29	-1.69	-0.48	-1.82

Table 3.5: Calculated adsorption energies for acids on the Anatase (101) surface (in eV.)

The phosphonic acid group has an extra degree of freedom in terms of its binding modes over formic and boronic acids, due to the extra oxygen atom it possesses. Numerous adsorption structures of similar binding modes are therefore available to it, and we report only the

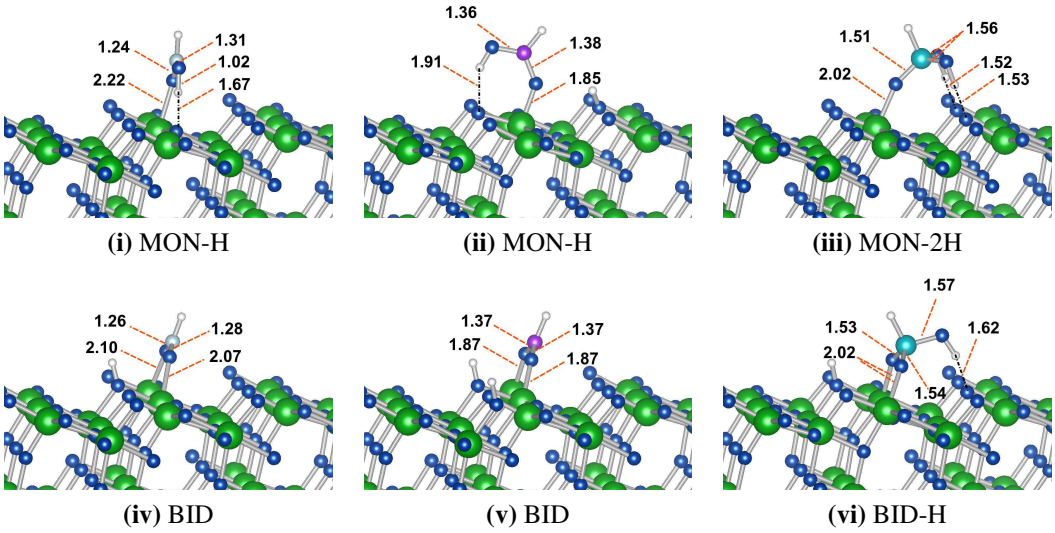

(i) MON-H **(ii)** MON-H **(iii)** MON-2H

(iv) BID **(v)** BID **(vi)** BID-H

Figure 3.8: Anchor adsorption structures on anatase (101): Two most stable adsorption structures for formic acid (**(i)** & **(iv)**), boronic acid (**(ii)** & **(v)**) and phosphonic acid (**(iii)** & **(vi)**)

most stable of each of these. Examining the results for phosphonic acid we see that overall it binds much more strongly to the surface in each of the given binding modes. The most stable adsorption mode for phosphonic acid is the bidentate bridging mode with an additional single hydrogen bond (BID-H Figure 3.8), in which two oxygen atoms of the acid group form bonds to two adjacent Ti(5) atoms in the surface, and the final OH group forms a hydrogen bond to an adjacent O(2) atom. A second comparably stable adsorption mode is found where the phosphonic acid binds through its carbonyl group, with the two OH groups forming hydrogen bonds to two adjacent O(2) atoms (MON-2H Figure 3.8). Previous studies have found similar results, with a DFT tight binding study finding the BID-H to be the most stable with the MON-2H structure being the only stable monodentate structure found after relaxation [114]. A second study found the two to be comparable in energy, but with the monodentate structure slightly more stable by 0.13 eV [115]. Our calculations do obtain further stable monodentate structures, all of which contain a single hydrogen bond irrespective of whether the hydrogen dissociates to reside on the nearest O(2) of the surface or not. Similarly to the previous works no stable tridentate binding mode was obtained.

Chemical adsorption of the boronic acid requires the dissociation of at least one hydrogen atom from either of its OH groups. From the results reported in table 3.5 we can see that its most stable structure is the bidentate bridging mode, similar to that of both the formic and phosphonic acid groups. However the strength of the interaction for this mode, and for

Adsorbate	MON	MON-H	BIC	BID-H	TRI (BID-H)
Boronic	-1.50	-1.83	-0.80	-2.56	N/A
Formic	-0.84	-1.61	-1.08	-2.27	N/A
Phosphonic	N/A	-2.35	-2.69	-3.22	-3.03

Table 3.6: Calculated adsorption energies for acids on the Rutile (110) surface (in eV.)

all others, is found to be significantly weaker than that of the formic acid and phosphonic acid groups. While it is still possible for the boronic acid group to form a stable bond, and therefore anchor dyes to the TiO_2 electrode, it certainly will be at a disadvantage in terms of device stability and dye take up over dyes anchoring through phosphonic and formic acid groups to the typical nanoparticle electrode dominated by the (101) anatase face. This result is in agreement with experimental work[85], in which TiO_2 sensitised with boronic acid groups gave low surface coverage, and resulting low IPCE values. Increasing the number of boronic anchoring moieties had the effect of increasing the surface coverage, and consequently the IPCE.

Stabilisation of the monodentate binding modes through hydrogen bond formation is another interesting feature, with the monodentate modes of both the formic and phosphonic groups being stabilised in such a way. Boronic acid also tended towards the formation of these hydrogen bonds when adsorbed in each of the monodentate modes investigated (again only the most stable of these is reported).

3.5.2 Rutile (110)

Examining the interaction of our binding groups with the rutile (110) surface (table 3.6) a different trend with respect to the interactions on the anatase (101) surface is immediately observed; In each binding mode the interaction of all three anchoring moieties with rutile (110) is considerably stronger than that with anatase (101). Our direct comparison of adsorption energies confirms this trend, which has been reported by proxy when comparing previous studies for formic acid adsorption on the (110) and (101) surfaces [117, 111] and for phosphonic acid [115, 87].

As with the anatase (101) surface, for each anchoring group the bidentate bridging mode is again found to be the most stable structure. However there is a contrast when comparing the relative stabilities of each mode, as on the (110) rutile surface the bidentate bridging mode

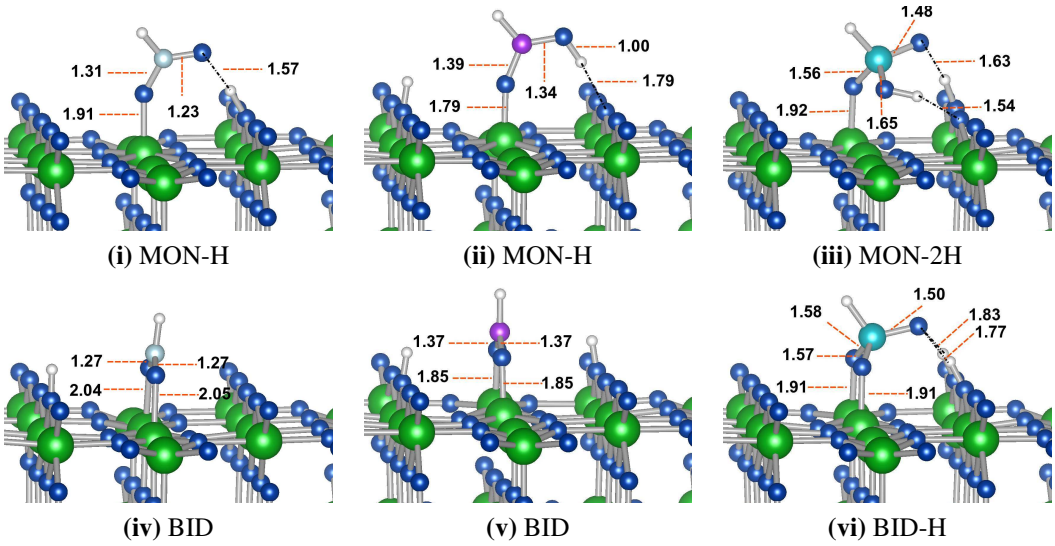

Figure 3.9: Anchor adsorption structures on rutile (110): Bidentate and monodentate structures for formic acid ((**i**) & (**iv**)), boronic acid ((**ii**) & (**v**)) and phosphonic acid ((**iii**) & (**vi**))

is considerably more stable than the most stable monodentate modes. Experimentally FTIR studies also find one binding mechanism for formate on rutile (110), which is identified as being the bidentate bridging mode by Hartree-Fock studies [118].

A further difference with the anatase (101) surface can be noted in the reordering of the relative binding stabilities of the anchoring groups. For the (101) surface the binding strength ordered such that phosphonic $>$ formic $>$ boronic. For the rutile (110) surface we find the ordering phosphonic $>$ boronic $>$ formic. This is a significant result, suggesting that dyes containing either phosphonic and boronic acids would have the ability to bind more strongly than carboxylic anchored dyes when adhering to the majority (110) surface exposed in rutile nanorod electrodes.

Both the formic and boronic acids bind in a very similar manner in their most stable modes, as can seen in figure 3.9. A notable difference in all anchors is the stabilisation of the chelating binding mode with respect to the (101) surface.

Addition of a hydrogen bond is found to stabilise the adsorption structure for all anchors. The phosphonic acid again differs in its binding modes slightly, due to its different molecular structure, and has more scope for forming hydrogen bonds than the other two anchors. In both of the phosphonic adsorption modes shown in 3.9, two hydrogen bonds are formed. Two dissociated hydrogen atoms, attached to O(2) surface atoms, coordinate to the single carbonyl group on the phosphonic acid in BID-H. In MON-H the hydrogen on the phosphonic OH

Adsorbate	MON-H	BIC	BID	BID2	TRI
Boronic	-1.69	-0.65	-0.66	-4.08	N/A
Formic	-1.96	-1.70	-0.73	-1.72	N/A
Phosphonic	-2.70	-1.82	-2.85	-3.21	-2.99

Table 3.7: Calculated adsorption energies for acids on the Anatase (001) surface (in eV.)

group coordinates to a single O(2) atom, along with the carbonyl group coordinating to the dissociated hydrogen. Similarly to the (101) surface no stable tridentate mode is found rather, when attemping to bind the phosphonic group in a tridentate structure, relaxation returns the mode to a BID-H structure, although a single hydrogen bond, marking the difference between the more stable BID-H structure (labelled TRI(BID-H) in table 3.6).

3.5.3 Anatase (001)

Similarly to the rutile (110) surface, the anatase (001) surface reconstructs to form a (1×4) termination in order to minimise the surface energy [119], and thereby becoming less reactive. Capping with hydrofluoric acid results in a fluorine terminated (1×1) surface which is more stable than the (101) surface. Using this capping agent it is possible obtain single crystals with extremely high percentages of the (001) surface exposed. There is some debate over whether the (001) surface retains its (1×1) termination after removal of the fluorine capping agent by thermal processing. Experimentally the crystals are reported as remaining unchanged[120], with a recent theoretical work showing that the process of removing the fluorine capping agent will result in the formation of the $(1 \times 4$ reconstruction[121]. We report here only results on the (1×1) surface termination, and view the study on the (1×4) reconstruction as an important future extension of the work.

Calculated adsorption energies for all three anchors on the (001) surface can be seen in table 3.7, along with selected adsorption structures in figure 3.10. Bidentate bridging can occur in two ways when the anchor binds to two Ti(5) atoms in the corrugated surface, with the anchor either bound above the O(2) atom (labelled BID in table 3.7) , or above the O(3) atom in the surface (labelled BID2 in table 3.7). For all anchors the binding is more stable when above the O(3) surface atom, this is as a result of the associated stress when the outward corrugation of the O(2) atom is reversed due to repulsion from the anchor binding above it.

High adsorption energies are indicative of the high reactivity of the (001) surface. This

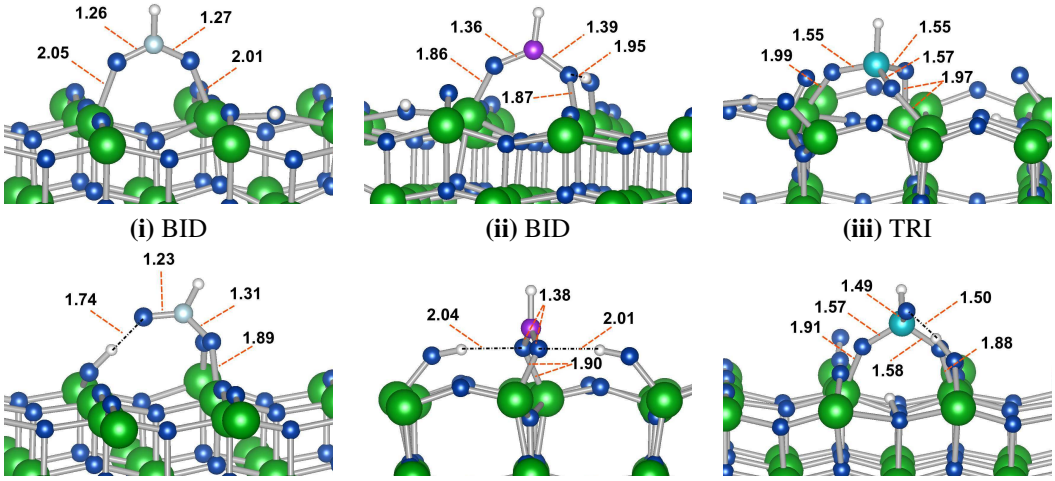

Figure 3.10: Anchor adsorption structures on anatase (001): Most stable adsorption structures for formic acid ((**i**) & (**iv**)), boronic acid ((**ii**) & (**v**)) and phosphonic acid ((**iii**) & (**vi**))

can also be seen in the tendency of the O(2) atoms to form surface -OH groups on addition of dissociated hydrogen atoms (see for example the boronic binding motifs in figure 3.10), a feature not present in either rutile (110) or anatase (101) surfaces. Another noticeable trait is the stabilisation of the bidentate chelating mode.

For the formic acid adsorption the monodentate structure is now found to be the most stable, with the bidentate bridging mode again similar in energy as it was for the (101) surface. However the chelating mode is now also found to be similar energetically. All three modes are more stable than for the (101) surface, but are not as stable as the most energetically favoured mode on the rutile (110) surface (bidentate bridging $E_{Ads} = -2.27$eV).

In the case of the phosphonic and boronic acids the most stable structures are again found to be the bidentate bridging modes (BID2) and the monodentate mode with hydrogen bond (MON-H). However, while the stability of these structures are similar for the phosphonic acid the boronic acid has much larger adsorption energy for the bidentate mode. Looking at figure 3.10(v) the BID2 mode for boronic anchor has, in addition to the usual bidenate O-Ti bond, the two dissociated hydrogen atoms, which have formed surface OH groups, also coordinating to the binding oxygen atoms. This goes some way to explain the stability of the system; moving one of these co-ordinating H-atoms to another O(2) atom further from the adsorbate, and thereby preventing it from forming a hydrogen bond with the binding oxygen atom, results in a 0.88 eV less stable structure.

Again we have the important result that a reorganisation of the most stable binding anchors occurs for this surface, giving us boronic $>$ phosphonic $>>$ formic, illustrating that *most* used carboxylic anchor is therefore predicted to have the *least* stable binding structure for the (001) surface and that the *least* used boronic anchor is predicted to have a *significantly stronger* binding structure than both phosphonic and formic acids.

We recognise the importance of performing these calculations on the reconstructed surface, in order to verify the impressive stability of the boronic-(001) surface coupling. However, irrespective of this, our results highlight a significant point when designing dyes for DSSCs; the anchor choice should necessarily depend on the majority surface exposed in the electrode. This is a particularly important point to consider at present, given the current trend of exploring and exploiting the properties of other electrode TiO_2 morphologies for which the (101) is no longer the dominant exposed surface. As a final point, the impressive binding of the boronic and phosphonic anchors to the unreconstructed (001) surface can be seen as making a strong case for experimentalists to find a way of exploiting its reactivity by functionalising the surface before any reconstruction can occur.

3.6 Chapter Summary

In this chapter we have introduced the two main TiO_2 polymorphs of interest for use as electrodes in dye sensitised solar cells, performing convergence studies and calculating the bulk properties for both. Following this introduction to TiO_2 bulk we have characterised three of the most important TiO_2 surfaces for use in DSSCs.

Examining the interaction of three binding anchors with each of these surfaces allowed us to compare and contrast the benefits of the most used carboxylic acid group with underused phosphonic and boronic anchors. Our results show that for each surface a reordering of the relative binding strengths of the anchors occurs. This highlights the important, but often neglected, point; that anchoring groups perform *differently* on different surfaces. Although somewhat obvious, this conclusion is a useful pointer to experimentalists working in the field and is something that should be taken into consideration when designing sensitising dyes. Finally the reactivity, and impressive binding strength of the anchors when attaching to unreconstructed anatase (001) surface is found to make a compelling case for experimentalists to exploit this reactivity by functionalising before surface reconstruction.

Chapter 4

Sensitising TiO_2: Dye Design

4.1 Introduction

Typically dye sensitised solar-cells (DSSCs) have been composed of a network of TiO_2 nanocrystalline particles upon which a dye is adsorbed [122]. Ensuring the highest occupied molecular orbital (HOMO) of the dye resides within the band gap of the semiconductor and the lowest unoccupied molecular orbital (LUMO) resides within the conduction band provides a photoexcitation pathway for electron transfer from the dye to the conduction band of the semiconductor. Reduction of the dye by interaction with a redox couple then regenerates the cell. Sensitising the semi-conductor to sunlight beyond its wide band gap UV range in this manner provides energetic access to the majority of photons arriving from the sun.

Ruthenium based dye sensitised solar-cells (DSSCs) have long provided the efficiency benchmark for current technology in the field, with efficiencies exceeding 11% operating under 1.5 A.M. solar irradiance [122, 123, 124], with zinc porphyrins more recently showing comparable efficiencies[10].

Organic chromophores by comparison offer potentially cheap, non-toxic and readily available alternative sensitisers. High molar extinction coefficients of organic dyes allow thinner semi-conductor films to be utilised [39] and the lack of expensive noble metals, such as Ruthenium, could result in considerably lower production costs. Notably organic dyes have also recently been used as coadsorbants, broadening the absorption range and leading to higher efficiencies [10, 125, 126]

Novel organic dyes based on coumarin [127, 128], merocyanine [129, 130], triphenylamine [131, 132], tetrahydroquinoline [133] and carbazole [134, 135], among others, have

been engineered and used successfully to sensitise TiO_2 in operational DSSCs. Recently efficiencies as high as 9.52 % have been achieved using indoline based dyes [39, 136], approaching those of the ruthenium based sensitisers.

Large efficiencies of the Ru(II) complex based solar cells have been attributed to an efficient metal to ligand charge transfer. A long charge separation period and the transfer of electrons into the π^* orbital of the ligand allows high injection rates from the carboxylate group into the TiO_2 conduction band. Coupled with the wide absorption range of the sensitisers results in the high efficiencies produced [122, 123, 124, 137, 138].

Efficiency improvements in organic DSSCs have been pursued through a wide variety of efforts, with molecular design of dyes possessing desirable characteristics being one of the main avenues of investigation. The properties of their Ru based counterparts have informed the design of organic chromophores with common desirable traits, including a) strong binding to TiO_2 b) intramolecular charge separation c) broad absorption spectra in the visible to near infrared range of the solar spectrum.

Intramolecular charge transfer can be achieved through the separation of an electrophobic donor and electrophilic acceptor group within the dye by way of a π linker, in D-π-A structures. Increasing the conjugation length of the π linker can also red shift the absorption spectra, increasing the short circuit current of the cell. Short circuit current improvements are often translated into cell efficiency increases. For example, Kim and coworkers produced an increase in the short circuit photo-current density of 1.2 mA/cm^2 through the extension of a conjugated linker, between a di-methylfluorine containing donor and a cyanoacrylic acid acceptor, by the introduction of an additional thiophene unit [44]. A resulting increase in efficiency of 0.81% was obtained.

Due to the relative stability of its conjugated ring structure and its tunable optical properties, thiophene is one of the most widely used linker moieties [127, 128, 131, 132, 133, 139, 134, 135, 44, 140]. Hara et al. have reported a similar response to that of Kim and co-workers on introduction of an additional thiophene moiety into coumarin dyes [127, 140].

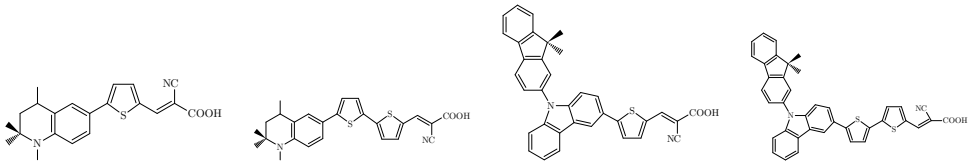

C2-1 **C2-2** **JK-24** **JK-25**

Figure 4.1: Tetrahydroquinoline chromophores, (C2-1, C2-2) and Carbazole chromophores, (JK-24, JK-25)

Counter-productively, extending the conjugation in this manner can also produce dyes with the tendency to form aggregates. Detrimental effects of π-stacked aggregates are well known, with intermolecular interactions reducing the charge transfer efficiency [129]. Molecular design of dyes [141], as well as the strategic use of co-adsorbents[142] have been employed to reduce the effect of aggregation and improve efficiency by way of limiting monolayer coverage and dye-dye interaction.

This chapter focuses on the DFT description of the adsorption interaction of D-π-A chromophores containing thiophene linker moieties with the anatase TiO_2 (101) surface. Chromophores containing electron donating tetrahydoquinoline (C2-1, C2-2) and carbazole (JK-24, JK-25) groups (all shown in figure figure 4.1) have been examined, with the cyanoacrylic acid group acting as electron acceptor. Differences in chemical composition between dyes of the same class is limited to an additional thiophene linker moiety in the bridge between the donor and acceptor groups. Extension of the thiophene chain in this manner forms one of the most widely used design mechanisms to improve the charge separation and absorption properties of DSSCs, and our investigation allows for systematic examination of its effectiveness. Surface coverage effects on the electronic structure and adsorption characteristics are also examined, which also allows us to ascertain the effect of increased conjugation length on dye aggregation.

4.2 Computational Details

All calculations were performed within a density functional theory framework, in a plane wave basis, using the VASP code [143]. Electron exchange and correlation was treated within the generalised gradient approximation of Perdew and Wang [144] and the pseudopotential method was utilised in the form of ultrasoft Vanderbilt pseudopotentials [145] to treat core electrons. For Titanium atoms the $4s^2 3d^2$ electrons are treated as valence electrons, for oxygen, carbon and nitrogen the 1s electrons are treated as being in the core. Sulphur atoms are treated with the $1s^2 2s^2 2p^6$ electrons considered to be in the core.

Bulk anatase TiO_2 calulations were carried out with a Monkhorst-Pack k-point mesh of (6,6,4) and a plane wave cut-off of 400 eV. Bulk lattice parameters were obtained by allowing ion position, cell shape and volume to vary throughout minimisation.

Modelling of the TiO_2 (101) surface utilised a slab model in which the periodic nature of the VASP code was used to represent the system in the $[\bar{1}01]$ and the [010] directions. In the [101] direction the system was represented as periodic repetitions of the (101) surface, two of

which can be seen in figure 3.4, with a vacuum buffer region of 15Å between slabs.

For monomer chromophore adsorption on the (101) surface the TiO_2 system size was increased in the $[\bar{1}01]$ and [010] directions so as to accommodate the chromophores with distances of at least 8Å separating the images in all three periodic directions.

Surface and monomer adsorption calculations were performed using a Monkhorst-Pack k-point grid of (2,2,1) throughout with a cut-off of 400 eV. Relaxations of both the isolated surfaces and the adsorption geometries proceeded by fixing the bottom substrate layer to the relaxed bulk positions and allowing remaining layers, along with the chromophore, freedom to move. Efficient relaxation was carried out by damped molecular dynamics at a temperature of 300 K, followed by a structural relaxation using the residual minimization method with direct inversion in the iterative subspace (RMM-DIIS)[146] until the forces on free ions were less than 0.03 eV/Å. For calculations of partial density of states the k-point mesh density was increased to (4,4,1).

We also examined the effect of monolayer coverage (or as close to monolayer coverage as dye dimensions would permit) by reducing the cell size in order to allow the interaction between the periodic images of the chromophores. Monolayer coverage of the (101) surface by the tetrahydroquinoline dyes was achieved using a $1 \times 2 \times 3$ slab in the [110], [010] and [101] directions respectively, with stoichiometric configuration $[TiO_2]_{12}$. The larger carbazole dyes were accommodated upon a $1 \times 3 \times 3$ slab in the respective directions, equivalent to $^2/_3$ monolayer coverage.

Semi-local approximations such as the GGA are known to incorrectly describe the long-range interactions responsible for aggregation effects[147]. Recently pioneering work on a generally applicable van der Waals density functional (vdW-DF) have shown considerable success in describing these non-local effects[148, 149, 150, 151]. In order to obtain an accurate description of the intermolecular interactions in the monolayer adsorption mode, non-local contributions from the vdW-DF are taken into account. A post-hoc correction is calculated through the application of the JUNOLO[152] code to the generated VASP charge densities.

4.3 Chromophore Adsorption on (101) Surface

4.3.1 Binding Mode and Adsorption Geometry

Numerous deprotonation and binding modes exist between the anchoring carboxylic acid group and the anatase TiO_2 (101) surface. Fourier transform infrared absorption spectra have suggested that both inorganic and organic chromophores adsorb onto the TiO_2 surface via a

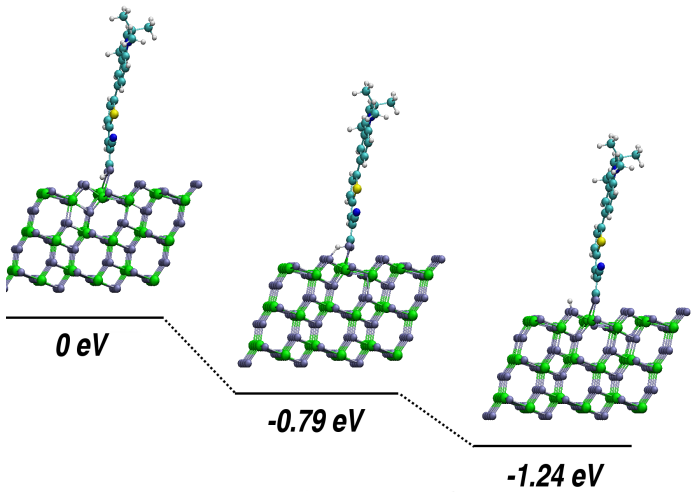

(i)

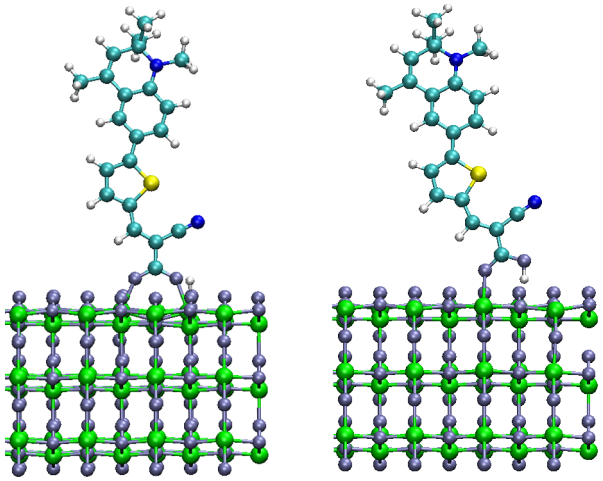

(ii)

Figure 4.2: (i) C2-1 deprotonation pathway on chromophore adsorption. (ii) Chromophore binding modes: bidentate bridging(left) and monodentate(right).

bidentate bridging mode[153, 154]. Taking C2-1 as a test case we have carried out several calculations to illuminate the binding mechanism.

Figure 4.2(i) illustrates the deprotonation pathway of the carboxylic acid group on adsorption to the TiO_2 surface in a bidentate bridging mode. Initial adsorption has the OH group intact, followed by an intermediate state in which the hydrogen is shared between the O atoms on the carboxylic acid and TiO_2 surface. Finally the hydrogen is completely transferred to the surface, with an energetic gain of -1.24 eV.

Comparison of the monodentate and bidentate bridging adsorption mechanisms have also been made, figure 4.2(ii). In agreement with the literature [153, 154] the bidentate bridging mode is favoured by -0.37 eV. Given the similar anchor and bridge structure for all chromophores we use this hydrogen dissociated, bidentate bridging mode to model the chromophore-TiO_2 interactions. In this mode oxygens from the carboxylic acid group form a bridge through bonds with two Ti(5) atoms adjacent along the [010] direction, as seen in figure 4.2, and we have placed the dissociated hydrogen on the closest O(2) atom. It is also worth noting that spin-polarised calculations have been carried out for C2-1 in this mode, and are found to be in agreement with the spin unpolarised case.

Simulating monolayer adsorption by the reduction of the cell size results in a system with reduced degrees of freedom, as the chromophore will in fact interact with periodic images of itself. In order to justify this method we have performed calculations, again with C2-1, in which monolayer adsorption was simulated by two chromophores adsorbed on a $2 \times 2 \times 3$ slab in the [110], [010] and [101] directions respectively, with stoichiometric configuration $[TiO_2]_{24}$. Different relative orientations of the dyes in this two chromophore monolayer representation were investigated, with the geometry of the most stable orientation found to be well represented by the single chromophore unit cell figure 4.3 (electronic structure was also found to be well represented). MONO adsorption geometries in all cases were found to be very similar to the relaxed ISOL structure (e.g. figure 4.8(i)).

4.3.2 Adsorption Energies

Adsorption energies were calculated by subtraction of the clean surface energy and the isolated molecule energy from that of the total system, and are illustrated in figure 4.1. Large conjugated molecules are well known to aggregate as a result of $\pi - \pi$ interactions. In order to evaluate the effect of increasing the conjugation length a post-hoc vdW correction for the addition of a thiophene linker moiety to both C2-1 and JK-24 monolayer calculations are also presented in figure 4.1. This correction can be seen as the increased dye-dye interaction on

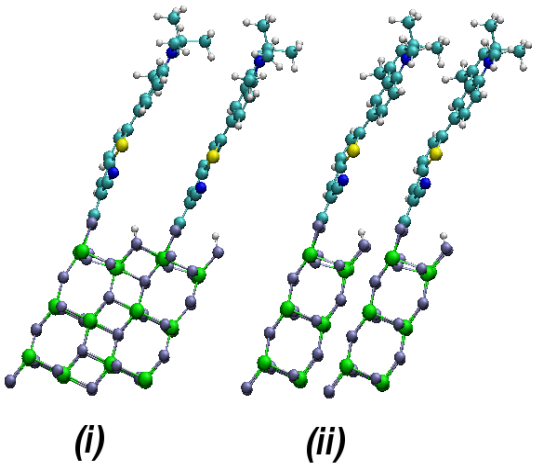

Figure 4.3: Relaxed adsorption geometry for (i) two chromophore and (ii) one chromophore representations of monolayer coverage C2-1.

addition of a thiophene linker moiety and is calculated for the C2 (JK) dyes as follows:

$$E^{vdW}_{+Thio} = (E^{vdW}_{tot} - E^{vdW}_{dye} - E^{vdW}_{surf})_{2T} - (E^{vdW}_{tot} - E^{vdW}_{dye} - E^{vdW}_{surf})_{1T} \qquad (4.1)$$

where the 2T and 1T subscripts refer to C2-2 (JK-25) and C2-1 (JK-24) respectively and E^{vdW} is the energy calculated with the vdW-DF for the VASP generated charge distribution using the JUNOLO code[152].

A prominent trend is observed, that the effect of increasing the dye coverage is much more pronounced than that of extending the thiophene chain. Monolayer adsorption energies are seen to be significantly larger than that of the isolated chromophores, $E^{Ads}_{MONO} > E^{Ads}_{ISOL}$. As a consequence a reduction in adiabatic electron transfer, due to smaller electronic coupling of the dye and substrate states, as well as overall stability of the DSSC could be expected if the monolayer adsorption mode was predominant.

It can be seen that, although isolated dyes on the surface are preferential in all cases, monolayer coverage is also energetically possible. Indeed the adsorption energies for the C2-2 ISOL and MONO are comparable when the vdW correction is taken into account. Our result that the C2-2 monolayer calculation is more energetically favoured than that of C2-1 is reinforced by this vdW-DF correction, which shows that the addition of a thiophene moiety to the π linker produces an increased favourable dye-dye interaction of 0.113 eV. Increased stabillity as a result of the larger conjugation length of C2-2 also inhibits the deformation of the thiophene chain when adsorbed onto the surface. Selected dihedral angles within both chromophores

Dye	ISOL (eV)	MONO (eV)	δE vdW (eV)
C2-1	-1.137	-0.834	–
C2-2	-1.186	-1.063	-0.113
JK-24	-1.174	-0.653	–
JK-25	-1.210	-0.696	+0.007

Table 4.1: Adsorption energies of monolayer (MONO) and monomer (ISOL) dye interactions with (101) surface and the Van der Waals correction for adding an extra thiophene moiety to the π linker (vdW).

adsorbed on the surface are exhibited in figure 4.4, and the difference in E^{Ads}_{MONO} of around -0.23 eV can be attributed to the slight deformation of the planar structure of the thiophene linker of C2-1, when compared to C2-2.

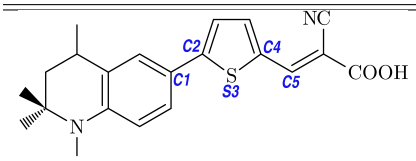

C2-1

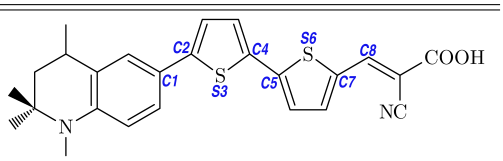

C2-2

C1-C2-S3-C4	-176.50	C1-C2-S3-C4	-177.92
C2-S3-C4-C5	173.88	C2-S3-C4-C5	-179.90
		C3-C4-S5-C6	-179.69
		C4-S5-C6-C7	-179.09

Figure 4.4: **Selected Dihedral Angles (deg):** C2-1 and C2-2 MONO adsorption on anatase (101) surface

Experimentally two alternative approaches for the two classes of dyes have been undertaken to hinder aggregation. Chen et al. have employed the addition of a co-adsorbent, chenodeoxycholic acid (CDCA), to inhibit the aggregation of the tetraquinoline dyes [133]. A larger change in J_{sc} for the C2-2 DSSC (9.82 mA/cm^2$\rightarrow$ 12.0 mA/cm^2) was observed than that of C2-1 DSSC (11.3 mA/cm^2$\rightarrow$ 11.2 mA/cm^2), suggesting the increase in thiophene chain length produced an increase in dye aggregation. Our result is in agreement with the experimental evidence, showing that the larger the conjugated π system the more likely is ordering into π stacked aggregates on the surface.

Design of non-planar dyes can be used as an alternative method to inhibit aggregation. Addition of the non-planar dimethylfluorene moiety to the carbazole dyes by Kim et al. is an example of this design[135] technique. A larger increase in adsorption energy on moving from monomer to monolayer coverage for the JK dyes than that of the C2 dyes would suggest that this is effective to an extent. An increased tendency towards aggregation with larger thiophene linker size is also inhibited by this non-planar structure, as seen in the similar decrease in adsorption energies of both MONO and ISOL carbazole calculations on addition of an extra thiophene group as well as the small positive vdW correction for thiophene addition.

4.3.3 Electronic Structure

Donor-π-acceptor dyes are designed with two main characteristics in mind. Firstly, excellent intramolecular electron transfer properties are exploited to bring excited charge towards the surface, increasing overlap between the dye-LUMO and LUMO orbitals on the substrate and thereby improving charge injection. Secondly, extension of the conjugated chain can red-shift the absorption spectrum, improving the light harvesting capacity of the cell [140, 142].

Sensitising the TiO_2 substrate to light beyond its UV range forms the main operating principle for DSSCs and requires the introduction of occupied states in the band gap. Partial density of states for the tetrahydroquinoline and carbazole dyes are illustrated in figures 4.5 and 4.6 respectively, showing that adsorption of all chromophores in both monolayer and monomer calculations result in occupied states appearing in the TiO_2 band gap. Introduced band states are localised exclusively on the chromophore with the lowest unoccupied molecular orbitals for all systems found to be located in $3d$ orbitals on the titanium atoms throughout the substrate (not illustrated).

Extension of the thiophene linker can be seen to produce a positive energy shift of the HOMO levels within the gap for all adsorptions, with a slight shift towards the conduction band of the dye-LUMO levels. However these shifts are much less dramatic than the effect on the electronic structure of increased dye coverage in moving from ISOL to MONO calculations. While the orbital characters remain essentially the same, the occupied states on the chromophore undergo a significant negative energy shift, widening the HOMO-LUMO gap by approximately 0.64 eV for both C2-1 and C2-2, 0.62 eV for JK-24 and 0.56 eV for JK-25. As a result of this shift a reduction of the number of states in the gap occurs for all systems. This result echos the trend in the adsorption energies, that dye concentration has a much more significant impact than conjugation length.

Adsorption of dipolar dyes on TiO_2 surfaces has been shown to shift both the substrate

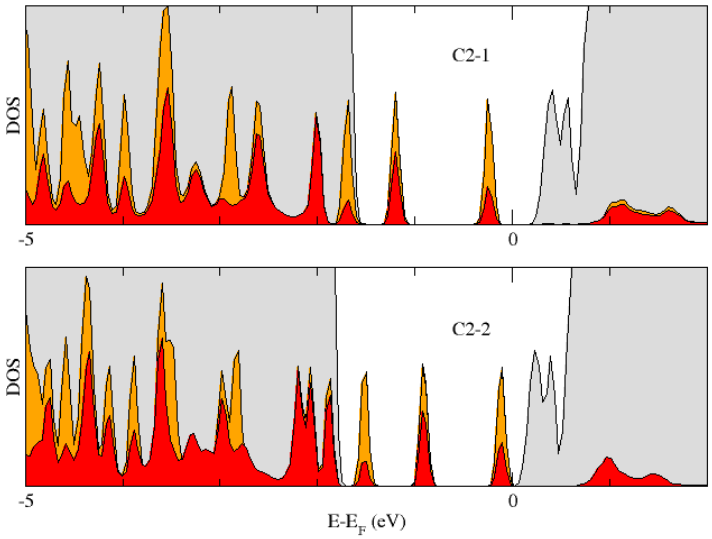

(i)

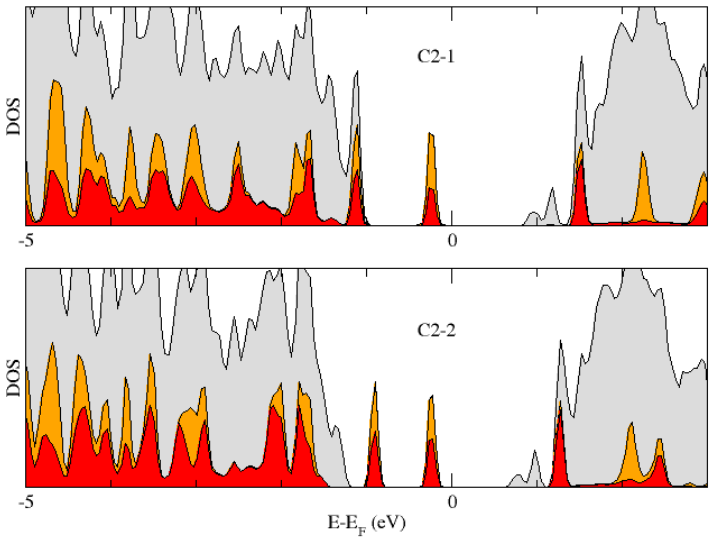

(ii)

Figure 4.5: Partial DOS: Projection on π-A and carboxylic acid anchor group (red), total chromophore (orange), total system (grey) of the tetrahydroquinoline dyes adsorbed on the Anatase (101) surface: (i) ISOL (ii) MONO

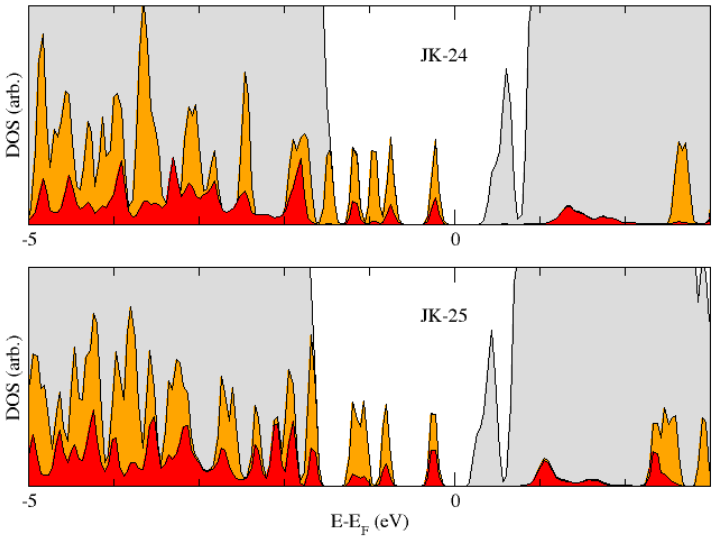

(i)

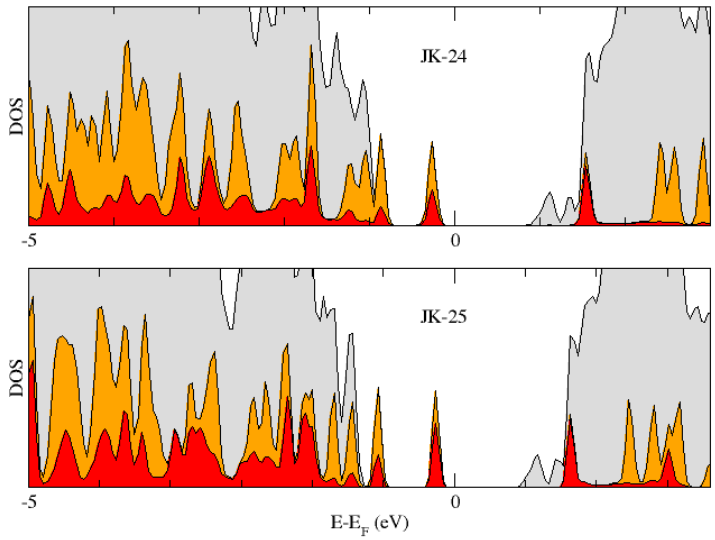

(ii)

Figure 4.6: Partial DOS: projection on π-A and carboxylic acid anchor group (red), total chromophore (orange), total system (grey) of the carbazole dyes adsorbed on the Anatase (101) surface: (i) ISOL (ii) MONO

valence and conduction bands[155]. Calculation of the dipole moments for the respective dyes along the [101] direction (C2-1 = -9.5 D, C2-2 = -10.2 D, JK-24 = -7.3 D, JK-25 = -8.9 D) might suggest that the influence of the dipolar fields could shift the substrate energy levels and be responsible for the difference in ISOL and MONO electronic structure. Figure 4.7 illustrates that although the adsorption of the dipole dyes does induce a shift in the substrate energy levels, this shift is similar for both the ISOL and MONO adsorption cases (similar results were obtained for the JK dyes).

Bond breaking and formation on dye adsorption on the TiO_2 surface has an associated charge rearrangement. Considering this charge rearrangement on dye adsorption as that of the total system minus that of both the isolated dye and surface:

$$\Delta\rho(\mathbf{r}) = \rho_{tot}(\mathbf{r}) - (\rho_{dye}(\mathbf{r}) + \rho_{surf}(\mathbf{r})) \tag{4.2}$$

it is possible to examine the charge reconstruction on dye adsorption. Figure 4.8(i) shows this charge reconstruction for C2-2, and it can be seen that both the ISOL and MONO cases are extremely similar. Plane-integrated charge transfer along the [101] direction is also shown, figure 4.8(ii), and again little difference between the two is found (similar ISOL and MONO charge reconstructions for all dyes were obtained). Coupled with the similar dipole-induced substrate band shifts for MONO and ISOL this would suggest that the electronic structure change on increased surface coverage is not a function of the dye-substrate interaction, but rather a dye-dye interaction.

We now describe a simple method we have employed to examine the dye-dye interactions. Taking the relaxed MONO geometry, reassociating the hydrogen and removing the TiO_2 surface produces a molecule only monolayer. Rescaling the unit vectors of the cell in the [010] and $[10\bar{1}]$ directions with a constant factor increases the dye separation, thereby causing the system to approach the ISOL limit. We have examined the behaviour of these molecule only monolayers as they approach the ISOL limit in two cases. Firstly the single MONO unit cell corresponding to parallel dipoles D1 - figure 4.9(i). Secondly a $3x3$ unit cell containing nine chromophores, with one of the dyes rotated such that the dipole is anti-parallel to the others - D2 figure 4.9(i). HOMO energy levels for each of these configurations with the C2-2 dye are presented in figure 4.9(iii). HOMOs are seen to converge towards the same value as the dyes approach the ISOL limit. In the MONO limit (scaling factor = 1.0) there is a distinct difference in HOMO energy levels. For the D2 configuration the HOMO was found to reside

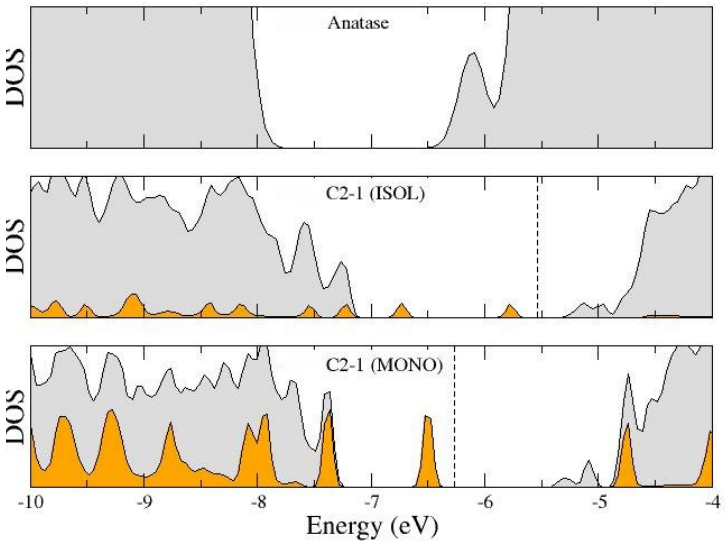

(i)

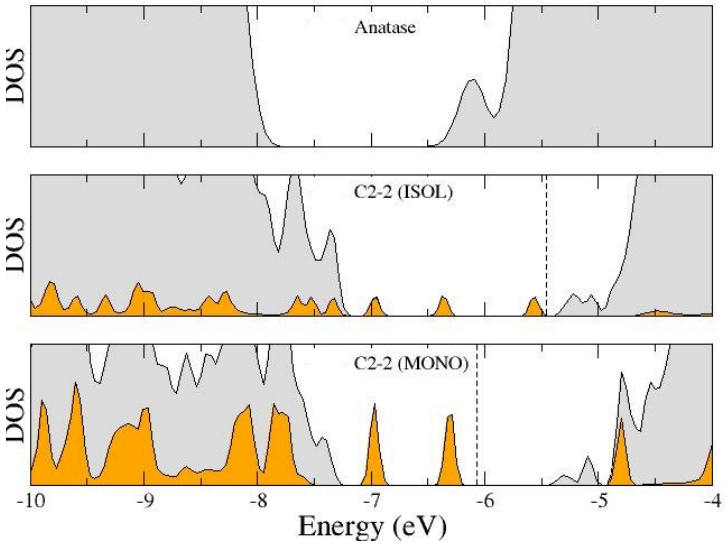

(ii)

Figure 4.7: Dipole induced shift of substrate energy levels: DOS for clean anatase (101), ISOL and MONO adsorptions for (i) C2-1 (ii) C2-2. Projection on adsorbed chromophore in orange.

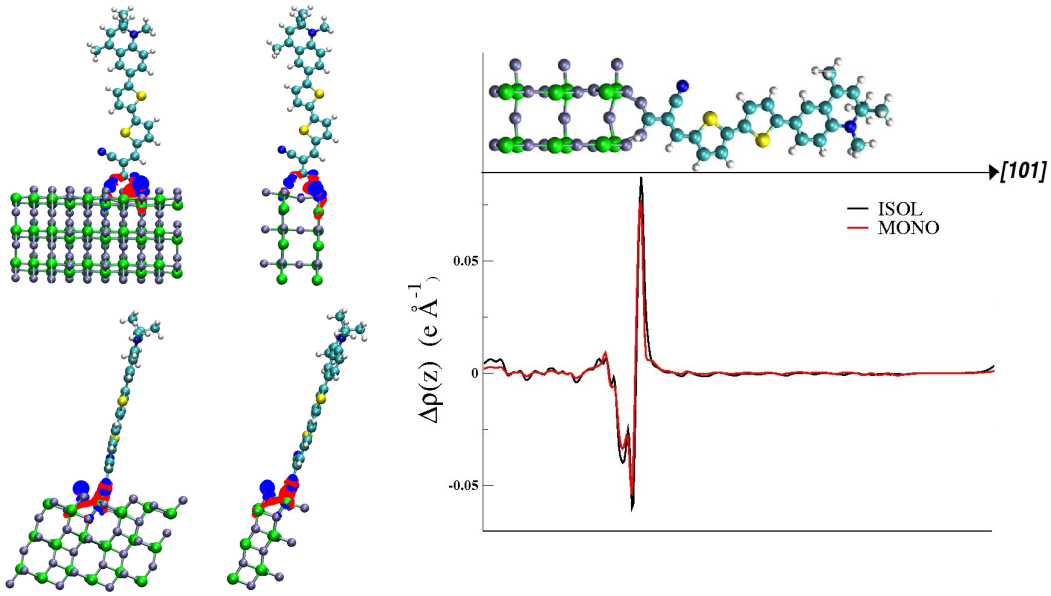

Figure 4.8: (i) Charge reconstruction isosurface at 0.05 e/Å^3. Charge increase in blue, depletion in red. (ii) Plane integrated charge transfer along the [101] direction, $\Delta\rho(z)$. MONO structure aligned with axes as guide for the eye.

exclusively on the central dye with opposite dipole moment. This HOMO was considerably above the HOMO-1 level, which for each case was localised on one of the eight remaining dyes with parallel dipole moments. The downward shift of the D1 HOMO as the MONO limit is approached can be seen to result from the dye residing in the dipolar field of the adjacent dyes. Indeed when this dipolar field is reversed, as is the case for the central dye in the D2 configuration (and to a lesser extent the remaining eight dyes) the HOMO is shifted positively (HOMO-1 is also shifted upwards, but to a lesser extent).

Dye concentration on the surface has a much larger impact than dye structure on the electronic properties, however the effect of increased conjugation is not insignificant. For the C2 dyes the small positive shift due to conjugation extension increases the number of occupied states residing in the gap in both MONO and ISOL calculations. Experimentally the red shift of λ_{max}^{Abs} on increasing the thiophene chain for the C2 dyes is found to be 24 nm [133], corresponding to a shift of 0.1 eV. This is in good agreement with our HOMO shift of 0.16 eV for the MONO calculations (0.24 eV for ISOL). An additional shoulder in the absorption spectra at a shorter wavelength found for the C2-2 dye when compared to the C2-1 dye by

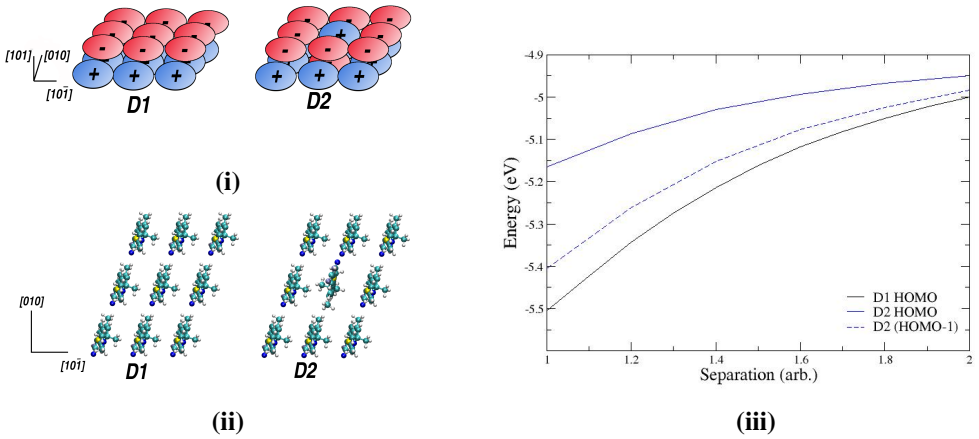

Figure 4.9: Molecule only monolayer for C2-1: (i) Schematic showing molecule dipole orientations: all parallel (left:D1) and one Antiparallel (right:D2). (ii) Molecule only monolayer structures from above (separation = 1.2). (iii) HOMOs for C2-1 molecule only monolayer structures D1 and D2 for differing separation along the [010] and $[10\bar{1}]$ directions. Separation is given as a scaling factor of the separation in the original MONO unit cell.

Chen et al. also corresponds well to our observation that in the MONO calculation an additional unoccupied state has been introduced into the gap. Chen et al. have synthesised the tetrahydroquinoline dyes, C2-1 and C2-2, and measured the efficiency of DSSCs based upon them as 4.49% and 4.53% respectively under AM 1.5 irradiation [133]. The slight increase in efficiency of the C2-2 dye over C2-1 was attributed to a broadening of the IPCE (incident photon to current efficiency) action spectrum, for which the increased number of states within the band may be a contributing factor.

In the case of the JK dyes the positive HOMO energy shift as a result of the additional thiophene linker does not introduce extra states in the band gap. A slight bunching of the HOMO levels from JK-24 to JK-25 in the ISOL calculations is observed and a shift of the HOMO-1 level in the MONO calculation occurs, so that it resides more clearly in the gap. Kim et al. have measured experimentally the red shift of λ_{max}^{Abs} as a result of an additional thiophene group to be 27 nm., corresponding to 0.17 eV. Our calculated HOMO shift of 0.16 eV for the ISOL calulation is in good agreement with this value (0.9 eV for MONO). Kim et al. have synthesised and measured the efficiency under AM 1.5 irradiation of the carbazole containing dyes, JK-24 and JK-25, as 5.02 % and 5.15% respectively [135]. Extension of the thiophene chain again showing a small increase in efficiency.

Several competing processes are at work in a DSSC, making the improvement of cell ef-

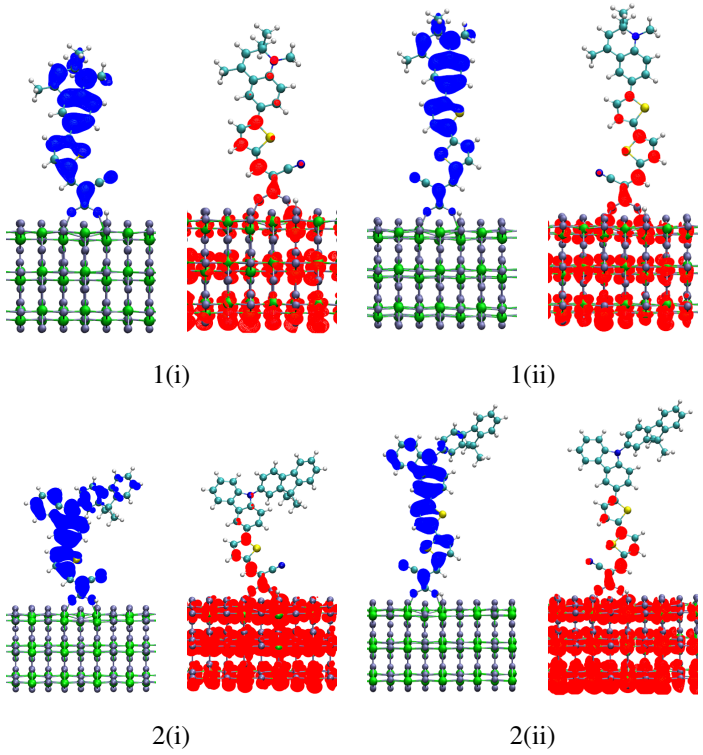

Figure 4.10: Isosurfaces of band decomposed partial charge distribution 0.05 e/Å^3: HOMO (blue) and Dye-LUMO (red) partial charge distributions for C2-1: 1(i), C2-2: 1(ii), JK-24: 2(i) and JK-25: 2(ii)

ficiency a complex balancing act. An appropriate driving force is required in order to ensure oxidation of the electrolyte and the regeneration of the cell. Increasing the thiophene conjugation will therefore have two effects. Introducing extra states in the band gap will broaden the absorption spectra, having a positive effect on the IPCE. However the positive shift of the HOMO will also reduce the effective driving voltage for cell regeneration as well as increase the undesirable charge recombination. Further extension of the conjugation of the C2 group of dyes by an additional thiophene unit produces a marked reduction in efficiency for the C2-3 chromophore[133], which could be due to this reduced driving voltage and increased aggregation effects.

Examining isosurfaces of the band decomposed partial charge distributions corresponding to the HOMO (blue: figure 4.10) show orbitals of π character delocalised over much of the chromophore, with no charge distribution residing on the semiconductor. Contrast can be seen in the dye LUMO orbitals (red: figure 4.10), with a large contribution from the substrate. We note that the dye LUMO orbitals located on the chromophores are of π^* character and reside

heavily on the thiophene bridge, cyano acceptor and anchor. Illustration of this point may also be seen from the projected density of states on the dye in the conduction band, figures 4.5 4.6. Indeed, for the chromphores with a di-thiophene linker the dye-LUMO contribution from the chromophore resides exclusively on the bridge, acceptor and anchor. Design of these dyes for excellent charge separation properties are proven successful by our results; A $\pi \rightarrow \pi^*$ HOMO to dye-LUMO transition into orbitals located on the π-A group providing a strong orbital interaction with the Ti 3*d* orbitals, which is known to be favourable for efficient charge transfer.

4.4 Chapter Summary

DFT calculations of the thiophene conjugated chromophores C2-1, C2-2, JK-24 and JK-25 adsorbed on the anatase (101) surface have been presented. A systematic investigation into the effect of conjugation extension and increased dye coverage has been carried out.

Surface coverage concentration has been found to have a more pronounced effect on electronic structure and adsorption properties than the effect of increasing thiophene conjugation. Large negative energy shifts of the introduced band gap states occur as a result of increased dye coverage, which would effectively reduce the IPCE of DSSCs. These shifts are shown to result from dipole-dipole interactions within the dye monolayer, and not from dye-TiO_2 interactions.

Thiophene conjugation length is shown to have a significant effect on electronic structure. Increased conjugation positively shift gap states, which can result in an introduction of extra occupied orbitals in the gap. Extra band gap states explain the broadening of the IPCE spectra due to this increased conjugation. Our results have shown the effectiveness of thiophene linker moieties for controlling charge separation within D-π-A structures bound to the TiO_2 surface. Also the extension of the conjugated thiophene chain for C2-2 from C2-1 produces a greater tendency for ordering into aggregates on the surface. Hindering of this attribute by the non-planar dimethylfluorene moiety for the JK-24 and JK-25 dyes is proven effective.

Chapter 5

Modifying TiO_2: Aluminium Doping

5.1 Introduction

So far we have examined the binding of anchors to TiO_2, and the effect modifications in dye design can on interactions with itself and TiO_2. Here we take a closer look at another approach for improving DSSC performance, namely the modification of the TiO_2 electrode through the introduction of dopants.

Cystal defects can have a significant role in defining the properties of TiO_2, and therefore the electrodes used in DSSCs. Actively doping TiO_2 with nitrogen, for example, is known to lower the photo-excitation threshold in anatase TiO_2 [156, 157], an extrinsic defect which has been put to use in photo-catalysis[158]. Aluminium dopants can be introduced in TiO_2 by inclusion of aluminium butoxide during the hydrolysis of titanium iso-propoxide (TTIP) [49]. DSSC electrodes including aluminium dopants produced in this manner have been shown to reduce the number of Ti^{3+} defects, improve the open circuit voltage (V_{OC}) and thereby the DSSC efficiency [49], however the mechanism has not been fully understood.

Intrinsic defects, such as oxygen vacancies, also have a important role in the chemical reactivity of TiO_2 surfaces. Examples include dissociation of water at vacancy sites on rutile (110) [159] and vacancies, along with other intrinsic defects, accounting for the island growth mode in the atomic layer deposition of Al_2O_3 on anatase (101) [160].

Oxygen vacancies introduce band-gap states in TiO_2 localised on Ti^{3+} ions [161, 162] which can trap injected electrons, and act as recombination centres [163]. Oxygen plasma

treatments of TiO_2 electrodes, which reduce the number of oxygen vacancies, have shown a marked increase in the short-circuit current of DSSCs [50], which indeed suggests that vacancies have a negative effect on DSSC performance. An increase in recombination sites in a DSSC will lead to interception of injected electrons by either the redox couple in solution, or by back transfer to dyes. Similarly this increase in recombination can cause a down shift in the quasi-Fermi energy of electrons in the conduction band, and a subsequent reduction in the short circuit voltage V_{OC}.

Previous theoretical studies carried out on aluminium doped TiO_2 have examined the stability of bulk defects in both rutile and anatase[164, 165, 166]. In the case of anatase, clustering of defects in which two Al dopants combined with oxygen vacancies was found to produce the most stable defect type [165, 166]. However the migration of aluminium interstitials throughout the bulk anatase crystal was found impossible at industrial temperatures, due to large transition barriers [165].

Oxygen vacancies are known to preferentially occupy sub-surface sites in anatase (101) [167, 168, 169]. It has been shown that oxygen vacancies in the (101) surface have diffusion barriers that can be overcome at typical annealing temperature, and surface vacancies migrate to and from the bulk at temperature $\geq$ 200K [169]. Diffusion of these oxygen vacancies suggests another mechanism by which stable clustering of intrinsic and extrinsic defects may occur in aluminium doped TiO_2.

The object of this chapter is to examine the effect of aluminium doping on the majority anatase (101) surface[170], and to understand the observed increase in DSSC efficiency which results. To this end density functional theory (DFT) calculations have been carried out to characterise the doped (101) surface, with a particular focus on the interplay between intrinsic oxygen vacancy defects and the extrinsic aluminium dopants. Defect stabilities have been calculated for aluminium defects with and without the presence of oxygen vacancies.

Exchange and correlation effects have been approximated by the generalised gradient approxiamtion of Perdew and Wang [171]. Semi-local functionals such as PW91 are known to incorrectly describe the Ti^{3+} states resulting from an oxygen vacancy in TiO_2, due largely to self-interaction errors and the band gap underestimation[172]. A similar failure has been reported in the case of single aluminium dopants for TiO_2 in the Rutile phase[164]. Therefore in the case of single Al substitutional defects and isolated oxygen vacancies, as a step to rectify the limitations of GGA, we have also performed GGA corrected for on-site Coulomb interactions (GGA+U) [173, 174].

Nudged elastic band (NEB) calculations have also been performed to establish diffusion

	Expt. [177] (Å)	Ref (US PP's) Chapter [178] (Å)	This Work (Å)
Lattice Parameters			
a	3.782	3.817 (+0.9%)	3.804 (+ 0.6%)
c	9.502	9.710 (+2.2%)	9.698 (+ 2.1%)
Bond Lengths			
Equatorial	1.932	1.954 (+1.1%)	1.947 (+ 0.8%)
Apical	1.979	2.011 (+1.6%)	2.005 (+ 1.3%)

Table 5.1: Calculated and experimental lattice parameters and bond lengths of bulk anatase TiO_2

barriers for oxygen vacancies in the presence of aluminium dopants, and illustrate the possibility of the intrinsic extrinsic defect clustering. Finally the effect of these defects on the adsorption of a typical DSSC dye is examined.

5.2 Computational Detail

All calculations have been performed using the plane wave DFT code VASP [175]. As mentioned, exchange and correlation effects were approximated with the GGA-PW91 functional [171] with core electron wavefunctions treated within the projector augmented wave method [176], with the same electrons treated as valence and core as in previous chapters. For both bulk and surface calculations a plane wave cut-off of 800 eV has been used, giving total energies converged to within 0.06 eV of values at 700 eV.

Calculated lattice parameters for the bulk anatase TiO_2 without defects can be seen in figure 5.1. Good agreement with experimental data and the results from the previous chapter can be seen, and we have used these bulk lattice parameters throughout the current investigation. Periodic images of the defects will interact with one another, and in order to gauge the extent of this interaction in the bulk case we have taken one defect type (A2; see figure 5.2) and performed calculations for varying supercell dimensions. Supercells containing one defect with sizes of 2, 3, 4 and 5 unit cells have been examined. Supercell extension was along one minor lattice vector (a=3.804 Å) while the other two vectors were kept constant. A Monkhorst-Pack k-point mesh has been utilised throughout these calculations with dimensions of $6 \times 6 \times 3$ for the smallest supercell, varying to $3 \times 6 \times 3$ for the largest supercell. Following this test

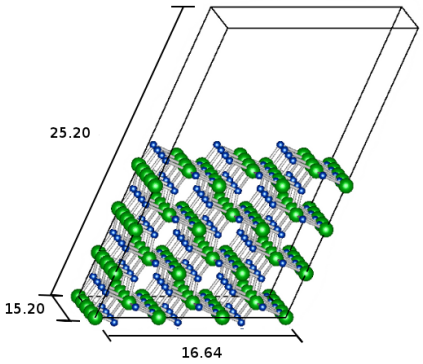

Figure 5.1: Anatase (101) surface: 4 layer slab used in defect calculations. Titanium atoms are represented in green, oxygen atoms in blue. The bounding box shows the unit cell with the cell dimensions in Å.

bulk defect calculations have been performed in a $3 \times 4 \times 1$ supercell, with a k-point mesh of $3 \times 2 \times 3$. Relaxations were performed using the conjugate gradients method, and considered finished when forces on ions were less than 0.03 eV/Å.

For surface calculations a four layer triclinic unit cell containing 288 atoms, with cell dimensions illustrated in figure 5.1, was the clean starting point. In order to prevent spurious interactions between periodic slabs it was ensured that a vacuum layer of at least 10 Å separated images in the (101) direction for all calculations. A Monkhorst-pack grid of $2\times2\times1$ was utilised throughout surface calculations, and increased to $4 \times 4 \times 1$ for density of states calculations. Fixing the bottom layer to the relaxed bulk position, geometry relaxations were again performed with the conjugate gradient method until ionic forces were less than 0.03 eV/Å. Calculations on chromophore adsorption were performed following previous work [178], and considered fully relaxed when forces on ions were less than 0.03 eV/Å. In the calculation of defect stability isolated molecule calculations have been performed, and in each case the calculation parameters are the same as the substrate to which they will be compared.

Results reported for the A2 and A3 defects have been obtained with spin unpolarised calculations, and compared to spin polarised tests with no difference found. In the case of the A1 defect, the single substitution of an Al dopant leaves one unpaired electron, so spin polarised calculations are performed throughout for both GGA and GGA+*U*. Similarly spin polarised calculations are performed in all cases in which an isolated oxygen vacancy is present.

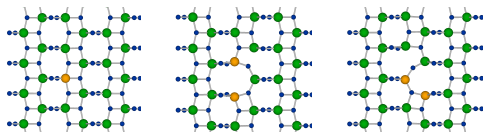

Figure 5.2: Aluminium doped anatase defect structues. Titanium atoms are represented in green, oxygen in blue, aluminium in orange. For clarity the defects are shown in a single (101) layer.

As mentioned we have performed calculations in which the GGA functional has been corrected for on-site Coulomb interactions (GGA+U) [173, 174]. Density functional theory, as we have seen in chapter 2, includes a self interaction error as a result of our mean-field treatment of the Coulomb potential. Exact exchange in Hartree-Fock cancels this effect, but this is not the case in DFT. The result is that the tendency of electrons to unphysically delocalise is increased. DFT+U attemps to correct this tendency by correcting the electronic correlations through the addition of an energy penalty (and a double counting term). We have employed the DFT+U correction in the form of Dudarev[173] in the case of the A1 defects and for the oxygen vacancy calculations. In the case of the oxygen vacancy U with a value of 3eV has been applied to the Ti3d orbitals, which has been shown to qualitatively agree with the B3LYP hybrid functional in the case of oxygen vacancies in Anatase TiO_2[179]. A range of values of U are applied to the O2p states in the case of a single Al^{3+} for Ti^{4+} substitution in the bulk, with a value of 6eV used for surface calculations.

5.3 Bulk TiO_2 Defects

Previous studies have suggested that interstitial defects are relatively less stable than substitutional doping [165], so here we focus only on these substitutional defect types. Three different defects are considered (illustrated in figure 5.2); direct substitution of a titanium atom for an aluminium atom (A1) and two substitutional defects combined with an oxygen vacancy (A2 & A3).

Aluminium dopants may also be introduced in TiO_2 during the combustion of $TiCl_4$ by inclusion of $AlCl_3$. As in the work of Shirley et al [165], we use as a measure of defect stability the energy of reaction for the following equivalent reaction:

$$(x+z)\,\mathrm{TiO_2} + z\mathrm{AlCl_3} + \frac{z}{2}\mathrm{Cl_2} \rightleftharpoons \mathrm{Ti}_x\mathrm{O}_y\mathrm{Al}_z + z\mathrm{TiCl_4} + \left(x+z-\frac{y}{2}\right)\mathrm{O_2} \tag{5.1}$$

such that

$$\begin{aligned}\Delta \mathrm{E}_{0K} =& \mathrm{E}_b\left(\mathrm{Ti}_x\mathrm{O}_y\mathrm{Al}_z\right) + \mathrm{E}_b\left(z\mathrm{TiCl_4}\right) \\ &+ \mathrm{E}_b\left(\left(x+z-\frac{y}{2}\right)\mathrm{O_2}\right) - \mathrm{E}_b\left(\frac{z}{2}\mathrm{Cl_2}\right) \\ &- \mathrm{E}_b((x+z)\,\mathrm{TiO_2}) - \mathrm{E}_b\left(z\mathrm{AlCl_3}\right)\end{aligned} \tag{5.2}$$

where $\Delta \mathrm{E}_{0K}$ is the energy of reaction at 0K, and $\mathrm{E_b}$ is binding energy as given by our DFT calculations. Zero point energies have been neglected.

As a first step we perform calculations on the A2 defect in order to evaluate the typical defect-defect interaction. Calculated bulk energies of reaction for the A2 defects in varying supercell sizes are exhibited in table 5.2. Reaction energies suggest that defect-defect interaction is fairly short ranged, with energies at a defect separation along the varying vector of around 7Å converged to within 0.02 eV of that at a distance of around 14Å. In order to minimize the defect-defect interaction bulk calculations proceed with supercells of dimenisons $3 \times 4 \times 1$ unit cells, containing 144 atoms in the clean supercell, giving a defect separation of greater than 7.5Å in all directions. Experimentally the atomic decomposition of the doped powder made up of 3.3% aluminium[49], while cell dimensions $4 \times 3 \times 1$ give us 1.4% for A2 & A3 defects.

Substitution of an Al^{3+} ion for a Ti^{4+} ion will result in one less electron in the system, and an oxygen hole being formed. Polaronic in nature, this resulting O^- state is poorly described by GGA and we have examined the defect stability and hole characteristics with varying values of on-site Coulomb interaction (U) figure 5.3.

Defect formation energy and O^- hole position can be seen to have a significant dependence on the value of the applied U correction (no value is reported for U=1eV as convergence was not reached). Reaction energies vary over a wide range of around 1 eV. Similar ranges for reactions involving TiO_2 on varying U have been reported elsewhere [180]. The nature of the GGA+U method is to empirically tune the value of U such that some property of interest belonging the system matches with experiment. Experimental data for the defect stability reaction is not available, so instead we tune the value of U such that the O^- polaron is well localised. In the case of pure GGA the hole is found to be delocalised throughout the system,

Defect Type	A2 (eV)
Supercell Dimension	
$2 \times 2 \times 1$	-0.051
$3 \times 2 \times 1$	-0.280
$4 \times 2 \times 1$	-0.342
$5 \times 2 \times 1$	-0.368

Table 5.2: Calculated ΔE_{0K} for bulk aluminium defect typei A2 with varying supercell size. Dimensions are given as multiples of unit cell vectors along the two minor and one major axis respectively.

and becomes increasingly more localised on an oxygen atom neighbouring the aluminium dopant as the value of *U* is increased. We find that a *U* value of 6eV provides a well localised hole, which can be seen in figure 5.4, and is close to the value of 7eV used to describe the polaronic hole in rutile [164].

Selected bond lengths in the vicinity of the aluminium dopant can be seen in the case of pure GGA and GGA+*U* (*U*=6eV). In the case of the pure GGA calculation, variations in the bond lengths surrounding the dopant are found to be symmetric. Application of the onsite Coloumb correcton results in an asymmetric defect. Bond lengths involving an equatorially bonded oxygen atom adjacent to the dopant are extended, with this extension indicative of the associated O^- polaron.

Energetically, as this hole becomes more localised with increased values of *U*, its position is shifted further from the valence band in the band gap. Partial density of states for the pure GGA defect and the GGA+*U* (*U*= 6eV) can be seen in figure 5.4(c). For uncorrected GGA the defect is unpolarised with the oxygen hole located at the top of the valence band, consistent with results reported by Shirley et al [165]. For the GGA+*U* solution the defect is polarised, with the localised hole in the band gap.

Calculated bulk energies of reaction for the A2 and A3 defects, and the comparative result for the A1 defect, are exhibited in table 5.3. Given the wide variation of calculated reaction energies for the A1 defect formation with the value of the applied onsite Coloumb correction, we have also calculated the reaction energies for the A2 and A3 defects with an applied correction in order to make a direct comparison of the stability.

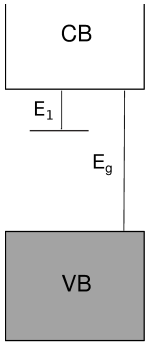

U(eV)	E_1	E_g (eV)	ΔE_{0K}
0	2.17	2.17	0.293
1	N/A	N/A	N/A
2	1.78	2.17	0.232
3	1.50	2.19	0.093
4	1.21	2.21	-0.076
5	0.92	2.23	-0.266
6	0.64	2.25	-0.472
7	0.39	2.26	-0.689

Figure 5.3: **A1 Bulk Defect:** U dependence on band gap (E_g), oxygen hole state (E_1) and defect formation energy (ΔE_{0K}).

Defect Type	GGA (eV)	GGA+U (U = 6eV)
A1	0.293	-0.472
A2	-0.388	-0.710
A3	-0.317	-0.629

Table 5.3: Calculated ΔE_{0K} for bulk aluminium defect types with and without applied U correction.

GGA predicts defect types comprising two aluminium substitutions with an oxygen vacancy, types A2 & A3, to be exothermic with the most stable defect type being A2. Single substitutional defect A1 is found to be endothermic by GGA. These results are in good agreement with previous work using the PBE functional, with ultrasoft pseudopotentials [165]. Substitution of an Al^{3+} for one Ti^{4+} results in one less electron in the system, and a O^{-} state is formed rather than O^{2-}. Combining two of these substitutions with an oxygen vacancy results in formal charge being maintained, resulting in the stability of defect types A2 & A3. While we can put less faith in the absolute values of the GGA+U results, given the empirical nature of the method and the lack of experimental data, the same trend is still exhibited with the clustered A2 and A3 defect types being more stable than a single Al^{3+} for Ti^{4+} substitution.

	Bond (Å)									
	Al-O1	Al-O2	Al-O3	Al-O4	Al-O5	Al-O7	O5-Ti2	O5-Ti3	O7-Ti4	O7-Ti5
Method										
GGA	1.91	1.90	1.93	1.93	1.91	1.91	2.04	1.88	2.02	1.89
GGA+U(6 eV.)	1.90	1.85	1.93	1.91	**1.95**	1.90	**2.29**	**2.07**	2.01	1.90

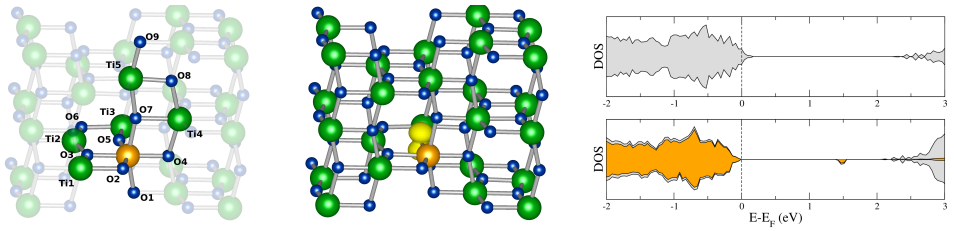

(a) **(b)** **(c)**

Figure 5.4: **A1 Bulk Defect: Top** Selected bond lengths for the A1 defect. Largest bond lengths resulting from a localised polaron are in bold. **Bottom (a)** Atom labels used in table above. **(b)** GGA+U(6eV) defect state with localised hole. Titanium atoms are represented in green, oxygen atoms in blue, aluminium in orange and spin difference isosurface in yellow (0.04 ev/Å). **(c)** Projected density of states for A1 defect. Top: GGA, Bottom: GGA+U (U=6eV). Total DOS in grey and for GGA+U calculations the oxygen 2p states are represented in orange.

5.4 (101) Surface

In the case of the (101) surface numerous inequivalent positions are available for defects. The clean stoichiometric surface contains both five-fold and six-fold co-ordinated titanium atoms, each of which may be substituted for an Al atom. Energies of reaction for A2 and A3 defects in which substitutions occurred in different (101) layers were consistently found to be less stable than those containing two Al atoms in the same layer and therefore we only report the latter results. Differing defect positions for A2 defects can be seen in figure 5.5. For the A1 defect position the same notation applies, for example D1 corresponds to a single substitution of a five-fold co-ordinated Ti atom and D1.2 corresponds to substitution of a six-fold co-ordinated Ti in the upper layer. A3 defects necessarily contain Al substitutions at differing positions along the [101] direction, which in the case of the uppermost layer means substitution of one

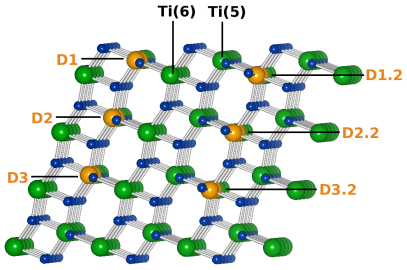

Figure 5.5: Notation for surface defect positions relative to the 101 surface. Titanium atoms are represented in green, oxygen atoms in blue and aluminium in orange. Ti(5) labels five-fold co-ordinated titanium atoms, Ti(6) six-fold coordinated.

five-fold co-ordinated and one six-fold co-ordinated Ti. The differing notation therefore refers to the position of the vacancy, with D1 refering to the defect in the uppermost layer with the vacancy slightly further along the [101] direction than D1.2.

Calculated reaction energies for defects at each of these positions are shown in figure 5.4. It is known that oxygen vacancies on anatase (101) surfaces reside preferentially at sub-surface sites [167, 168]. Sub-surface sites are here also found to be preferential for the aluminium defects, with the D2 position being the most stable for each type (the same was found in tests with 5 layer slabs). Large differences in stability can be seen between surface and subsurface sites, with a significant energetic bias towards the sub-surface positions for all defects. This is parallel to experimental evidence suggesting that Aluminium defects tend to reside in subsurface sites in the rutile TiO_2 polymorph [181, 182]. Least stable defects energies are present when aluminium atoms are substituted for 6-fold co-ordinated Ti atoms in the surface and reside next to two-fold cordinated oxygen atoms (O(2)) in the surface i.e. position D1.2. Despite residing next to an O(2) atom the A1 and A2 defects at position D1 is relatively more stable than its D1.2 counterpart as the Al atoms bonding to the O(2) atoms are themselves under co-ordinated as a result of being at the surface.

Given the empirical nature of the GGA+U reaction energies, the A1 GGA+U results are given relative to the bulk case in order to focus on the general trend rather than absolute values. Similar energetic bias towards the subsurface D2 is exhibited, with the D1.2 position the least stable. GGA+U results for the A1 defect suggest that if the defect resides close enough to an under co-ordinated surface O(2) atom the O^- hole will localise on it. Defect positions D1, D1.2 and D2 all result with a surface localised hole state figure 5.7. Indeed in the case of the D3.2 defect the hole localises on an O(2) atom in the bottom layer of the surface which, given

Defect Type	A1		A2	A3
	GGA	GGA+U		
	(eV)	(eV)	(eV)	(eV)
Position				
D1	0.197	-0.056	-0.128	0.274
D1.2	0.454	0.333	0.625	0.331
D2	**-0.122**	**-0.225**	**-0.568**	**-0.337**
D2.2	0.043	0.094	-0.175	-0.299
D3	-0.050	0.164	-0.400	-0.299
D3.2	-0.020	0.328	-0.307	-0.301

Table 5.4: Calculated ΔE_{0K} for differing positions in a 4 layer (101) slab. Most stable defect positions for each type are highlighted in bold. A1 GGA+*U* reaction energies are given relative to the bulk defect formation energy.

that the bottom layer of the slab is fixed to the bulk position, explains the increase in the D3.2 defect formation energy relative to the bulk. GGA predicts no variation in position relative to the valence band of the hole state, while for the GGA+*U* calculations a large energetic variation is observed with differing location in the surface figure 5.7. At the surface the hole is further from the valence band, converging towards the bulk value as it moves further into the slab, as can be seen for two examples in figure 5.6 (D3.2 being the exception again, due to the localisation of the hole on a fixed atom).

As in the bulk case, the most stable defect is found to be that of type A2 and its formation is energetically favourable when at the D2 sub-surface position. An important difference to note is that GGA predicts that when A1 defects reside at subsurface sites the defect formation becomes exothermic and energetically favourable, unlike the bulk which is endothemric. Differences between all three defect stabilities are not so large and in reality all three defect types will co-exist.

5.4.1 Oxygen Vacancy

We have seen that introduction of an Al dopant produces hole states in the band gap. Intrinsic oxygen vacancies have the opposite effect, introducing occupied states within the band gap. In the case of GGA these states are delocalised throughout the lattice, and unpolarised with the introduced states both at the bottom of the conduction band. Application of DFT+U produces

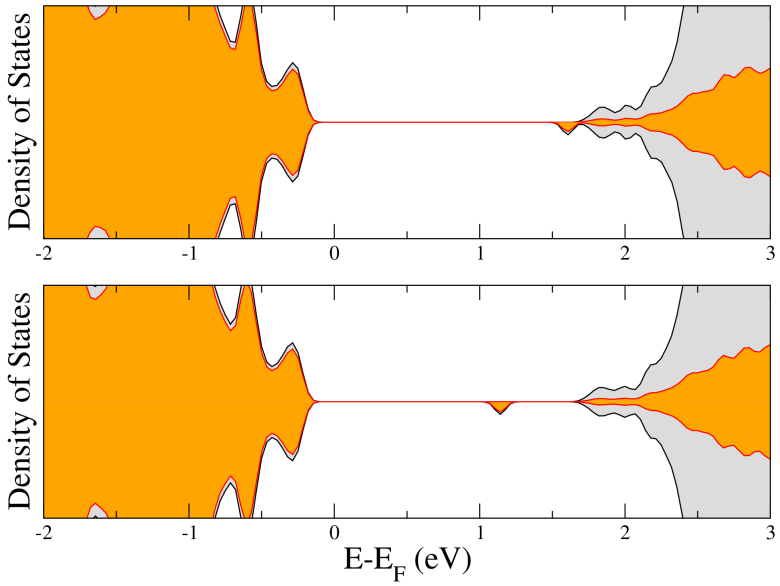

Figure 5.6: Partial density of states for single Al dopants in the (101) surface. Top: A1 defect in D1 surface position. Bottom: A1 defect in D2.2 position. Projection on the oxygen atoms is in orange, total DOS in grey.

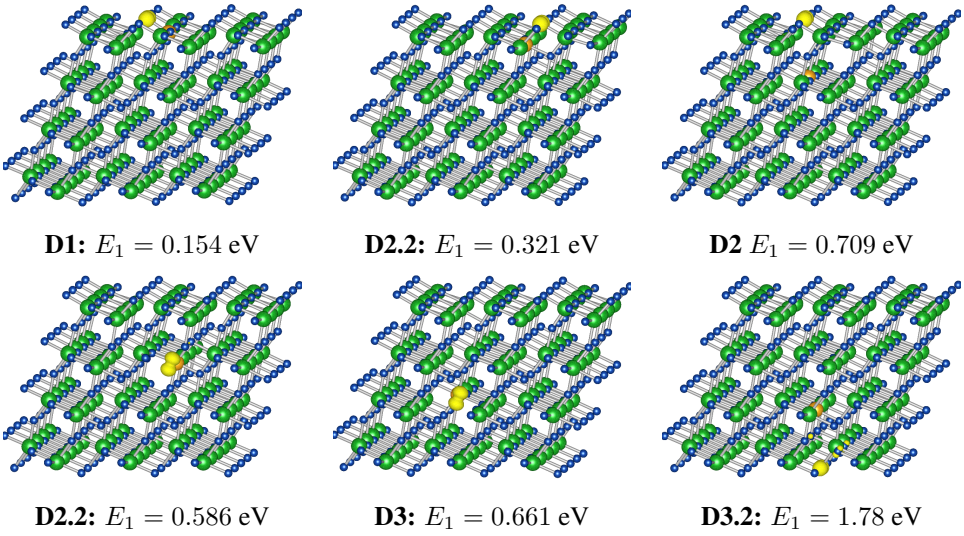

Figure 5.7: **A1 Surface Defect:** GGA+*U* spin difference isosurface (yellow, 0.02 (0.04 ev/Å)) for the A1 single substitutional defect at varying positions in the (101) surface. Associated hole position relative to the conduction band is also given.

a localised vacancy state on a neighbouring Ti atom, giving us a Ti^{3+} ion, and a second delocalised throughout the lattice (spin difference isodensity plot may be seen in figure 5.8). We can see from the partial density of states that both states lie relatively close to the conduction band edge, with the localised state further into the band gap. This is similar to the situation reported for oxygen vacancies in bulk anatase treated with GGA+U [172]

5.5 Vacancy Diffusion

In order for the A2 and A3 defect formation to occur the substitutional defect type A1 must have some mechanism of combining with oxygen vacancies. However previous work has suggested that the movement of aluminium interstitials throughout the anatase lattice is not energetically feasible [165]. Here we propose the diffusion of oxygen vacancies throughout the lattice as a mechanism by which A1 and oxygen vacancies combine to result in A2 and A3 defects.

In order to investigate this possibility we have performed climbing image nudged elastic band (NEB) calculations[183] to examine the energy profile along oxygen vacancy diffusion paths which would result in the formation of A2 and A3 defects. For these calculations the computational expense has been eased by reducing the number of anatase layers in the slab

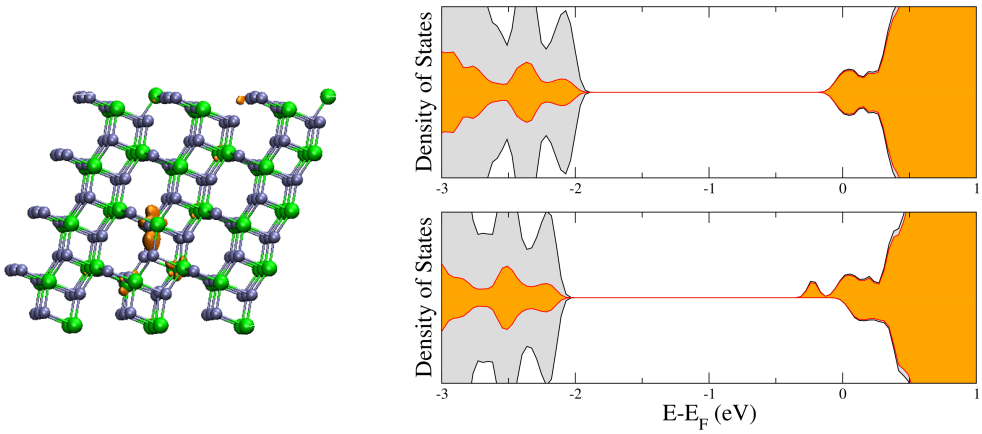

Figure 5.8: **(i)** Spin isosurface for oxygen vacancy state in the (101) surface and **(ii)**partial density of states for GGA(top) and GGA+U(U=3eV)(bottom)

to three (sub-surface defects in position D2, i.e. those in the second layer from the surface, remain the most energetically favoured in the three layer slab).

The preference of both oxygen vacancies and A1 aluminium defects to reside in the sub-surface anatase (101) region increases the likelihood of a) two A1 defects occupying adjacent sites and b) oxygen vacancies residing close to A1 defects. Due to this preference of the A1 and oxygen vacancies to occupy subsurface sites we have examined only the diffusion of a single subsurface oxygen vacancy towards two adjacent subsurface A1 defects. Diffusion of oxygen vacancies is therefore assumed to proceed parallel to the (101) surface. Obviously this scenario is not exhaustive of the possible ways in which the defect types can combine, rather it is taken as a likely possibility to gauge the typical energetic barrier for such combination processes.

Potential energy surfaces and vacancy diffusion pathways for the formation of A2 and A3 defects can be seen in figure 5.9 and figure 5.10. Small diffusion barriers of around 0.15 eV and 0.1 eV are found for the A2 and A3 defects respectively. Energetic gains on overcoming these barriers of around 0.25 eV and 0.13 eV for A2 and A3 defects illustrate a bias towards the formation of these defects. Oxygen vacancy diffusion therefore provides a mechanism by which the aluminium dopants combine with oxygen vacancies in their proximity. This result explains the experimentally observed reduction in Ti^{3+} defects on doping of TiO_2 with aluminium [49]. Again it is important to stress that we are not suggesting that these

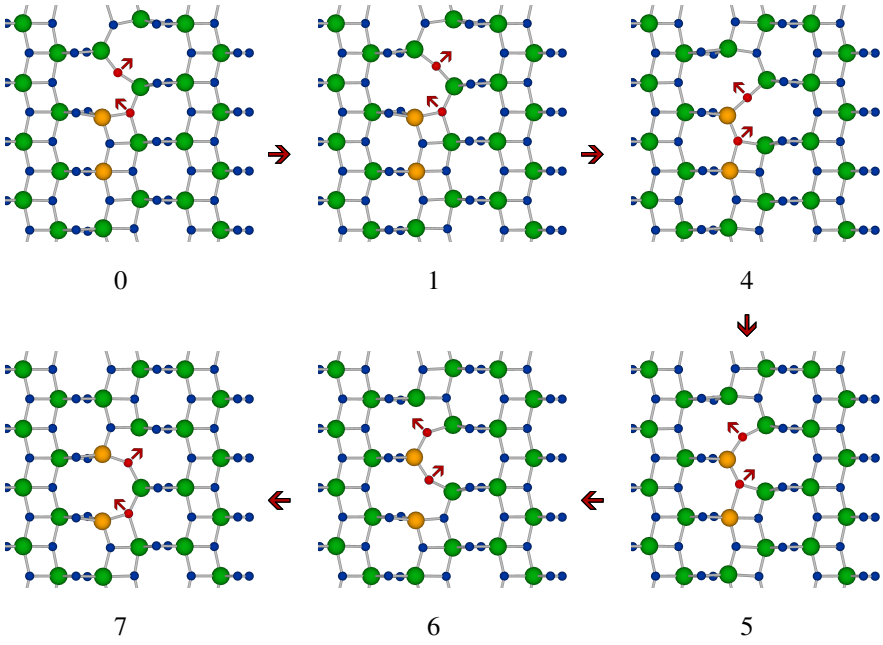

(i)

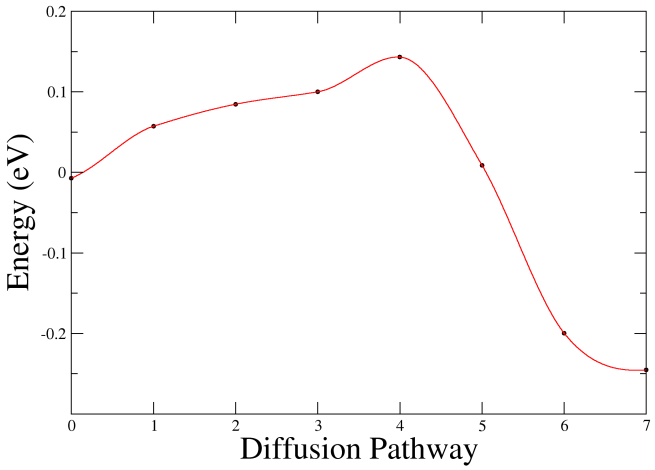

(ii)

Figure 5.9: **(i)** Diffusion pathway for an oxygen vacancy towards Aluminium dopants resulting in a defect of A2 type. For clarity only the central layer is illustrated. **(ii)** Potential energy pathway along the shown diffusion pathway, with a spline fitted to the data to serve as a guide to the eye.

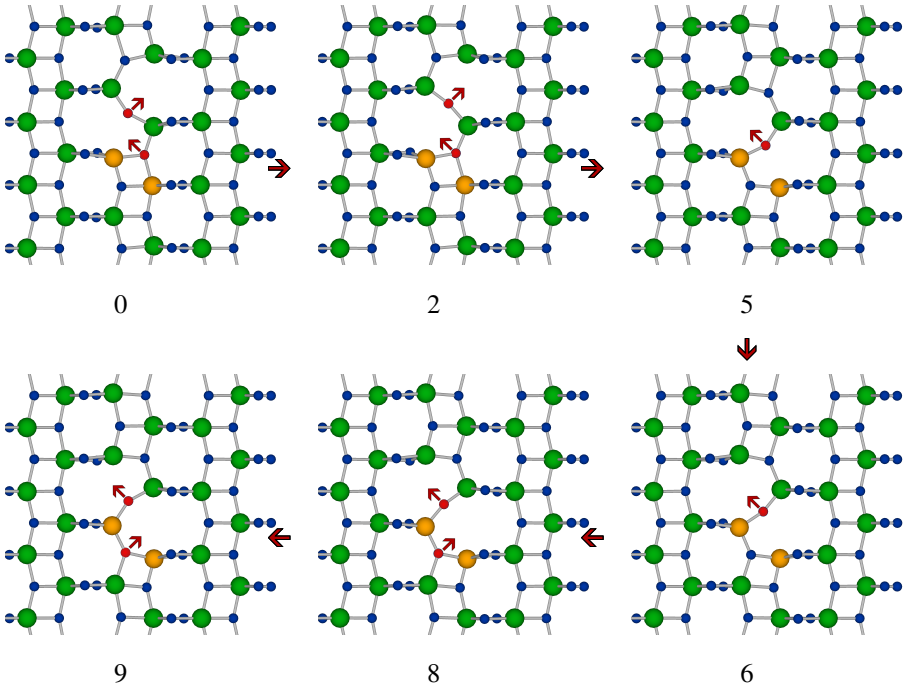

(i)

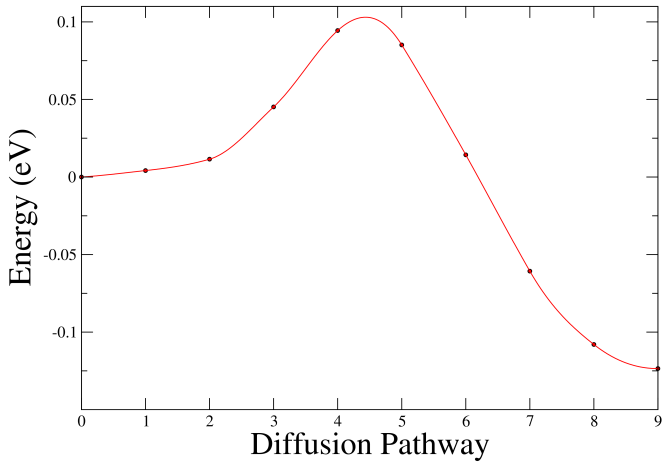

(ii)

Figure 5.10: **(a)** Diffusion pathway for oxygen vacancy towards Aluminium dopants resulting in a defect of A3 type. For clarity only the central layer is illustrated. **(b)** Potential energy pathway along the shown diffusion pathway, with a spline fitted to the data to serve as a guide to the eye.

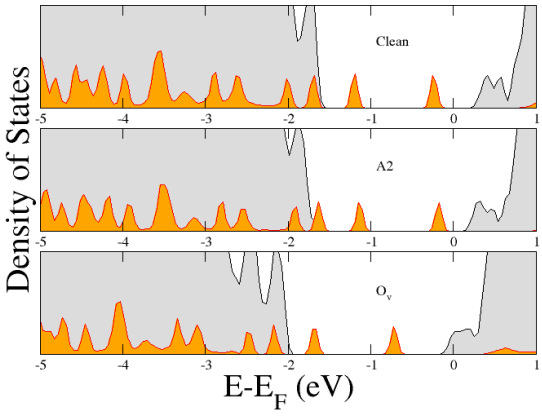

Figure 5.11: Partial density of states. Top: C2-1 adsorbed on clean anatase (101). Middle: C2-1 adsorbed on anatase (101) containing an A2 subsurface defect. Bottom: C2-1 adsorbed on anatase (101) containing an oxygen vacancy. The projection on the chromophore is in orange, total DOS in grey.

diffusion processes are the only mechanism by which intrinsic and extrinsic defects are likely to interact. Given an experimental atomic decomposition of 3.3% aluminium in the doped TiO_2 powders, coupled with the preference of oxygen vacancies and Al dopants to reside in subsurface positions, it is one likely mechanism.

5.6 Electronic Structure & Chromophore Adsorption

Adsorption of a chromophore to TiO_2 electrodes is one of the fundamental interactions in a dye sensitised solar cell. To understand the impact of aluminium doping on this interaction calculations on a composite system in which a chromophore is adsorbed onto both clean and defective surfaces have been performed. For this purpose we have chosen the C2-1 tetrahydroquinoline chromophore which has shown to successfully sensitise TiO_2 in DSSCs [184], and was studied in the previous chapter. From our previous work we know the chromophore preferentially binds to the clean anatase (101) surface via a dissociative bidentate bridging mechanism [178] and it is this adsorption mode that is used throughout. The C2-1 dye has been adsorbed on surfaces containing A2, A3 and oxygen vacancy defects in sub-surface positions, and for each of these adsorption modes we have used the same computational procedure

as the previous chapter, to allow direct comparisons. Adsorption energies are calculated by the subtraction of the energy of the defective slab and the isolated C2-1 chromophore from that of the total system and are shown in figure 5.5. Adsorption on the slab containing a sub-surface oxygen vacancy increases the adsorption energy significantly with respect to the clean surface, whereas the adsorption on slabs containing the aluminium defects vary only slightly with respect to the clean surface. Experimentally it has been reported that aluminium doped TiO_2 binds chromophores more strongly to the surface, due to a preference for dye molecules to attach to stable Ti^{4+} atoms rather than Ti^{3+} [49]. Our result that the C2-1 adsorption energy increases on the preferential subsurface oxygen vacancy compared to the Al defects suggests that this result is due to observed morphology changes resulting from the doping, not as a result of a decrease in Ti^{3+} concentration.

As we have already seen that in the A1 substitutional defect an Al^{3+} ion replacing a Ti^{4+} ion results in a valence band hole, while an oxygen vacancy introduces occupied Ti^{3+} states into the band-gap. The combination of two substitutional aluminium atoms with an oxygen vacancy (A2 & A3) causes the formal charge to be maintained, with the two electrons from the oxygen vacancy filling the valence band holes resulting from Al^{3+} substitutions. Oxygen vacancy states are not present and the substitutional valence band holes disappear, with the result that the doped A2 and A3 anatase surfaces behave as if they were clean. We can see this result on examining the density of states for the C2-1 adsorbed on the A2 defect and on the clean surface, figure 5.11, with little difference between the electronic structure for C2-1 adsorbed on the clean surface and that of the C2-1 adsorbed on the A2 (a similar result is found for the A3 defect).

Adsorption above the oxygen vacancy results in electronic structure that retains the occupied defect state at the bottom of the conduction band. Interestingly the oxygen vacancy also down shifts the dye localised HOMO relative to the conduction band, while the A2 defect slightly shifts these dye localised states closer to the conduction band. We have also performed adsorption calculations on the oxygen vacancy with GGA+U (again using the PAW approach) and found a similar result, as can be seen in figure 5.12, with the oxygen vacancy defect states being retained just below the conduction band and a down-shift of the dye HOMO level within the band gap. As well as providing the reported recombination Ti^{3+} centres this shifting of the HOMO level by the introduction of of an oxygen vacancy could have consequences for DSSC efficiency, potentially compounding the effect of recombination by adding to the reduction in J_{SC} and V_{OC}.

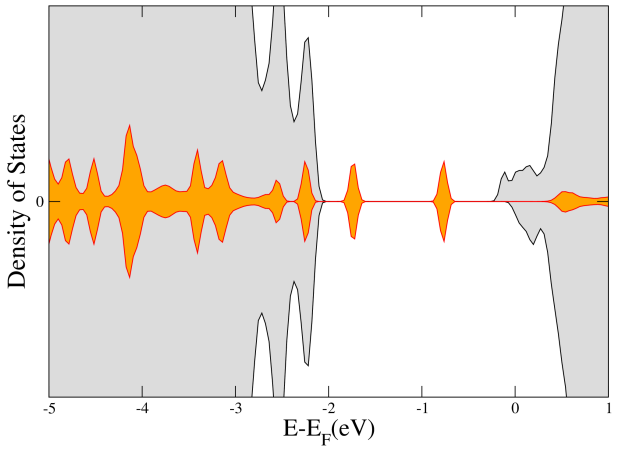

Figure 5.12: GGA+U partial density of states for C2-1 adsorbed above an oxygen vacancy. The projection on the chromophore is in orange, total DOS in grey.

Defect type	Adsorption energy (eV)
Clean [178]	-1.14
O_V	-1.55
A2	-1.20
A3	-1.12

Table 5.5: Calculated adsorption energies for the C2-1 chromophore on the anatase (101) surface.

5.7 Chapter Summary

DFT and DFT+U calculations on the Al^{3+} doping of anatase TiO_2 have been performed, with both the bulk and (101) surface examined. Single substitutions of Al^{3+} with Ti^{4+} (defect A1) and clustering of two of these extrinsic Al^{3+} dopants with an intrinsic oxygen vacancy have been investigated (defect type A2 and A3). Defect types A1 were found to be endothermic in the bulk, and exothermic at sub-surface sites on the (101) surface. A2 and A3 were found to be exothermic in the bulk and also preferentially occupy sub-surface sites on the (101) surface.

Nudged elastic band calculations have illustrated that combination of an intrinsic vacancy and extrinsic Al^{3+} dopants to form stable defects is possible and likely through oxygen vacancy diffusion. Low energy barriers for this diffusion process with an energetic bias towards the formation of A2 and A3 defects have been found, and vacancy diffusion has been concluded to be a viable route to these clustered defects.

Susbstitution of Ti^{4+} with $A1^{3+}$ results in a valence band hole. Combining two of these substitutions with an O vacancy result in the formally neutral defects, A2 and A3, in which the typical oxygen vacancy Ti^{3+} states are not present and the valence band hole disappears. This 'cleaning up' of the oxygen vacancies in the TiO_2 subsurface by benign aluminium doping results in a reduction in Ti^{3+} states and explains the observed increase in DSSC efficiency obtained as a result. Recombination at these Ti^{3+} sites effectively leads to a reduced J_{SC}, the open circuit voltage can also be reduced as a result of a down shift in the quasi-Fermi energy. We also found a down shift in the dye localised states in the band gap on introduction of an oxygen vacancy. Removing these defects can improve both J_{SC} and V_{OC}, and thereby improve efficiency.

Adsorption of a typical DSSC chromophore, the C2-1 tetraquinoline dye, on the defective surface has be investigated. Adsorption to the oxygen vacancy site is found to the most energetically favoured, with the adsorption on the A2 and A3 defects behaving much like adsorption on a clean surface. A down shift in the dye localised states in the band gap on introduction of an oxygen vacancy has been observed. Finally we conclude that the observed V_{OC} increase on aluminium doping of the TiO_2 electrodes in DSSCs is likely to be as a result the benign clean up of Ti^{3+} states by the trivalent aluminium dopants.

Chapter 6

RT-TDDFT in the CONQUEST Code

6.1 Introduction

Density functional theory (DFT) has become an almost ubiquitous tool in the arsenal of the electronic structure theorist[185, 186]. Extending DFT to the time domain results in its excited state counterpart, time dependent density functional theory (TDDFT)[187, 188].

Casida's linear response formulation of TDDFT [189, 190] requires the solution of an eigenvalue equation for a matrix Ω written in the space of electron-hole pairs. Ω is of order N^2 where N is the number of electronic transitions considered, and diagonalising Ω scales computationally as $\mathcal{O}(N^6)$. For small systems this approach is feasible computationally, and has been widely used [190], while for larger systems the unfavourable scaling renders it unsuitable.

Real time propagation of the time-dependent Kohn-Sham equations, pioneered by Yabana and Bertsch [191], provides an alternative approach to Casida's linear response formalism. Real time TDDFT (RT-TDDFT) proceeds by the construction of an effective Hamiltonian, followed by the direct propagation of the Kohn-Sham orbitals using this Hamiltonian. Assuming both the number of occupied states (N_{KS}) and the number of mesh points (N_M) scale linearly with system size, RT-TDDFT will scale with the number of atoms, N, as $N_{KS}N_M \sim N^2$. A significant prefactor in the form of the number of time steps and the computational effort for construction of the Hamiltonian exists, making this method unsuitable for systems of small size. However the $\mathcal{O}N^2$ scaling have made it the natural choice for tackling systems of large size, and a complementary partner to Casida's approach.

Linear scaling, or $\mathcal{O}$(N), density functional theory is now well established [192]. In a similar manner RT-TDDFT based on the propagation of the density matrix, as opposed to the Kohn-Sham orbitals, can be made to scale *linearly* with system size. Reductions in the computational expense obtained by working with the truncated density matrix open up the possibility of studying excited states in large systems that cannot feasibly be examined with other methods.

RT-TDDFT based on density matrix propagation has been used to study fullerene, sodium clusters, polyacetylene oligomers, carbon nanotubes and silicon clusters to name a few[193, 194, 195, 196, 197, 198, 199].

In this chapter we briefly introduce the idea behind linear scaling density functional theory (for a review see [200]), followed by a brief summary of our implementation of RT-TDDFT in the CONQUEST code. Tests are presented on a series of previously studied small molecules, in order to confirm the reliability and limitations of our implementation. We then examine the effect of matrix truncation and the scaling with system size for a series of long chain alkane molecules.

6.2 Computational Approach

6.2.1 Linear Scaling DFT

DFT calculations obtain the electronic ground state by self-consistent minimisation of an energy functional $E[n(r)]$ through variation of the electronic density n(**r**). In typical DFT approaches this electronic density is expressed in terms of the single particle Kohn-Sham orbitals as $n\left(\mathbf{r}\right) = \sum_i |\psi_i|^2$. Linear scaling DFT methods follow an equivalent approach but work instead with the density matrix, formally defined as:

$$\rho(\mathbf{r}, \mathbf{r'}) = \sum_i f_i \psi_i\left(\mathbf{r}\right) \psi_i\left(\mathbf{r'}\right)^* \tag{6.1}$$

DFT in the conventional approach involves the diagonalisation of the Hamiltonian. Linear scaling methods instead obtain the ground state by minimisation of the system energy through variations of $\rho(\mathbf{r}, \mathbf{r'})$.

Kohn's principle of nearsightedness[201] states that for well-gapped systems the density matrix approaches zero exponentially as the separation increases, $\rho(\mathbf{r}, \mathbf{r'}) \to 0$ as $|\mathbf{r} - \mathbf{r'}| \to \infty$. Using this principle allows a spatial cut-off radius to be imposed on the density matrix, such that

$$\rho(\mathbf{r}, \mathbf{r}') = 0 \qquad \text{for all} \qquad |\mathbf{r} - \mathbf{r}'| > R_c \tag{6.2}$$

This provides a variational upper bound to the total system energy, E_{tot}. Increasing the cut-off causes the value of E_{tot} to approach the true value.

Linear scaling behaviour can be obtained through this spatial cut-off by noting that the number of non-zero density matrix elements increases linearly with system size. Diagonalisation of the Hamiltonian in conventional DFT methods intrinsically scales as $\mathcal{O}(\mathrm{N}^3)$, providing a computational bottleneck which limits system size. $\mathcal{O}(\mathrm{N})$ methods do not suffer from the same bottleneck, allowing vastly larger systems to be studied. For example Conquest has been used to perform calculations on millions of atoms [192].

In practice Conquest uses the density matrix written in separable form in terms of a localised basis of support functions $\phi_{i\alpha}$

$$\rho(\mathbf{r}, \mathbf{r}') = \sum_{i\alpha, j\beta} \phi_{i\alpha}(\mathbf{r}) K_{i\alpha, j\beta} \phi_{j\beta}(\mathbf{r}') \tag{6.3}$$

Where $\phi_{i\alpha}$ is the α^{th} support function centred on atom i. Support functions are a non-orthogonal basis set of localised orbitals, and have an overlap matrix given by:

$$\mathbf{S}_{\alpha,\beta} = \int \phi_{i\alpha}(\mathbf{r})\, \phi_{j\beta}(\mathbf{r})\, \mathrm{d}\mathbf{r} \tag{6.4}$$

Support functions themselves are flexible, and are in turn expanded in a set of basis functions. Two options for this basis set representation exist in Conquest, pseudo-atomic orbitals (PAOs)[202], or blips. Blips allow systematic convergence with the basis set size, in a similar way to plane waves. PAOs cannot be systematically converged in an easy manner, but typically produce comparable results with significantly smaller basis set sizes than blips. All of the RT-TDDFT work in this thesis uses the PAO basis set, with the implementation using the blip basis an important piece of work to be carried out in future.

6.2.2 Real Time TDDFT

Expanding the time-dependent Kohn-Sham equations in the basis of our set of non-orthogonal support functions, in the instance where the support functions are stationary with time, gives

$$i\frac{\partial}{\partial t}|\mathbf{c}(t)\rangle = \mathbf{S}^{-1}\mathbf{H}|\mathbf{c}(t)\rangle \tag{6.5}$$

and

$$i\frac{\partial}{\partial t}\langle\mathbf{c}(t)| = -\langle\mathbf{c}(t)|\mathbf{H}\mathbf{S}^{-1} \tag{6.6}$$

allowing us to write the quantum Liouville equation of motion for our auxiliary density matrix $\mathbf{K}$ in the non-orthogonal support function basis:

$$i\dot{\mathbf{K}} = \mathbf{S}^{-1}\mathbf{H}\mathbf{K} - \mathbf{K}\mathbf{H}\mathbf{S}^{-1} \tag{6.7}$$

The formal solution to this equation can be expressed as:

$$\mathbf{K}(t) = \mathbf{U}(t,t_0)\mathbf{K}(t_0)\mathbf{U}^{\dagger}(t_0,t) \tag{6.8}$$

where $\mathbf{U}(t,t_0)$ is a propagator satisfying both:

$$|\mathbf{c(t)}\rangle = \mathbf{U}(t,t_0)|\mathbf{c}(t_0)\rangle \tag{6.9}$$

$$i\frac{\partial}{\partial t}\mathbf{U}(t,t_0) = \mathbf{S}^{-1}\mathbf{H}\mathbf{U}(t,t_0) \tag{6.10}$$

Expressing the propagator in integral form we have:

$$\mathbf{U}(t,t_0) = \mathcal{T}\exp\left\{-i\int_{t_0}^{t}\mathrm{d}\,\tau\mathbf{S}^{-1}\mathbf{H}(\tau)\right\} \tag{6.11}$$

where $\mathcal{T}$ is the time ordering operator. Evolution of the system for a total time, $T = n\Delta t$, may be carried out piecewise in smaller intervals, allowing us to express the total evolution operator as the product of small time operators:

$$\mathbf{U}(t,t_0) \simeq \prod_{n=0}^{N-1}\mathbf{U}\left((n+1)\,\Delta t, n\Delta t\right) \tag{6.12}$$

where

$$\mathbf{U}(t+\Delta t,t) = \exp\left[-i\mathbf{S}^{-1}\mathbf{H}(\tau)\Delta t\right] \tag{6.13}$$

Evolution of the time dependent system is then reduced to the problem of approximating the propagator $\mathbf{U}(t+\Delta t,t)$. Two approximations exist in the definition of $\mathbf{U}(t+\Delta t,t)$, firstly that of approximating the matrix exponential $\exp(\mathbf{A})$ and secondly the exact form of the matrix

for which we wish to calulate the exponential. There are several methods for calulating the exponential of a matrix [203], here we use the simplest approximation, a Taylor expansion:

$$\exp(\mathbf{A}\Delta t) = \mathbf{I} + \sum_{n=0}^{\infty} \frac{(\mathbf{A}\Delta t)^n}{n!} \tag{6.14}$$

Similarly there are many different approaches for deciding which matrix exponential to use as a propagator. All of the approximations implemented are taken from the work of Marques et al.[204] on RT-TDDFT propagators, and are briefly decribed here for completeness.

The exponential midpoint propagator approximates the $\mathbf{U}(t + \Delta t, t)$ by the exponential taken at $\tau = t + \Delta t/2$:

$$\mathbf{U}_{EM}(t + \Delta t, t) = \exp\left\{-i\mathbf{S}^{-1}\mathbf{H}\left(t + \frac{\Delta t}{2}\right)\right\} \tag{6.15}$$

Implicitly enforcing time-reversibility, such that propagating forward from t and backwards from $t + \Delta t$ by $\Delta t/2$ produce the same result, provides the so called *enforced time-reversal symmetry* method.

$$\begin{aligned}\mathbf{U}_{ETRS}(t + \Delta t, t) = &\exp\left\{-i\frac{\Delta t}{2}\mathbf{S}^{-1}\mathbf{H}\left(t + \Delta t\right)\right\} \\ &\times \exp\left\{-i\frac{\Delta t}{2}\mathbf{S}^{-1}\mathbf{H}\left(t\right)\right\}\end{aligned} \tag{6.16}$$

Using the Magnus operator the exponential solution to Schrödinger equation for a time-dependent Hamiltonian may be written as[205]:

$$\mathbf{U}_{M4}(t + \Delta t, t) = \exp\left\{M_{G4}\right\} \tag{6.17}$$

where $\mathbf{M}_{\text{G4}}$ is an infinite series of integrals providing an exact solution. Truncating this expansion to fourth order and approximating the integrals using Gauss-Legendre points as in [204] gives in our non-orthogonal basis:

$$\begin{aligned}M_{G4} = &- i\frac{\Delta t}{2}\left[\mathbf{S}^{-1}\mathbf{H}(t_1) + \mathbf{S}^{-1}\mathbf{H}(t_2)\right] \\ &- \frac{\sqrt{3}\Delta t^2}{12}\left[\mathbf{S}^{-1}\mathbf{H}(t_2), \mathbf{S}^{-1}\mathbf{H}(t_1)\right]\end{aligned} \tag{6.18}$$

where $t_{2,1} = t + [1/2 \pm \sqrt{3}/6]\Delta t$.

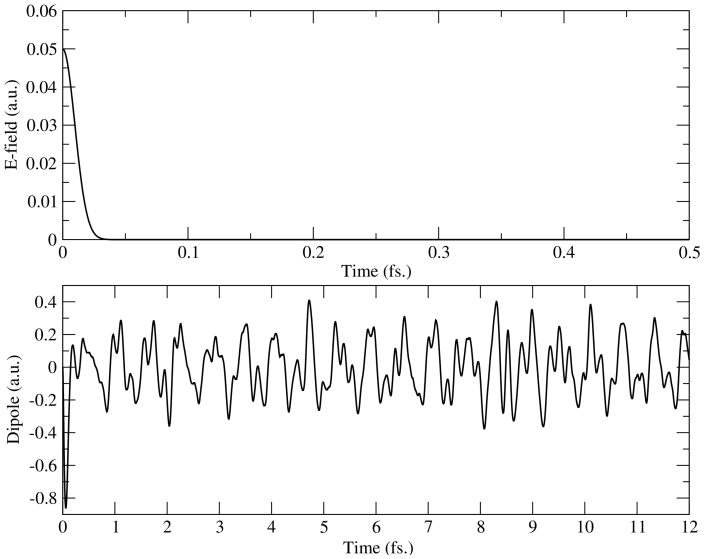

Figure 6.1: Applied electric field and induced dipole moment for a benzene molecule. ($\Delta t = 0.03$ a.u. ≈ 0.00073 fs.)

6.2.3 Linear Response

Propagating in real time provides direct access to the time-dependent charge density, and therefore the electronic response to external fields. Applying a time dependent external electric field polarised along axis *j*,

$$\delta v_{ext}\left(\mathbf{r},t\right) = -\mathbf{E}_j(t)\cdot\mathbf{r}$$

allows us to examine the time-dependent response of the system. Application of this electric field will produce an induced time-dependent dipole moment:

$$\mathbf{P}\left(t\right) = \mathbf{P}\left(0\right) - \int \mathrm{d}\mathbf{r}\, n\left(\mathbf{r},t\right)\mathbf{r}. \tag{6.19}$$

As an example of the calculated repsonse of a system to an applied electric field, figure 6.1 illustrates the induced dipole response of a benzene molecule on application of a field with a Gaussian time profile, centred at $t = 0$.

Access to the time-dependent dipole moment allows us to calculate the time dependent polarisability:

$$\alpha_{ij}(\omega) = \frac{\int \mathrm{dt}\, e^{i\omega t} P_i(t)}{\int \mathrm{dt}\, e^{i\omega t} E_j(t)}$$

The imaginary part of the polarisability is directly proportional to the absorption cross section, $\sigma(\omega)$ and the experimentally observed strength function, $S(\omega)$.

$$S(\omega) = \frac{2\omega}{\pi} Im\left(\frac{1}{3} Tr\left(\alpha_{\mu j}(\omega)\right)\right) \tag{6.20}$$

Density matrix RT-TDDFT therefore has the potential to be an extremely useful tool for theoretically predicting the electronic absorption spectra of large systems.

6.3 Propagator Unitarity

We wish the total charge in our system to remain stable, and in order for this to be the case the propagators must be unitary with respect to the overlap matrix. Conserving total probability,

$$P(t+\Delta t) = \mathbf{c}^*(t+\Delta t)\mathbf{S}\mathbf{c}(t+\Delta t) \tag{6.21}$$

$$= \mathbf{c}^*(t)\mathbf{U}^\dagger\mathbf{S}\mathbf{U}\mathbf{c}(t) \tag{6.22}$$

$$= P(t) \tag{6.23}$$

we see that in order for the above to be true, and for the total charge to be conserved, the following must hold:

$$\mathbf{U}^\dagger\mathbf{S}\mathbf{U} - \mathbf{S} = 0 \tag{6.24}$$

From our approximation for the matrix exponential 6.14 we see that, if it were exact, our propagators would indeed exhibit this property. However, as it is impossible for us to store an infinite sum on our computer, we must truncate our Taylor expansion at some point. Doing so will introduce errors, with two factors affecting the scale of the break from S-unitarity; the time step and the number of terms in our summation. While we can extend our expansion arbitrarily, and reduce the time step arbitrarily, we wish to avoid excess computational expense by keeping the expansion as small as possible and the time step as large as possible within some acceptable margin of accuracy. We can directly examine the unitarity of our propagators through equation 6.24.

6.3.1 Time-Step Dependence

As a test we have examined the extent of the break from unitarity for a range of time-steps and number of terms in the matrix exponential expansion. We have used a small molecule for

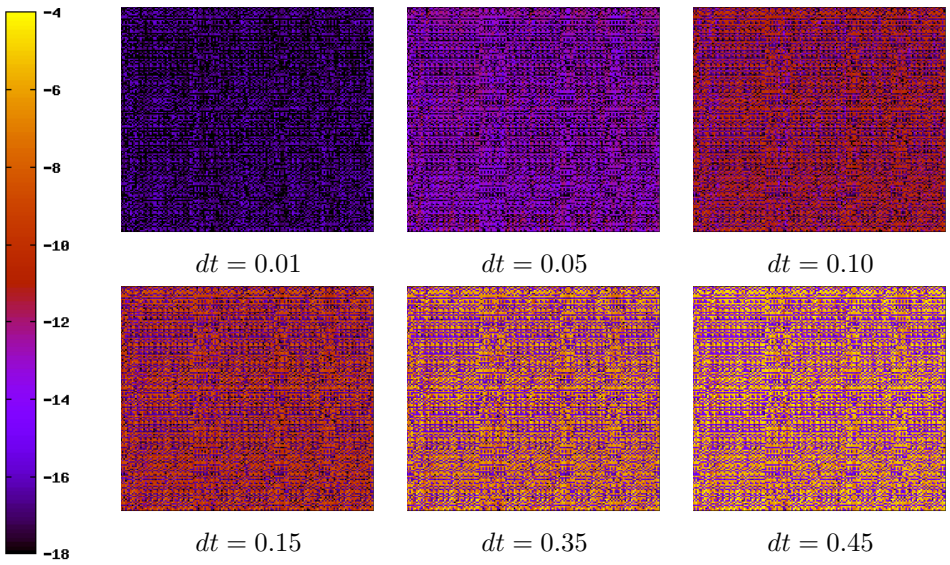

Figure 6.2: Plot of the absolute values of matrix $\mathbf{U}^{\dagger}\mathbf{S}\mathbf{U} - \mathbf{S}$ (on a base 10 log scale), illustrating the propagator unitarity for the exponential midpoint propagator, for varying time step sizes (in au.). The system studied is a single benzene molecule, and the matrix is shown at the end of a 10 au. run.

the purpose, benzene, with a small applied electric field perturbation with a Gaussian profile centered on $t = 0$ (as in figure 6.1).

Exhibited in figure 6.2 we can see the dependence on simulation time step of the propagator unitarity, with the obvious trend being that as the time step is reduced the propagator approaches unitarity. We can see that even for time steps up to ~ 0.15 a.u. the propagator maintains its unitarity to a high degree (similar results were obtained for each of the propagators). The corresponding effect on the charge conservation can be seen in figure 6.3 and, as expected we see that as the time step increases the conservation of charge deteriorates with the propagation eventually becoming unstable for large timesteps.

Examining the form of our propagators we see that for each we require the extrapolation of the Hamiltonian matrix to some unknown point beyond the current time t, $\mathbf{H}_{+}$. As suggested by Marques et al.[204] in order to minimise errors it is possible to carry this procedure out self-consistently. In our case meaning that we propagate $\mathbf{K}(t)$ to $\mathbf{K}(t + \Delta t)$ based on an extrapolated Hamiltonian. We then construct a new Hamiltonian matrix $\mathbf{H}(t + \Delta t)$ using $\mathbf{K}(t + \Delta t)$. $\mathbf{H}_{+}$ can then be interpolated from Hamiltonian matrices for times up to and including $(t + \Delta t)$, and the whole procedure is iterated until some self-consistency criteria is obtained. The effect of not performing this self-consistency procedure on the charge con-

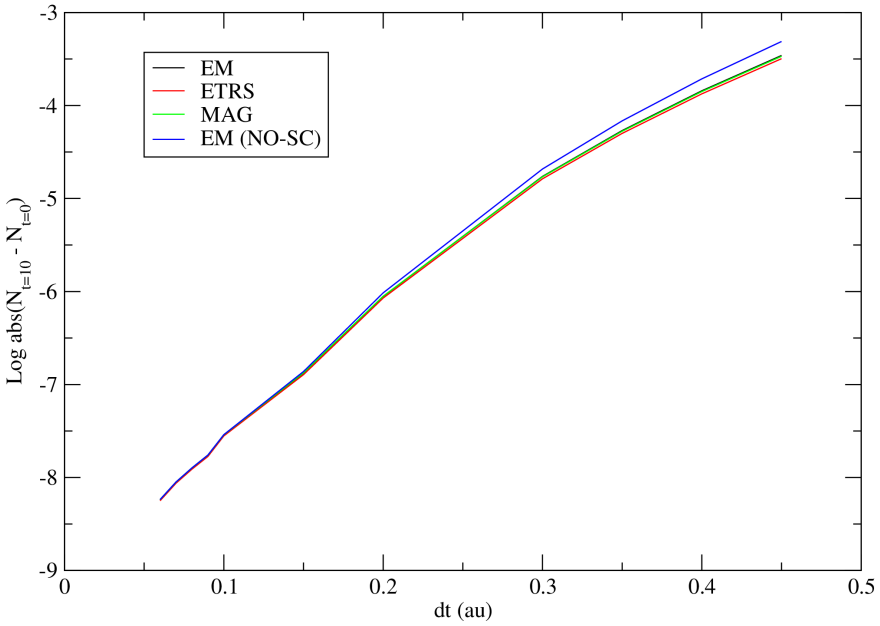

Figure 6.3: Variation in total charge (on a base 10 log scale) with time step size, following a 10 au. run for benzene using all three propagators. Also included is charge variation for the EM propagator without the self-consistent propagator step (see text for details).

servation can be seen in figure 6.3. While the self-consistency cycle is found to improve the charge conservation, in reality for small time steps the difference in charge conservation and calculated properties is not found to be significant enough to warrant the extra computational load of constructing the Hamiltonian matrix several times per time-step. As a compromise we enforce the self-consistency only for a small number of steps ($\sim 50 - 100$) at the beginning of a run, typically when our external electric field is applied for the study of the linear response.

A significant point to note is that little difference is exhibited between the calculated results using each of the three propagators in terms of charge conservation, and in general we have found this to be the case. It is reported that for systems with strongly time-dependent Hamiltonians the $\mathbf{U}_{\mathrm{M4}}$ propagator is advantageous[204], but for our present work this is not the case and we have opted for the simplest exponential midpoint propagator throughout.

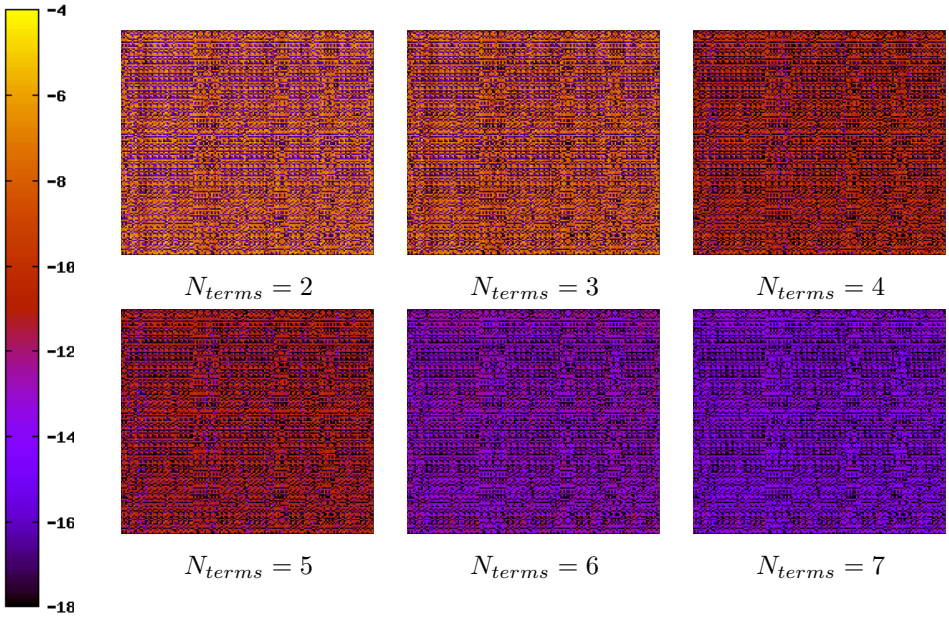

Figure 6.4: Plot of the absolute values of the matrix $\mathbf{U}^{\dagger}\mathbf{S}\mathbf{U} - \mathbf{S}$ (on a base 10 log scale), illustrating the propagator unitarity for the exponential midpoint propagator, for differing number of terms in the Taylor expansion for our propagator. The system studied is a single benzene molecule, and the matrix is shown at the end of a 10 au. run (dt = 0.04 au.)

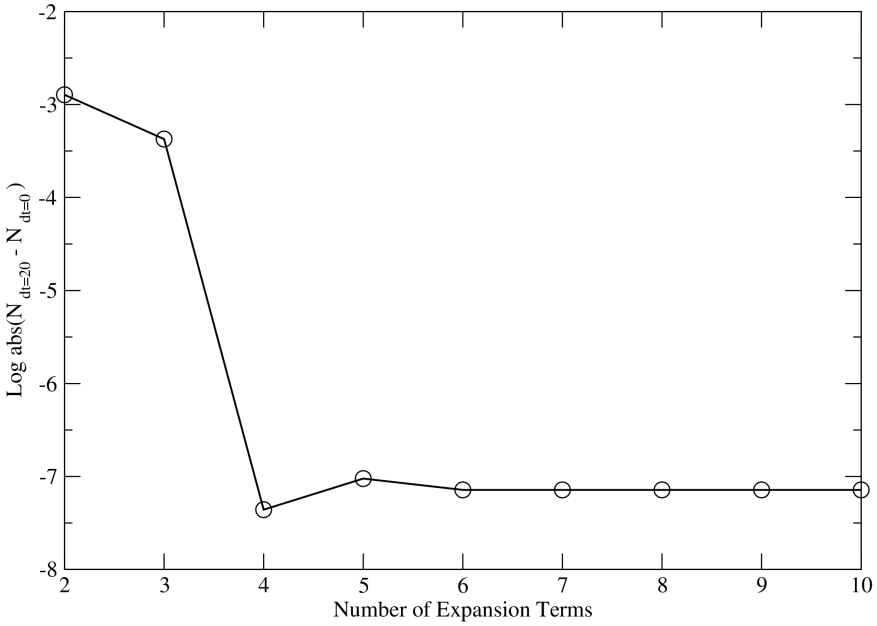

Figure 6.5: Absolute variation in total charge (on a base 10 log scale) with the number of terms in our matrix exponential expansion, following a 20 au. run for benzene using the EM propagator with a time step of 0.04 au.

6.3.2 Matrix Exponential Truncation

The effect of truncating the Taylor expansion used to evaluate the matrix exponential on the unitarity of the propagator can be seen in figure 6.4. We see that reducing the number of terms reduces the unitarity of the propagator, as expected. Looking at figure 6.5 the convergence of the charge conservation with the number of terms in the exponential expansion can be seen. We find that we reach good convergence with six terms included in the expansion, and we opt for this level of accuracy throughout the remainder of the thesis.

6.4 Small Molecules

In order to verify that our implementation is correct we have performed tests on several systems for which the electronic transitions have been studied experimentally and theoretically elsewhere, allowing us to make direct comparisons. For this purpose we have chosen four small molecules (Carbon monoxide, Methane, Ethylene and Benzene) and used our implementation to calculate the optical absorption spectra within the TDLDA approximation.

6.4.1 Identifying Transitions

Meaningful comparison of our results with experiment requires the identification the electronic transitions to which the peaks in our calculated absorption spectra correspond. In Casida's approach information about electronic transitions is inherently produced, while in RT-TDDFT it is not.

It is often possible to reason the corresponding transition by examining the polarisation and energy of peaks and comparing to that of optically allowed transitions experimentally. Where possible, in order to more confidently assign peaks of our calculated absorption spectra to particular electronic transitions, we have followed the procedure in [206] whereby a sinusoidal electric field tuned to a particular excitation mode is applied. A resulting electronic resonance is set up, for example see figure 6.6 for the CO molecule with an applied electronic field corresponding to the first transition.

Examining the difference between the excited charge density at resonance and the ground state charge density, $\rho_{EX} - \rho_{GS}$, allows us to identify the molecular orbitals responsible for the transition. $\rho_{EX} - \rho_{GS}$ for the first valence transitions of both CO and C_2H_4 can be seen in Fig. 6.6. It can be seen that in the case of the CO molecule the lowest energy peak corresponds to an electronic transition from a σ to π^* orbital. Similarly the charge difference for the C_2H_4 can be identified as a transition from a π to π^* orbital, with $\rho_{EX} - \rho_{GS}$ showing good agreement with that reported in [206].

For methane we assumed that the first transition in our absorption spectra corresponds to the first experimentally observed transition. Similarly, given the good agreement between our calculated spectra for C_6H_6 and experiment, we have assumed the well studied π to π^* transition to correspond to our first calculated peak.

Identifying transitions in this manner involves a considerable extra computational overhead, and typically is not performed for most RT-TDDFT calculations. Indeed for larger systems we would expect the method not to be very effective, as more complex resonance pat-

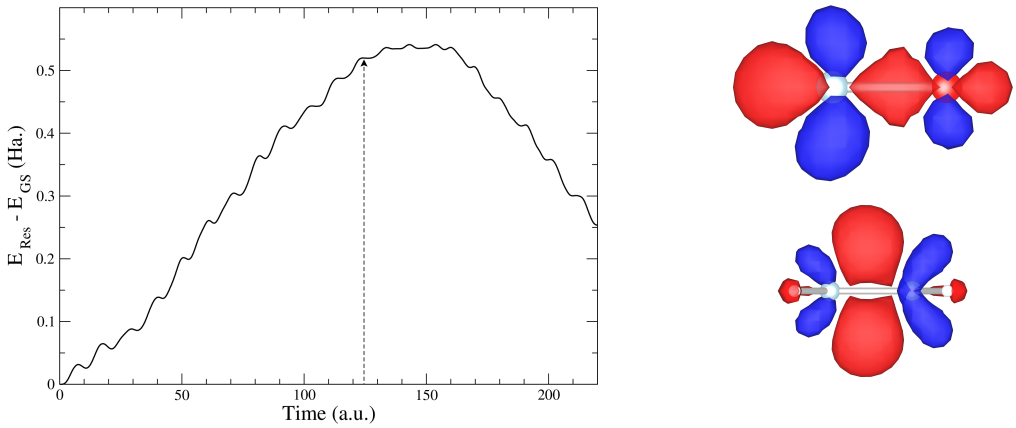

(i) **(ii)**

Figure 6.6: **(i)** Resonant energy difference from the ground state, E_{RES}-E_{GS}, for CO molecule with E-field frequency corresponding to the first transition of the calculated absorption spectrum (Fig. 6.7**(i)**), polarised along the C-O bond. The arrow shows the point at which ρ_{EX} is obtained. **(ii)** Resonant $\rho_{EX} - \rho_{GS}$ for first transitions of CO (top) and C_2H_4 (bottom). Isosurfaces in blue are positive, red are negative.

terns would make obtaining meaningful information about the transitions involved difficult. However it is useful in testing our implementation.

6.4.2 Basis Sets

Our support functions are expanded in a basis of numerical orbitals, in this case pseudo-atomic orbitals generated within the Siesta code [207]. These PAOs are eigenfunctions of the atomic pseudopotentials with a confinement energy shift used to determine a radial cut-off for the orbitals, beyond which they are zero. This confinement energy provides a single parameter to define the cut off radii for different orbitals, and is the energy each orbital obtains on being confined by an infinite potential to a particular radius.

Multiple orbitals per angular momentum channel can be used (multiple-ζ), with the shape of multiple orbitals determined by a split norm procedure[207]. This procedure uses a parameter to define the norm of a numerical orbital outside some radius where they match the tail of the first zeta PAO, and within this radius the vary smoothly to the origin. Subtracting this numerical orbital from the original PAO gives the multiple-zeta orbital. Of course it is possible to define these radii by hand and fine tune the basis set. In addition to multiple zeta, polarisation orbitals can be included within the basis set, and are obtained by solving the same atomic pseudo problem but with an applied electric field.

We use the notation SZ DZ 3Z 4Z to describe single zeta, double zeta, triple zeta and so on. Similarly we descibe the number of polarisation orbitals included in the basis by SZP, SZ2P and SZ3P (one, two and three polarised orbitals respectively).

6.4.3 Benchmark Tests

To first gauge the effect of varying our basis set on the results we have performed calculations on the ethylene molecule with varying numbers of PAOs and two different confinement energies. The basis sets have been generated with a confinement energy of 1 meV and 5 meV, resulting in confinement radii of 4.93 and 4.24 Å for the carbon atoms respectively, and radii of 4.77 and 4.21 Å for the hydrogen atoms respectively. The total run time was 14.51 fs. (600 au.) with a time step of $\sim$0.0242 fs (0.1 au). The results can be seen in table 6.4.3.

Calculated energies for the $\pi \rightarrow 3s$ transition show a wide variation with basis set choice, while the $\pi \rightarrow \pi^*$ valence transition varies less. The effect of systematically increasing the number of basis functions is to improve our results with respect to that of the reference values. Similarly increasing the cut-off radii, by reducing the confinement energy, tends to improve

Transition	Basis Set								Ref[208]	Expt. [209]
	2ZP	2Z2P	3ZP	3Z2P	4ZP	4Z2P	5ZP	5Z2P	3ZP	
1 meV										
$\pi \rightarrow \pi^*$	7.84	7.62	7.73	7.62	7.67	7.62	7.67	7.62	7.45	8.0
$\pi \rightarrow 3s$	8.43	7.95	7.78	7.67	7.46	7.40	7.46	7.29	6.69	7.11
5 meV										
$\pi \rightarrow \pi^*$	7.82	7.73	7.75	7.69	7.70	7.68	7.67	7.67	7.45	8.0
$\pi \rightarrow 3s$	10.64	8.03	7.88	7.76	7.57	7.51	7.46	7.45	6.69	7.11

Table 6.1: Basis set dependence of calculated TDLDA transition energies (eV.) for first valence ($\pi \rightarrow \pi^*$) and Rydberg ($\pi \rightarrow 3s$) excitations for the C_2H_4 molecule.

Molecule	Transition	RT-TDDFT (eV.)	Ref	Expt
CO	$\sigma \rightarrow \pi^*$	8.17	8.20[210]	8.51[1]
CH_4	$T_2 \rightarrow 3s$	9.22	9.27[211]	9.70[212]
C_2H_4	$\pi \rightarrow \pi^*$	7.48	7.45 [211]	8.00[209]
C_6H_6	$\pi \rightarrow \pi^*$	6.87	$\sim$6.90 [213]	6.90 [2]

Table 6.2: Comparison of calculated TDLDA transition energies for small molecules with other values and experiment. Conquest results obtained with 5Z4P basis sets, with the exception of benzene (2Z2P).

the quality of the result. This is to be expected, as increasing the size of our basis set, while systematically increasing the range, will maximise the variational degrees of freedom available to describe our time dependent density matrix.

However our values are still far from those computed elsewhere, and we find generally that for small molecules it is essential to use a large basis with multiple extended polarisation orbitals in order to produce results in line with other works. In addition we find that fine tuning the radial cut-offs by hand, as opposed to using the confinement energy and split norm procedure, can allow us to improve the quality of our results for small molecules.

Exhibited in table 6.2 are the calculated transitions for our four test molecules. In the case of the smallest molecules (carbon monoxide, ethylene, and methane) a hand tuned 5Z4P basis set is employed. While for benzene the result is obtained using a 2Z2P basis with a 5meV

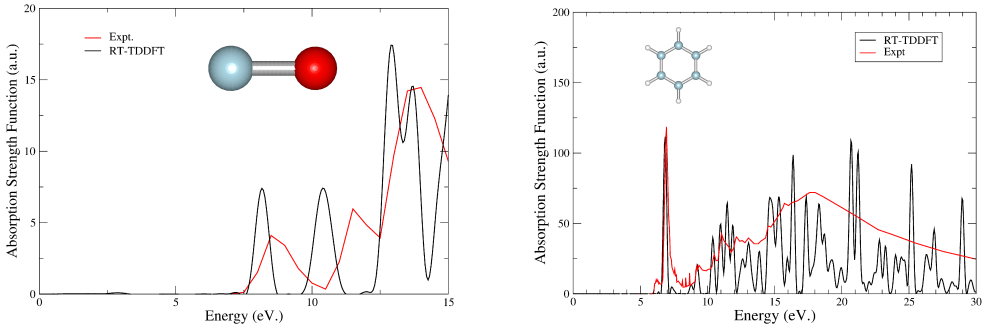

(i) **(ii)**

Figure 6.7: **(i)**: Absorption strength function for carbon monoxide from RT-TDDFT and experiment. Experimental data taken from [1]. **(ii)** Absorption strength function for Benzene from RT-TDDFT. Experimental data taken from [2].

confinement energy. Also presented in figure 6.7 are the optical absorption spectra for the benzene and carbon-monoxide molecules, along with the experimental data.

We can see a strong agreement between our results and that of other studies, giving us confidence in our implementation. Very good agreement is exhibited between the calculated benzene absorption spectra and the experimental values using a reasonably modest 2Z2P basis set. This highlights the point that for larger molecules we generally found that the need large hand tuned basis sets, as is necessary for the smaller molecules, is reduced. Typically results in agreement with those in the literature and experiment are found using smaller basis sets, a point that is important to bear in mind, given the context of linear scaling methods.

6.5 Computational Scaling: Alkane Molecules

In this section we perform calculations on long chain alkane molecules, an example of which can be seen in figure 6.8 ($C_{11}H_{24}$) along with the general chemical structure for an alkane chain. Our aim is to examine the effect of matrix truncation on the propagation of the density matrix, along with the computational scaling with system size.

As a first step we calculate the absorption spectra for the $C_{11}H_{24}$ molecule for several different basis sets using the generalised gradient PBE functional[214] (all further calculations in this section are performed with this functional), and the results can be seen in figure 6.9. Experimentally as the length of the alkane carbon chain increases, the absorption onset is found to reduce, and the reported adsorption onset for $C_{10}H_{22}$ is $\sim$ 175 nm. [215] ($\sim$ 7.1 eV.). We see that as the number of PAOs in the basis set is increased the calculated absorption onset

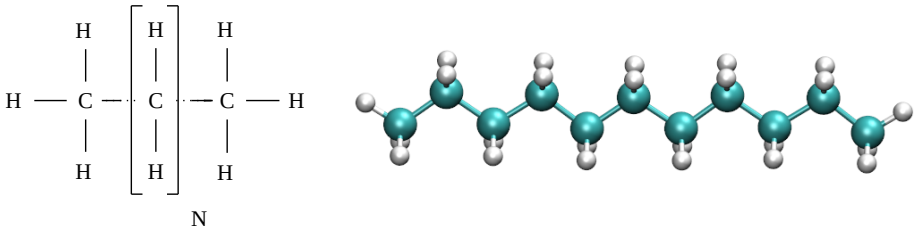

Figure 6.8: Alkane molecule chemical structure (left) and the molecular structure of the $C_{11}H_{24}$ molecule (right).

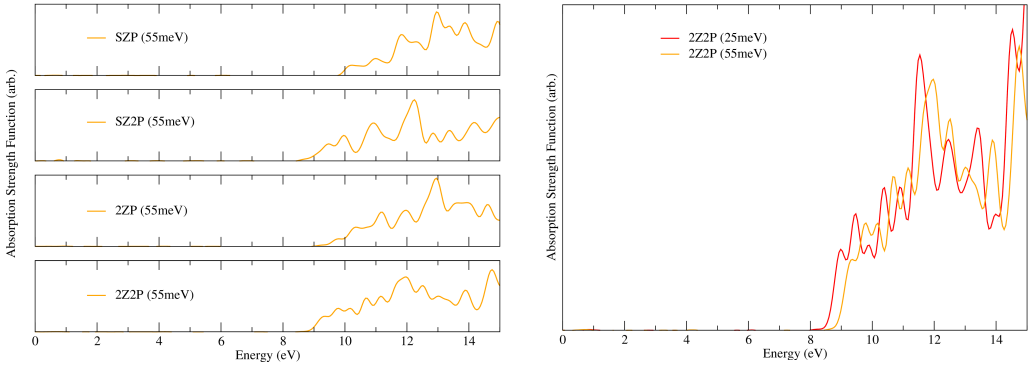

Figure 6.9: Basis set variation of the calculated alkane optical absorption spectra. Effect of increasing the number of PAOs in the basis set(left) and the effect of extending the radii of the basis functions(right) are shown.

approaches this value. Particularly noticeable is the change of the absorption energy caused by the addition of polarisation orbitals. Similarly a significant shift is induced by extending the range of the PAOs (a variation from 55 meV to 25 meV in the confinement energy extends the radii of the carbon and hydrogen basis sets by $\sim$ 0.35 Å and 0.33 Å respectively). This is understandable, given that the first transitions in the alkane molecules are reported as being Rydberg in character[215], we would expect the addition or more diffuse PAOs to improve the description of these excitations. Given the well documented difficulties of TDDFT to accurately describe Rydberg transitions [216], and given that this is not our aim in any case, we proceed to carry out our tests with the SZP and SZ2P basis sets generated using a confinement energy of 55meV (radial cut off for the PAOs is 3.31Å and 3.12Å for carbon and hydrogen respectively).

It is worth noting that several previous works have been done on linear scaling TDDFT

(for a review see [217]). Our approach closely resembles that of Chen et. al. [193, 194, 195, 196, 197]. Indeed Chen et al. have previously studied the long chain alkanes within the linear scaling excited state regime [218].

6.5.1 Propagator Truncation

Within the linear scaling DFT regime of Conquest the density matrix is minimised subject to several constraints. One of these constraints, imposing idempotency on the density matrix, requires the inverse of the overlap matrix. In the case of TDDFT we also require the inverse of the overlap matrix for our propagation, as seen in equation 6.13, due to the non-orthogonal nature of our basis set. In order to compute the inverse overlap matrix Conquest uses Hotelling's method[219], however for poorly conditioned overlap matrices computing the inverse overlap matrix can prove difficult. In our current implementation of TDDFT the atoms remain stationary and so too, therefore, does the overlap matrix. Therefore we have also included the possibility of computing the inverse overlap with the SCALAPACK routines. Although the scaling will not be linear, computing the inverse overlap in this way makes only a relatively small contribution to our total TDDFT runtime, as we only calculate the inverse overlap once at $t = 0$.

While it is apparent that the overlap matrix will be sparse, allowing it to be truncated, the inverse of a sparse matrix will not in general be sparse itself. We have therefore tested the effect of truncating both the $\mathbf{S}^{-1}$ matrix and the $\mathbf{S}^{-1}\mathbf{H}$ matrix on the propagation. Figure 6.10 shows the average absolute error in the matrix elements of $\mathbf{S}^{-1}$ and the $\mathbf{S}^{-1}\mathbf{H}$ matrices caused by truncation (the error in $\mathbf{S}^{-1}$ elements given is the average of the elements of the $\mathbf{S}^{-1}\mathbf{S}$-$\mathbf{I}$ matrix, and the error in the $\mathbf{S}^{-1}\mathbf{H}$ is calculated with a full range $\mathbf{S}^{-1}$ matrix.).

As the range of the matrices increases the error caused by the truncation converges towards zero, as we expect. The $\mathbf{S}^{-1}$ matrix converges less quickly than the $\mathbf{S}^{-1}\mathbf{H}$ matrix, indicating that it is more dense than the $\mathbf{S}^{-1}\mathbf{H}$ matrix. The effect truncation of these matrices has on the unitarity of the propagators can be seen in figure 6.11. We see that the unitarity converges as the $\mathbf{S}^{-1}\mathbf{H}$ range increases, and the propagators are converged with a range of around $\sim$ 22.5-27.5 Bohr. This indicates that the $\mathbf{S}^{-1}\mathbf{H}$ matrix is indeed sparse, and we can safely truncate it. Similarly it makes sense to truncate the $\mathbf{S}^{-1}$ matrix, given that we are truncating $\mathbf{S}^{-1}\mathbf{H}$ and that the Hamiltonian matrix is sparse. We can see this by noting that the unitarity of the propagator in figure 6.11 is also well converged for each of the truncation ranges imposed on the inverse overlap.

As additional atoms are added the Hamiltonian matrix, overlap matrix, and the inverse

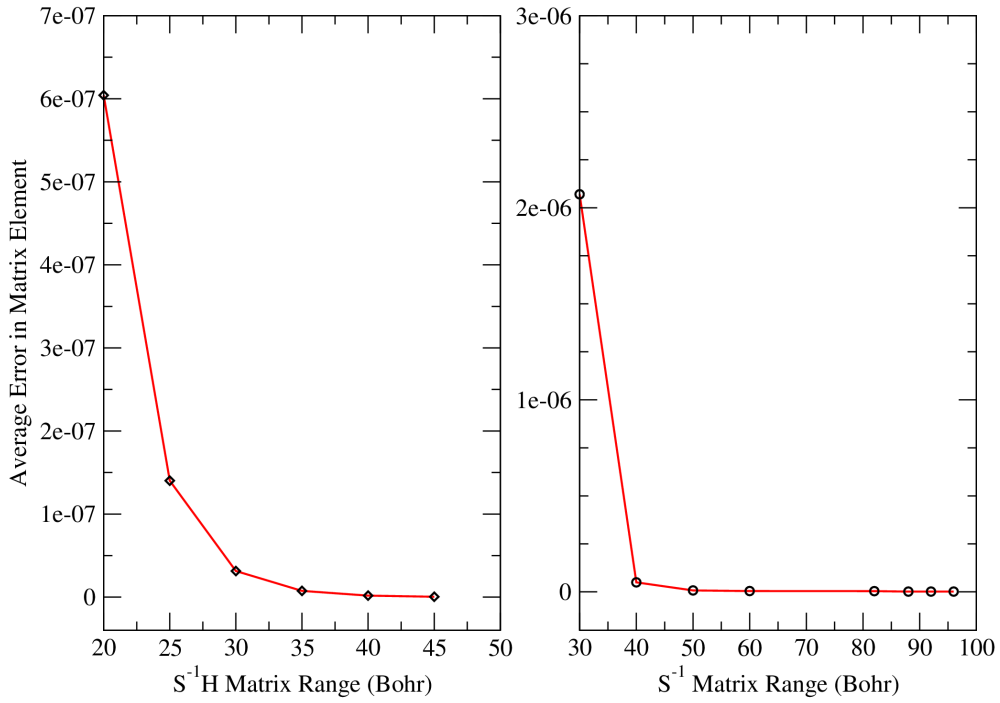

Figure 6.10: Average absolute error in the $\mathbf{S}^{-1}\mathbf{H}$ (left) and $\mathbf{S}^{-1}$ (right) matrix elements with matrix range for the $C_{47}H_{96}$ molecule. SZP basis set is used, generated with a 55meV confinement potential.

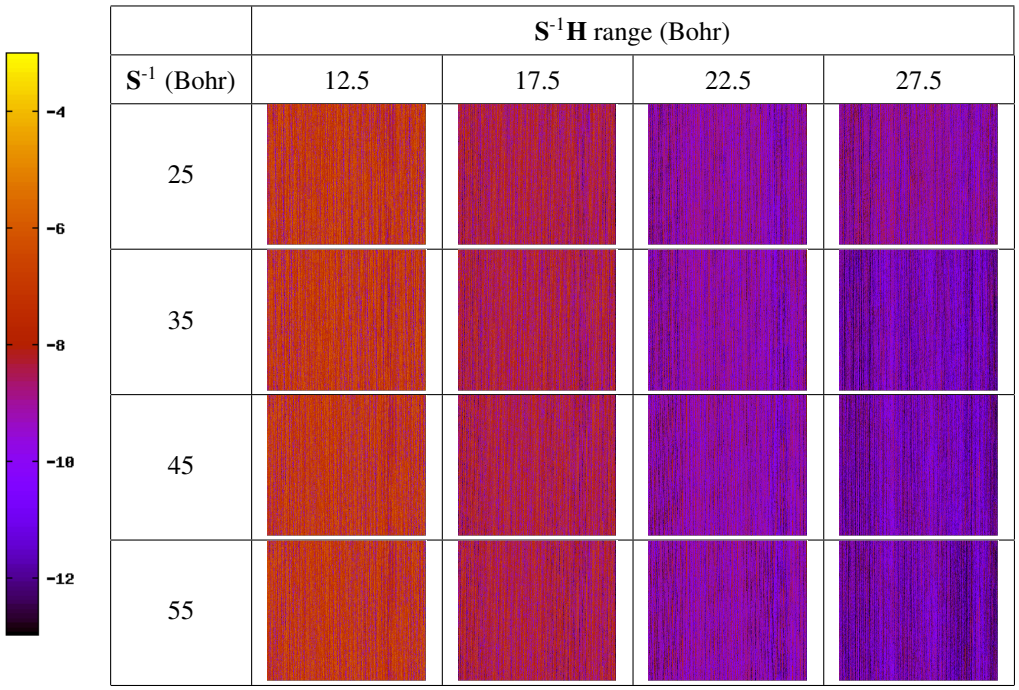

Figure 6.11: Plot of the absolute values of the matrix $\mathbf{U}^{\dagger}\mathbf{S}\mathbf{U} - \mathbf{S}$ (on a base 10 log scale), illustrating the propagator unitarity for differing truncation ranges of the $\mathbf{S}^{-1}$ and $\mathbf{S}^{-1}\mathbf{H}$ matrices for the $C_{47}H_{96}$ molecule

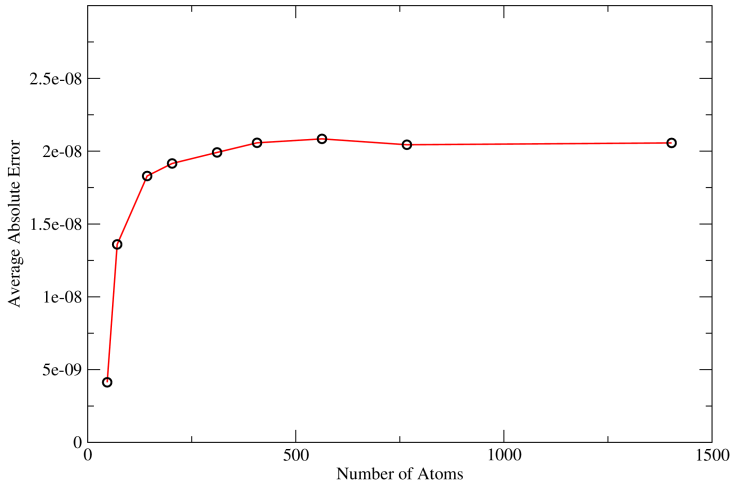

Figure 6.12: Average absolute error in the $\mathbf{S}^{-1}\mathbf{H}$ matrix elements with system size.

overlap will vary. Increasing the system size may therefore affect the ranges of these matrices. We have tested this effect by fixing the $\mathbf{S}^{-1}$ and $\mathbf{S}^{-1}\mathbf{H}$ ranges at 30 and 35 Bohr respectively, and examined the error in the truncated $\mathbf{S}^{-1}\mathbf{H}$ matrix with system size with the results shown in figure6.12. We see that the error changes slightly on increasing system size, but converges as the size increases. Consequently the propagator unitarity was found to exhibit the same trend. This illustrates that the $\mathbf{S}^{-1}\mathbf{H}$ is well ranged, irrespective of system size, allowing us to impose a cut-off radii on both of these matrices. In effect this ensures that as the system size increases, the computational load can be made to scale linearly.

Similarly, increasing the number of basis functions will directly affect the overlap matrix, and consequently the inverse overlap and the propagator. In order to gauge the extent of this effect we have examined the $C_{103}H_{208}$ molecule with a larger basis set (SZ2P). Exhibited in figure 6.13 is the absolute value of the $\mathbf{U}^{\dagger}\mathbf{S}\mathbf{U} - \mathbf{S}$ matrix with $\mathbf{S}^{-1}\mathbf{H}$ matrix truncation range. Despite the larger number of basis set functions we see that the $\mathbf{S}^{-1}\mathbf{H}$ matrix is still well ranged, although the range is wider, and again a truncation will lead to a computational load that scales linearly with system size.

A further point to note is that it is possible to avoid the use of the inverse overlap matrix in the TDDFT propagation altogether. Chen et al. have employed a Cholesky orthogonalisation scheme to bypass the need for the inverse overlap[218]. However using this scheme requires

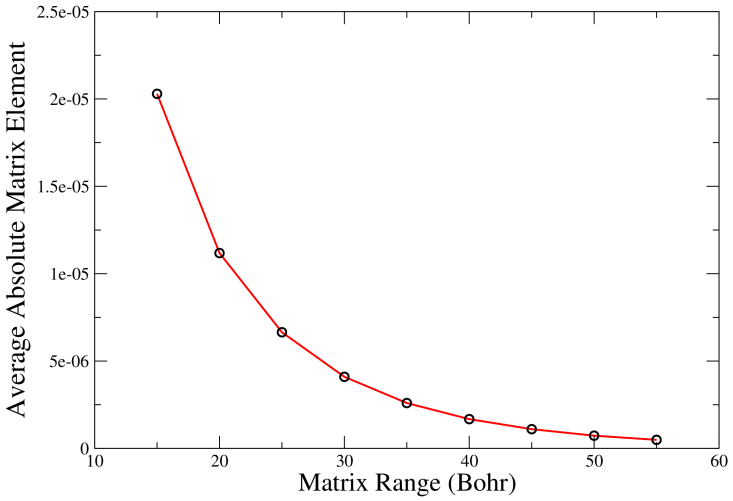

Figure 6.13: Average value of the $\mathbf{U}^{\dagger}\mathbf{S}\mathbf{U} - \mathbf{S}$ matrix with $\mathbf{S}^{-1}\mathbf{H}$ matrix range for the $C_{103}H_{208}$ molecule calculated with a SZ2P basis set.

the inverse of the Cholesky decomposition, and it is not apparent that it will be more sparse than the inverse overlap. It is possible that this scheme might improve the calculation of of the propagator, as the orthogonalised Hamiltonian may be more localised than our $\mathbf{S}^{-1}\mathbf{H}$ matrix. Calculating the Cholesky decomposition can be made to scale linearly, and implementation of this alternative method has already begun in order to contrast the two approaches.

6.5.2 Density Matrix Truncation and Scaling

Finally we examine the effect of truncating the density matrix, and have performed calculations generating spectra for the $C_{47}H_{96}$ molecule at varying truncation radii, R_{Cut}, of the density matrix. The results can be seen in figure 6.14, and generally we find that as the density matrix cut-off increases the spectra tend to converge, as expected, with higher lying states requiring a larger cut-off to converge. We can see from the comparison of $R_{\text{Cut}} = 30$ and $R_{\text{Cut}} = 35$ that there is good agreement for the initial transitions, as well as the general shape of the spectra.

Applying this $R_{Cut} = 35$ Bohr cut-off (along with a cut off of 35 Bohr. on the $\mathbf{S}^{-1}\mathbf{H}$ matrix) we can examine the computational scaling with system size, with the results exhibited in figure 6.15.

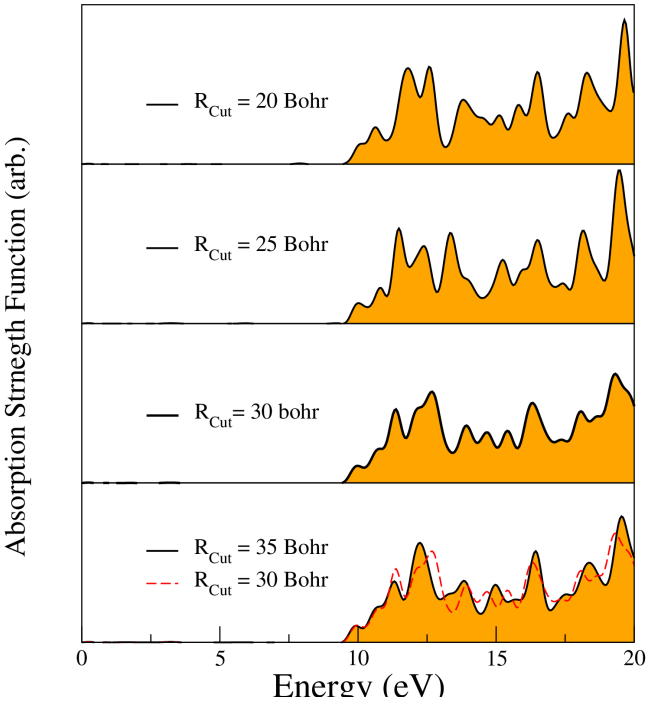

Figure 6.14: K matrix truncation radii dependence: Spectra generated for the $C_{47}H_{96}$ molecule at varying density matrix cut-off radii. (Total run time of 400 a.u. at a time step of 0.05 a.u.)

6.6 Chapter Summary

In this chapter we have introduced the central idea behind a linear scaling, or $\mathcal{O}$(N), density functional theory code and outlined our implementation of real-time time dependent density functional theory in the Conquest $\mathcal{O}$(N) code. We have demonstrated the soundness of the implementation through benchmark tests for small molecules, and also discussed the effect of basis set and system sizes on the results.

$\mathcal{O}(N)$ approaches utilise the density matrix, as opposed to working directly with Kohn-Sham orbitals, providing a route to the linear scaling computational time with system size by its truncation. We have discussed the range of our propagator matrices for an alkane chain test system, and the implications of this matrix truncation on the unitarity of the propagation. Similarly we have examined the effect of truncating the density matrix on the calculated optical absorption spectra, showing that the range required is much more extended than that required for converged ground state properties. While the impact of localisation cut-off in the charge density matrix on these TDDFT calculations is a topic warranting further study, we

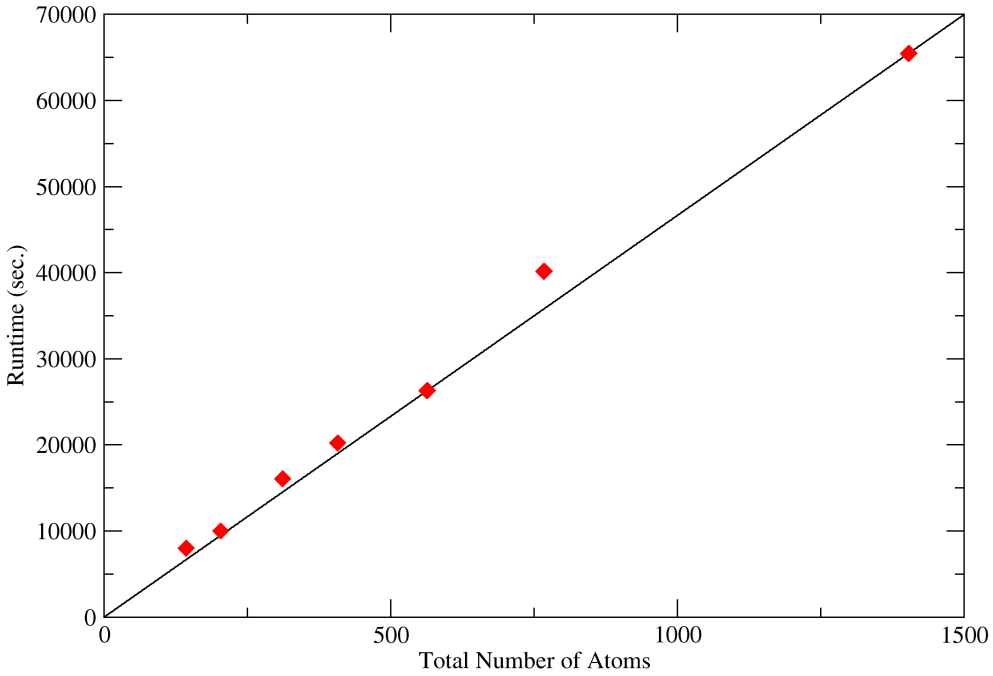

Figure 6.15: Computational TDDFT run time versus system size for long chain alkane molecules. The system was run with a timestep of 0.05 a.u. for a total time of 10 a.u.

have shown that in truncating these matrices at a suitable point we a obtain computational load that increases linearly with system size. This offers a complementary approach to the typical Casida linear response of TDDFT, which scales with system size as $\sim N^6$ and is particularly suited to smaller systems, in that it provides a viable route for studying excitations in larger systems.

Chapter 7

Dye Sensitised Nanoclusters by RT-TDDFT

7.1 Introduction

Titanium dioxide has many technological uses, such as in photocatalysis [220, 221] and of course in dye sensitised solar cells [222]. As we have mentioned, two technologically relevant polymorphs of TiO_2 exist; Rutile and Anatase. Rutile is the more stable of the two in bulk, however TiO_2 nanoclusters (NCs) become more stable in the anatase phase as size decreases [223]. This highlights a significant point in terms of nanostructure properties; *size matters*. For example, adsorption of oxalic acid on TiO_2 NCs has been shown to produce different complexes depending on size [224]. Similarly size has been shown to have an effect on the electronic and optical properties of TiO_2 NCs. Several studies have reported quantum size effects (QSE) resulting in a blue shift of the band-gap on decreasing nanocluster size [225, 226].

Taking the typical exciton Bohr radius in TiO_2 as being in the range 0.8-1.5 nm [227, 228], any computational study examining quantum size effects in TiO_2 NCs must extend beyond this range. For anatase nanoclusters this amounts to performing calculations involving clusters in size beyond $\sim$200 atoms. A recent time dependent density functional tight binding(TD-DFTB) examination of TiO_2 nanoclusters has shown that, for $(TiO_2)_N$ clusters between the range of $30<N<190$ no quantum size effects were found [229]. As an initial study in this chapter we go beyond the TD-DFTB approach and examine the quantum size effects using our density matrix RT-TDDFT, which given its good scaling properties provides an ideal tool

for examining this effect. Our first aim for this chapter is therefore to examine the QSEs in TiO_2 clusters and test the size threshhold for bulk behaviour. We do so by calculating the optical properties for $(TiO_2)_N$ clusters in a wide range containing $16<N<82$ TiO_2 units.

Having used our implementation to examine one major component of DSSCs, TiO_2, we then proceed to use our method to study another major component, sensitising dyes. Designing dyes with an appropriate absorption spectra tuned to the solar irradiance spectrum is extremely important in the engineering of efficient DSSCs, and in studying several dyes we illustrate the extent to which our method can be used as a tool to predict their optical absorption.

As a final study we use both DFT and our RT-TDDFT implementation to examine a model DSSC system, namely the effect of dye adsorption on a small TiO_2 cluster. Using this small model system we generate optical spectra and illustrate the modelling of excited electron injection into the TiO_2. We outline current work we are performing modelling these effects in larger systems, and briefly outline the motivation: to study dye-dye interactions at TiO_2 surfaces.

7.2 Computational Details

All calculations in this chapter have been performed using the CONQUEST DFT code[230, 231], and the TDDFT results presented are obtained using our RT-TDDFT implementation within CONQUEST, outlined in the previous chapter. We perform the calculations using the PBE GGA functional for exchange and correlation[232] and these are set-up such that the studied system is isolated within the cell separated by a vacuum region of at least 20 Bohr.

As the studied systems are not so large in size we employ diagonalisation of the Hamiltonian matrix in order solve the Kohn-Sham equations rather than minimising the energy via the density matrix. Similarly the inverse overlap matrix is obtained using the SCALAPACK routines [233]. Relaxations have been performed using the FIRE algorithm [234] until forces on all atoms are less than 0.0005 Ha/Bohr, and in the case of TDDFT spectra results are generated using relaxed structures obtained using the same level of accuracy as the TDDFT run.

For the TDDFT calculations the extent of the systems studied is not so large as to allow any matrix truncation during the run, and all results exhibited have been performed for full range matrices. For TDDFT the results are obtained using isolated systems in the cell with a sufficient surrounding vacuum so as to ensure no overlap between matrices of adjacent cells so as to avoid errors being introduced in our propagators. Optical spectra are generated by imposing a time dependent electric field, Gaussian in profile and centred on $t = 0$ with peak

height of 0.05 au, polarised in each of the three cartesian directions, as explained in the previous chapter. TDDFT runs are performed for a total run-time of 420 au.(dt=0.07 au), 300 au (dt=0.05 au.) and 400 au (dt=0.05 au.) for the isolated TiO_2, isolated dyes and coupled dye TiO_2 cluster systems respectively.

7.3 QSEs in TiO_2 Nanoclusters

7.3.1 Structural Properties

In this section we describe the set-up of our nanoclusters, and the structural properties once we have relaxed them. As opposed to the more complicated approach of [229] in which spherical clusters are generated by employing molecular dynamics, here we take the simplest method of generating our clusters by taking an extended optimised bulk lattice structure and cutting our clusters directly from it. The five clusters we have chosen to study contain 16, 24, 30, 44 and 82 TiO_2 units respectively. Cutting clusters from the bulk structure in this way is carried out to maximise the co-ordination numbers of the atoms, such that no dangling bonds exist and this leaves a relative excess of Ti atoms in the clusters. In order to obtain a formally neutral system we have removed Ti(4)-O(2) units from the surface of the clusters (where the number in brackets is the coordination number) until they posses the correct stoichiometry. The result of this procedure is a neutral, stoichiometric cluster exposing the (101) and (001) surfaces with all atoms coordinated to at least two others. The clusters before relaxation can be seen in the left hand side of table 7.1.

The right hand side of table 7.1 shows the relaxed cluster structures following optimisation. Significant surface reconstructions are seen to occur for all of the clusters, with the surface Ti-O(2)-Ti bonds buckling and shortening. The Ti-O pair radial distribution function for the largest and smallest clusters can be seen in figure 7.1, and we see that generally as the clusters relax the bond lengths shorten with respect to that of the unrelaxed bulk. Average Ti-O bond lengths can also be seen in table 7.2 and the average bond length increases towards that of the bulk structure as cluster size increases. As the size of the cluster increases the percentage of atoms in the cluster residing on the surface decreases, illustrating that surface reconstructions are responsible for the bond shortening.

	Unrelaxed		Relaxed	
	Side	Top	Side	Top
N=16	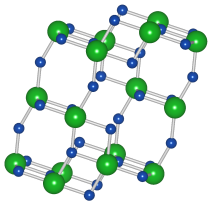	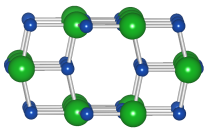	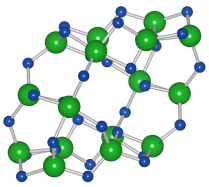	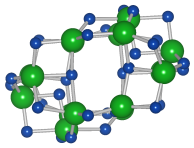
N=26	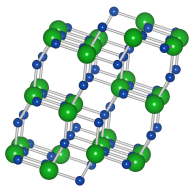	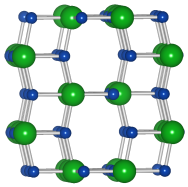	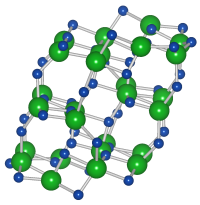	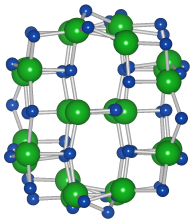
N=30	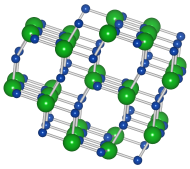	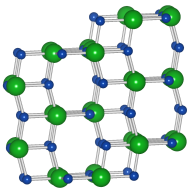	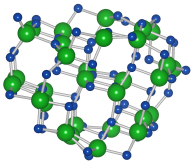	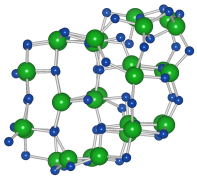
N=44	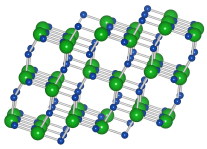	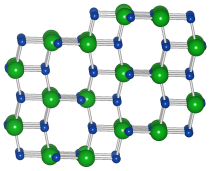	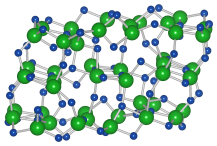	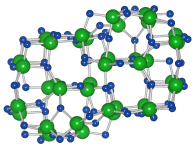
N=82	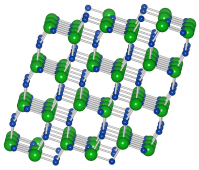	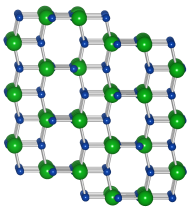	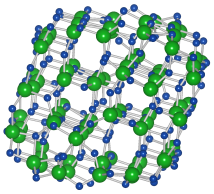	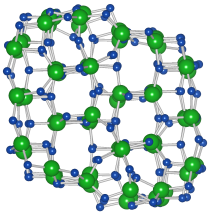

Table 7.1: Unrelaxed (left columns) and relaxed (right columns) $(TiO_2)_N$ clusters examined.

	N				
	16	26	30	44	82
Av. Ti-O Bond Dist(Å)	1.879	1.907	1.914	1.915	1.925

Table 7.2: Size dependence of the calculated average bond distances for TiO_2 clusters.

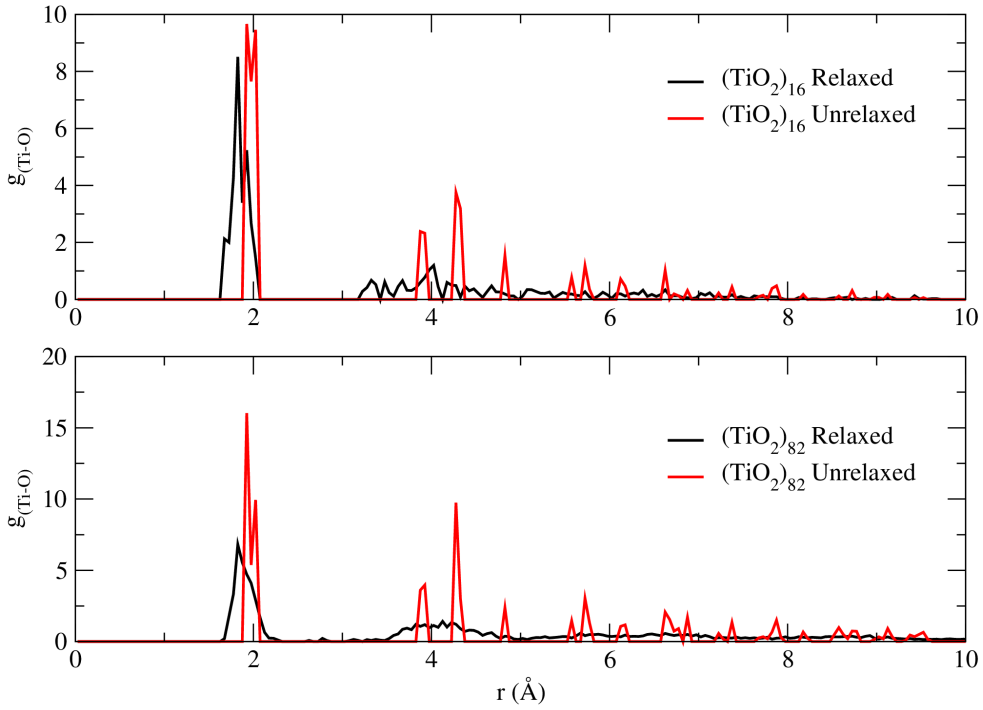

Figure 7.1: Ti-O radial distribution function for the largest and smallest TiO_2 clusters examined

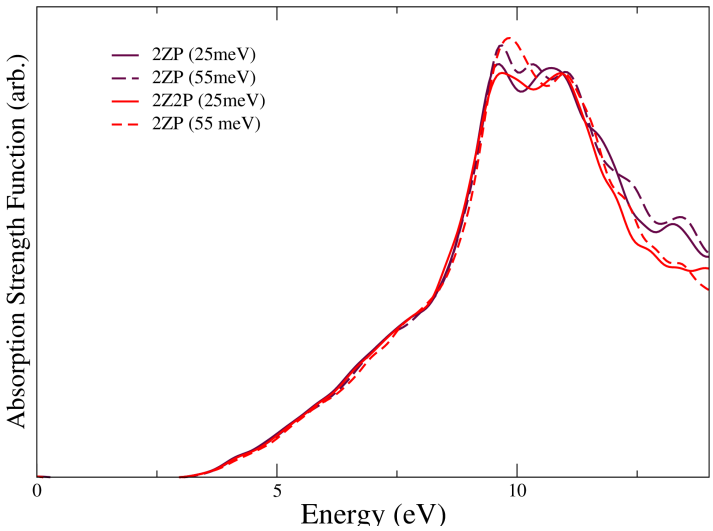

Figure 7.2: Calculated absorption spectra for the $(TiO_2)_{30}$ cluster for different basis sets.

7.3.2 Optical Properties

Following the generation of the relaxed clusters we have calculated the optical absorption spectra for each. As a first step we have tested the basis set dependence on the spectra using the $(TiO_2)_{30}$ cluster for SZP, SZ2P, 2ZP and 2Z2P basis sets. We have also used two different confinement energies (55 meV and 25 meV) when generating the basis sets so as to gauge the effect of extending the PAOs. The results for obtained for the DZP and DZ2P basis sets can be seen in figure 7.2. We see that the general shape of spectra calculated are extremely similar. Practically the same result is obtained for the SZ2P basis, and the SZP basis set results in a significant upwards shift of the higher lying states above the first transitions. While there are small differences between the SZ2P, 2Z2P and 2ZP basis sets, these differences are slight (at most a few meV) around the absorption onset, our region of interest. As such we opt for the 2ZP (55meV) basis set throughout.

The calculated optical absorption spectra for all of the $(TiO_2)_N$ clusters can be seen in figure 7.3, along with the absorption onset. We have employed the same approach as that of [229] to calculate the absorption onset, whereby we have fitted a high order Chebychev polynomial to the data in the region of the absorption edge and then taken a linear extrapolation at the inflexion point to zero. We can see from our result that a definite change in the absorption

onset occurs with material size, with the first transition approaching that of the bulk material as the size increases. This mirrors experimental results to a good degree where the absorption onset for $(TiO_2)_6$, $(TiO_2)_{14}$ and $(TiO_2)_{30}$ anatase clusters are measured as being in the ranges 4.00-4.26, 3.60-3.94 and 3.47-3.78 eV respectively[235]. Our calculated absorption onset for $(TiO_2)_{30}$ does not match perfectly the experimental data, which is to be expected given that there will be differences in the cluster shape. However the experimental shift of the absorption onset in going from $(TiO_2)_{30}$ to $(TiO_2)_{14}$ is $\sim$ 0.1-0.2 eV, and our calculated shift is 0.22 eV in going from $(TiO_2)_{30}$ to $(TiO_2)_{16}$ shows good agreement. We see that there is a large shift in the calculated absorption onset when we increase the size of the cluster to $(TiO_2)_{82}$with this value heading towards that of the bulk anatase value of 3.2 eV. However the values for $N = 26$ and $N = 44$ are identical, and the value for $N = 30$ increases. This can be explained by examining our structures in table 7.1, in which we see that the smallest dimension in any of the three cartesian directions is the same for $N = 26$ and $N = 44$ ($\sim$ 6.5-7 Å). However in increasing the size from $N = 26$ to the $N = 30$ cluster we have introduced a section exposing the (001) face that has a reduced dimension in the (101) direction with respect to that of the $N = 26$ and $N = 44$ clusters (visible on the very left of the $N = 30$ cluster from the side viewpoint in table 7.1), which may contribute to the increase in absorption onset. Certainly we may note that the smallest dimension of the $(TiO_2)_{82}$ cluster in any direction is $\sim$ 10Å, which is significantly larger than that of all of our other clusters.

7.4 Sensitising Dyes

As mentioned, the molecular design of dyes with particular attractive properties is extremely important within the field of DSSCs. One of these properties is the absorption spectra, and tuning it to maximise absorption from the solar spectrum is a key attribute when designing new dyes. The ability to computationally predict the absorption spectra of large complicated dyes is therefore extremely beneficial, and in this section we employ our RT-TDDFT method to calculate the optical absorption spectra of three dyes employed in working DSSCs.

Chemical structures for the dyes we have chosen to examine are exhibited in figure 7.4. Again we have chosen to examine dyes that conform to the typical D-π-A structure used in DSSCs, and in particular the extension of the π conjugated chain. We have selected C343, a coumarin dye based dye and two closely D-π-A related derivatives NKX2311 and NKX2586, all of which have been studied experimentally and theoretically before[3, 236, 237, 238]. Efficiencies of devices utilising these three dyes are ordered C343 (0.9%) $<$ NKX2586 (3.5%)

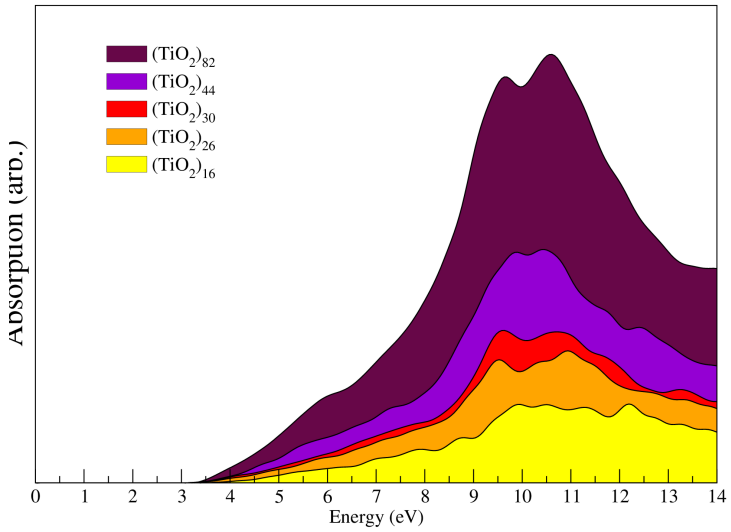

N	E_g (eV) (Å)
16	4.16
26	3.85
30	3.94
44	3.85
82	3.42

Figure 7.3: Calculated absorption spectra for the $(TiO_2)_N$ clusters (left) and absorption energy onset (right).

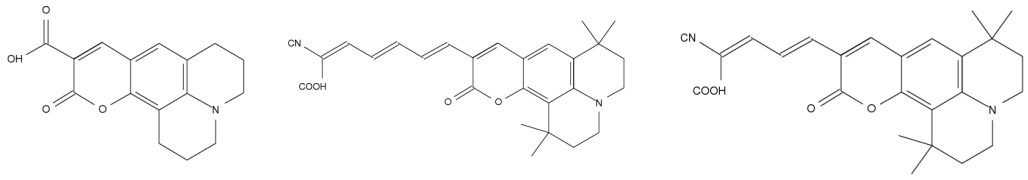

(i) **(ii)** **(iii)**

Figure 7.4: Chemical structures for the examined dye molecules:(i) C343, (ii) NKX-2311, (iii) NKX-2586

$<$ NKX2311 (5.2%), with the decrease in efficiency in going from NKX2586 $\rightarrow$ NKX2311 reported as being due to aggregation effects[3] as a result of the increased π conjugation in the linker moiety.

Calculated absorption spectra for C343, NKX2311 and NKX-2586 can be seen in figures 7.5, 7.6 and 7.7 respectively. Following basis set tests we have generated these spectra using a 2ZP basis, generated with a 25 meV confinement energy. see that our method produces results with varying degrees of success. Results for the C343 dye for the first transition are within $\sim$ 0.25 eV of the first experimental peak, in line with previous work with the PBE functional[237]. Our NKX-2311 spectra improves slightly with respect to that of the experimental data, with the first transition being within $\sim$ 0.2eV of the experimental peak. In the

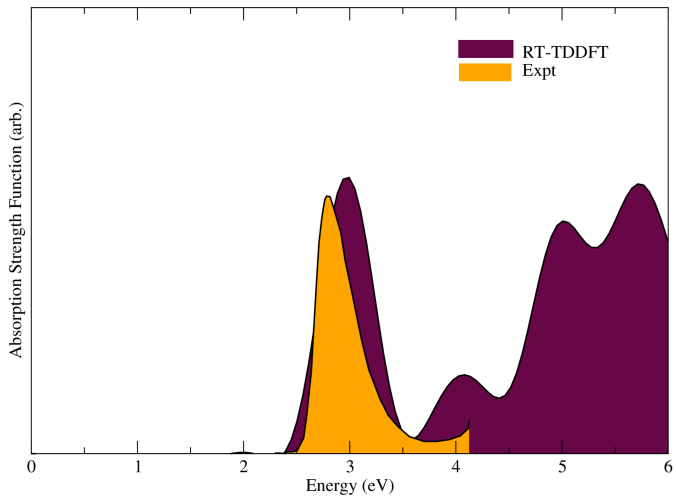

Figure 7.5: Absorption spectra for C343, and comparison to experimental data from [3].

case of these two dyes our results are better than those using the more sophisticated B3LYP functional[237, 239].

However for the NKX-2586 chromophore our results deteriorate slightly, with our calculated first peak being $\sim$ 0.3 eV off that of the experimental data. Again comparing with previous work find our result to be very similar, noting that for this dye previous work using the B3LYP functional is reported as producing results much closer to experiment for the first transition[237, 239]. Our calculated first transition energies follow the trend C343(2.95 eV) $>$ NKX-2311 (2.31 eV) $>$ NKX-2586 (2.14), again illustrating the design mechanism examined in chapter4, that an increase in conjugation length will red-shift the absorption spectra. The slight discrepancy between our results and experiment of around 0.15 eV could potentially be attributed to the neglect of solvation effects, as the addition of a methanol solvent has been shown to lower excitation energies calculated for C343[240].

7.5 Sensitised Nanoclusters

Our intention for this final piece of work had been to examine the dye-dye interactions on the surface of a TiO_2 nanocluster, establishing the effect on optical spectra and charge dynamics at the surface. Comparatively the decrease of efficiency of the NKX-2586 dye with respect to that of the NKX-2311 forms an interesting study, particularly given that the extension of the π conjugated chain in NKX-2586 has been designed to have the opposite effect.

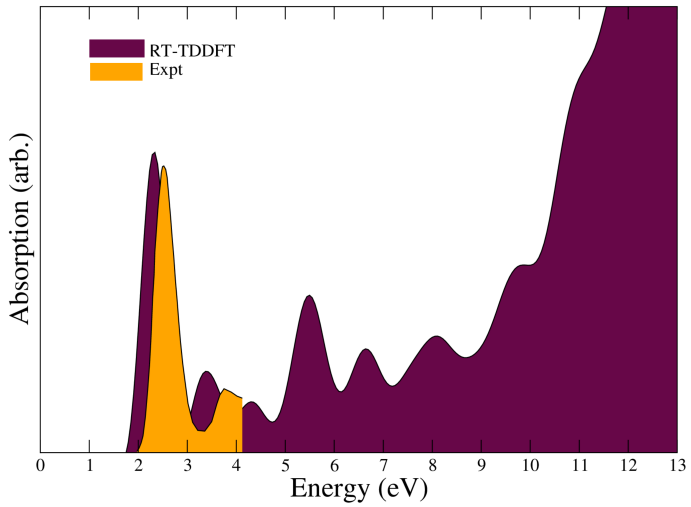

Figure 7.6: Absorption spectra for NKX-2311, and comparison to experimental data from [3].

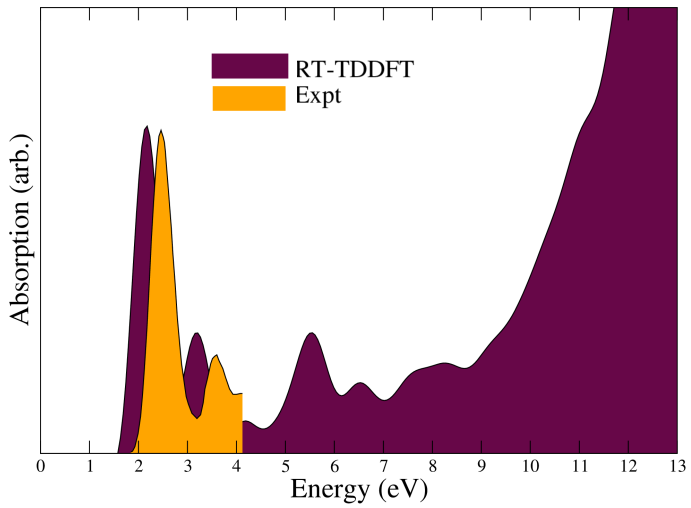

Figure 7.7: Absorption spectra for NKX-2586, and comparison to experimental data from [3].

Studying the aggregation phenonema, as a result of this π extension, is something we have already looked at in chapter 4. Furthering our work in this area by employing our RT-TDDFT method would be beneficial as, given that it is an important effect in defining the efficiency of DSSCs, there has been little work done examining it in DSSCs[241]. Given our earlier demonstration of size effects on the properties of TiO_2 clusters it is not hard to reason why so little work has been done in this area; the extremely large computational loads involved in studying at least two dyes interacting a TiO_2 system, which itself must be large enough to avoid size effects. Our RT-TDDFT method seems like a excellent candidate for tackling this problem.

While we are in the process of performing this study, it is not yet completed, and here in order to illustrate the method we present results on a small test system; namely the C343 dye adsorbed on a $(TiO_2)_8$. We have constructed the $(TiO_2)_8$ based upon the lowest energy structure found in [242], and have not discussed its results above as it has not been constructed in the same manner as those clusters of the previous study. However the calculated absorption onset is 4.05 (eV), significantly larger than that of the $(TiO_2)_{82}$ cluster, in line with the general trend.

We adsorb the C343 molecule in the bidentate bridging mechanism of the previous chapters, binding the disassociate hydrogen to a two-fold coordinated oxygen atom nearby on the cluster surface. Frontier molecular orbitals can be seen in table 7.3, and we note that the HOMO, a state in the band-gap, is completely localised on the C343 dye. The LUMO on the other hand resides almost entirely on the TiO_2 cluster. Previous works have reported that the next dye localised virtual Kohn-Sham orbital is the LUMO+15 (on a $(TiO_2)_9$ cluster)[237]. Here we find that the next unoccupied orbital with a large dye contribution is the LUMO+1 level, and it contains a extremely large contribution from TiO_2 states. There are several factors that could explain this different ordering of the dye localised LUMO with respect to the TiO_2 virtual orbitals, such as the different cluster size and geometry as well as a different binding mechanism employed. Going beyond ground state DFT and performing RT-TDDFT we obtain the optical absorption spectra presented in figure 7.8. Despite the different ordering of the virtual Kohn-Sham orbitals with respect to that found in [237] the TDDFT result is extremely similar. We find a shift of the absorption energy onset, with a transition of smaller oscillator strength at lower energy of around 2.1 eV. The main peak of the transition is red shifted with respect to the that of the free dye, and the peak itself is broadened slightly, which matches the experimental trends seen experimentally when adsorption of C343 on TiO_2 occurs[243].

The reason behind the poor reported efficiency of the C343 dye when employed in DSSCs

HOMO	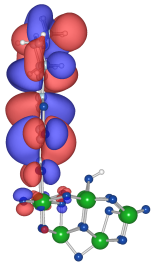	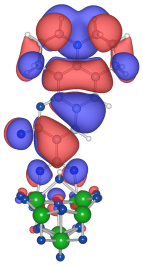
LUMO	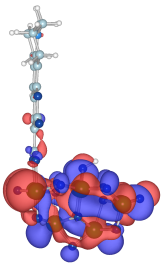	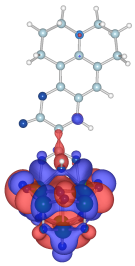
LUMO+1	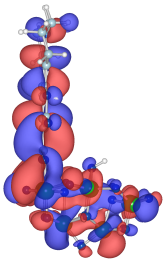	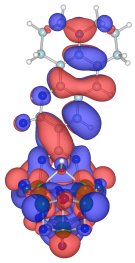
LUMO+2	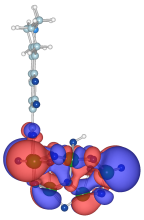	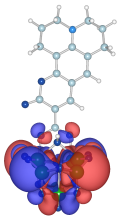
LUMO+3	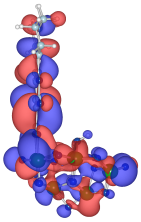	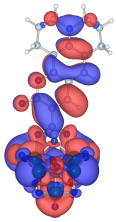

Table 7.3: Frontier molecular orbitals for the C343-$(TiO_2)_8$ system.

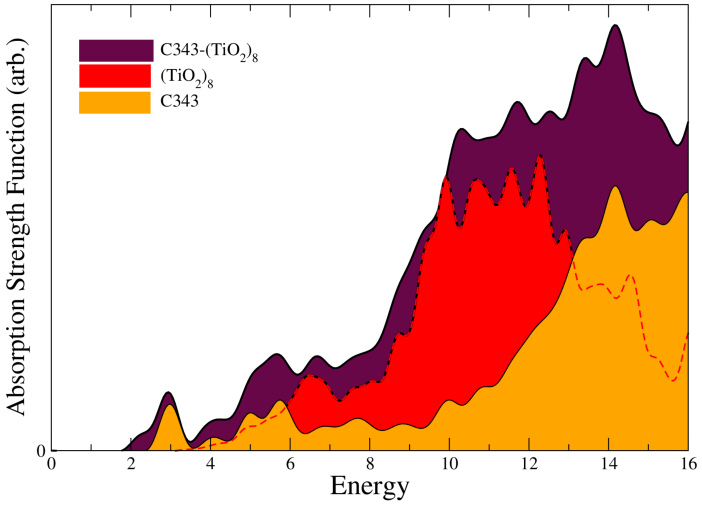

Figure 7.8: Absorption spectra for C343, $(TiO_2)_8$ and the sensitised model system, C343-$(TiO_2)_8$.

can be seen in the fact that, although a transition of small oscillator strength is introduced at an energy of around 2.1 eV, the main peak at $\sim$ 3.0 eV will not provide a significant advantage in terms of absorption of the solar spectrum beyond that of unsensitised anatase. The interest in the C343 dye stems from the closely related larger derivatives of it, such as the NKX-2311 and NKX2586 dyes, which are significantly better sensitisers.

Finally we have attempted to model the electron injection process from the dye excited state into the TiO_2. In order to proceed we have generated an excited state density matrix as a starting point for the calculation by performing a diagonalisation, and shifting an electron from the HOMO to the lowest unoccupied dye-localised state, LUMO+1. Dividing our simulation cell into two separate parts, one containing the dye and another the TiO_2 cluster, we can integrate the charge density in each region to monitor any charge transfer.

Time dependent charge localised on the dye molecule can be seen in figure 7.9, and we see that very little occurs in the way of electron injection. From 7.3 we can see that our LUMO+1 orbital has an extremely strong electronic overlap with the TiO_2 cluster, with a significant portion of the electronic level residing here. Examining the induced charge difference caused as a result of our HOMO$\rightarrow$LUMO+1 promotion, figure 7.9(ii), we can see that the promotion in itself is tantamount to a significant charge injection (with $\sim$ 0.35 electrons transferred to the TiO_2). Now examining the time-dependent dye localised charge, figure 7.9(i), we see in effect a small charge redistribution back to the dye. Potentially over delocalisation of the LUMO+1

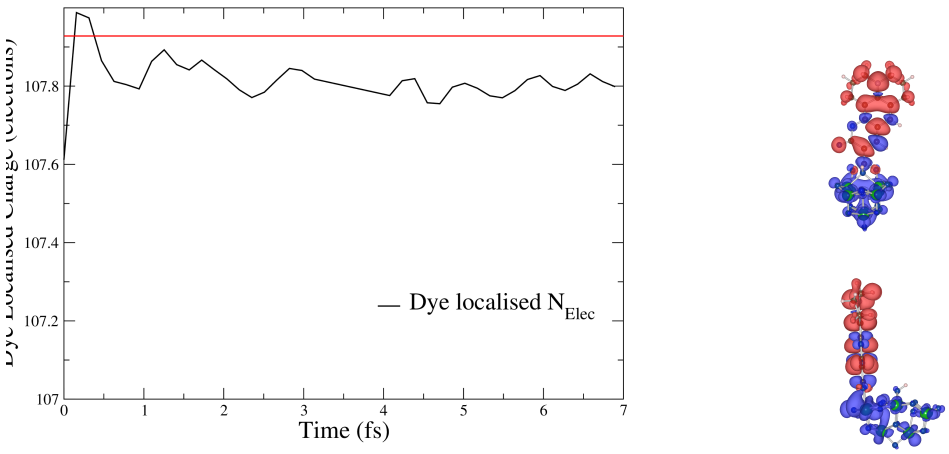

(i) **(ii)**

Figure 7.9: **(i)** Time dependent dye localised charge following promotion from HOMO→LUMO+1. Ground state dye-localised charge is illustrated with red line. **(i)** charge difference density plot for $\rho_{EX} - \rho_{GS}$. The regions of positive charge difference are in blue, those in red are negative.

level, and the limited size of our cluster are the cause of the poor description of charge injection and we can conclude that the naïve promotion of an electron from HOMO→LUMO+1 as a starting excited state is not a viable way forward.

Similar approaches to modelling the charge transfer in TiO_2 using RT-TDDFT have generated a starting system by the addition of a *dye-localised* one particle density matrix to the coupled system density matrix in order to generate a dye localised excitated state[244]. We are exploring the effectiveness of this method. Finally we note the possibility of using constrained-DFT, implemented in the CONQUEST code[245], to generate a dye-localised excited state as a starting point. This method applies an extra potential, that acts as a charge constraint, providing the possibility of localising an excess charge on some part of the system. While it may not be suitable for a small dye such as C343, for larger D-π-A dyes, where the excited state may be approximated as being localised on the anchor, this method offers a novel and interesting avenue of investigation and is one that we are also exploring.

7.6 Chapter Summary

In this chapter we have used our implemented RT-TDDFT in the CONQUEST code to examine two of the main components of DSSCs. Firstly we have studied quantum size effects in TiO_2 nanoclusters, illustrating a clear difference in optical properties with nanocluster size. As the size of the cluster, or rather the size of its smallest dimension, increases the first optical transition approaches that of the TiO_2 band-gap. While experimental work has been performed illustrating that a size dependence on the optical properties exists[235], what it hasn't established is the limit of this size dependence, a question that is of pertinance to the computational physicist working in the field. We have gone some way to establishing this threshhold for bulk behaviour, and shown that for a system containing 82 TiO_2 units the optical absorption onset is still some way above that of the bulk experimental value. An important result, given that those working in the field are typically content to model interactions with TiO_2 nanoclusters using model systems of far fewer atoms.

Next we have calculated the optical absorption spectra for several coumarin dyes used in DSSCs, and found that our method performs admirably, matching experiment well and reproducing results from previous theoretical work to a good degree. Finally we have briefly outlined our ambitions to study dye-dye interactions at the TiO_2 surface, which we feel is an understudied mechanism in DSSCs and well suited to be examined with our density matrix RT-TDDFT. We have briefly demonstrated our method being used to examine a model DSSC system, C343-$(TiO_2)_8$, generating optical spectra and discussed potential avenues for further work exploring the charge injection processes.

Chapter 8

Overview & Conclusions

Theoretical calculations have been presented on several key themes in the science of dye sensitised solar cells, with the motivation being to elucidate the factors affecting efficiency and provide insight to experimentalists working in the field.

Numerous aspects of a DSSC will directly affect the efficiency of the device and we have focused our attentions on some of the most fundamental; namely the interaction of anchors with the TiO_2 electrode, dye design and its affect on interactions at and with the semiconductor surface and the role intrinsic and extrinsic defects have in defining the properties of the electrode.

Optical properties of materials and electron dynamics play an important role in much of nanotechnology, not least DSSCs.With this fact serving as motivation we have implemented and tested RT-TDDFT in the linear scaling CONQUEST code. This computational tool allows the calculation of optical absorption spectra and the modelling of electron dynamics in real-time, and has the potential to do so for large physically realistic systems. As a final study we have employed our implementation to examine dye sensitised TiO_2 nanoclusters and dyes.

8.1 Anchoring to TiO_2

Anchoring of dyes to the TiO_2 surface defines the device stability and dye uptake by the TiO_2 electrode. While other anchoring groups exist the majority of sensitising dyes employ the same method; a carboxylic acid moiety. Similarly the overwhelming majority of DSSCs utilise nanocrystals exposing the prevalent anatase (101) surface. Two avenues of exploration for increasing device efficiencies are the use of nanostructured rutile electrodes, exposing the

(110) surface, and exploiting the enhanced light scattering and increased surface activity of the anatase (001) surface by increasing its exposed area. This led us to examine the validity of employing the prototypical carboxylic acid to anchor dyes irrespective of the majority surface exposed. We carried out a systematic study comparing and contrasting the binding of two underused anchors, boronic and phosphonic acids, with the carboxylic acid, and found a re-ordering of the relative binding strengths of the anchors when attaching to different surfaces. Illustrating that anchoring groups will perform differently on different surfaces, this result provides a useful point for experimentalists that should be taken into consideration when designing senstising dyes. We have also illustrated that the reactivity of the unreconstructed anatase (001) surface provides a platform for extremely strong binding of anchors, making a compelling case for experimentalists to exploit this reactivity by functionalising before surface reconstruction.

8.2 Dye Design

The design of sensitising dyes with desirable properties provides one of the main avenues of research for experimentalists wishing to increase device performance. We have explored two of the most regularly employed design mechanisms; the extension of a π-conjugated linker group in Donor-π-Anchor dyes, as a means of broadening absorption spectra, and the use of non-planar moieties to inhibit aggregation.

We found that, while increasing the conjugated bridge will introduce extra states into the band-gap, providing higher IPCE values, the act of increasing the conjugation also leads to an increased tendency for dyes to aggregate. An important point we have demonstrated is that dipole-dipole interactions between dyes, resulting from the formation of aggregates, can dramatically shift dye localised states in the band-gap. In the case studied these states were shifted downwards counteracting the benefits of extending the conjugated chain. Finally we have demonstrated the effectiveness of including non-planar moieties as design mechanism, by showing that non-planar dyes have a reduced tendency towards aggregation. Both of these conclusions provide useful guidance for experimentalists wishing to design dyes for DSSCs.

8.3 Interplay Between Intrinsic and Extrinsic Defects in TiO_2

Motivated by the increased performance of DSSCs employing TiO_2 electrodes that have been doped with aluminium, we have carried out a systematic study on the effects of Al doping

on the properties of anatase TiO_2. In particular we have examined how the introduced Al defects interact with the intrinsic oxygen vacancy defects and found that movement of oxygen vacancies is likely to lead to clustering of extrinsic and intrinsic defects. We have shown that this intrinsic-extrinsic defect interplay leads to the tri-valent aluminium dopants performing a "clean-up" of the vacancy defect states, thereby reducing the number of Ti^{3+} recombination centres. We have concluded that it is this benign clean up that leads to enhanced DSSC performance, and demonstarted this by showing that a dye adsorbed on an intrinsic-extrinsic defect containing a 2 Al-dopants and an oxygen vacancy behaves as if adsorbed on the clean (101) surface. Again this is valuable result for experimentalists, offering much simpler alternative for removing Ti^{3+} states to methods such as treatment with oxygen plasma[50].

8.4 RT-TDDFT

Electronic excitations and charge transfer are an essential aspect of much of work being done in nanotechnology today, not least DSSCs, with the accurate modelling of them being extremely important in predicting how devices will behave. Casida's linear response forumlation of TDDFT [189, 190] has been widely used, but scales poorly with system size. Therefore the need for other approaches that offer the potential of tackling large, more physically realistic models is apparent. Real time propagation of the time-dependent Kohn-Sham equations (RT-TDDFT), provides an alternative approach to Casida's linear response formalism and offers better scaling for large systems.

We have implemented and tested RT-TDDFT in the $\mathcal{O}$(N) DFT CONQUEST code, propagating not the Kohn-Sham wavefunctions, but working directly with the density matrix. By imposing suitable spatial cut-offs on the density matrix we have illustrated that the computational scaling of our implementation can be made to increase *linearly* with system size. Opening up the possibility of studying the optical properties of large systems, this implementation is of major benefit to those working in the field.

We have applied our method to systems of relevance to DSSCs, studying size effects in TiO_2 clusters, and generating optical absorption spectra for moderately sized dyes. We have concluded that the threshold for QSEs in TiO_2 extends to systems containing as many as ~ 250 atoms. This provides a useful guideline for those wishing to model optical properties of such systems, and serves the size of clusters for which a quantum size effect is observed serves as a useful post-hoc motivation for our excellent scaling RT-TDDFT implementation. Our method is also shown to produce good agreement with experiment for the optical properties of dyes

typically used in DSSCs; the coumarin derivatives C343, NKX-2311 and NKX-2586.

As a final study we have performed calculations on a test system modelling the interaction of C343 coumarin dye with a $(TiO_2)_8$ nanocluster. We find that on adsorption a small peak is introduced in the absorption spectra at lower energy than that of the free dye, and the main peak is red-shifted and broadened, traits that are apparent in the experimental data. Finally we demonstrate the failing of a simple approach for modelling charge injection in DSSC systems, and outline two potential solutions.

Bibliography

[1] W. Chan, G. Cooper, and C. Brion, "Absolute optical oscillator strengths for discrete and continuum photoabsorption of carbon monoxide (7-200 ev) and transition moments for the $x^1\sigma^+ \rightarrow a^1\pi$ system," *Chemical Physics*, vol. 170, no. 1, pp. 123 – 138, 1993.

[2] E. Koch and A. Otto, "Optical absorption of benzene vapour for photon energies from 6 ev to 35 ev," *Chemical Physics Letters*, vol. 12, no. 3, pp. 476 – 480, 1972.

[3] K. Hara, T. Sato, R. Katoh, A. Furube, Y. Ohga, A. Shinpo, S. Suga, K. Sayama, H. Sugihara, and H. Arakawa, "Molecular design of coumarin dyes for efficient dye-sensitized solar cells," *The Journal of Physical Chemistry B*, vol. 107, no. 2, pp. 597–606, 2003.

[4] A. Solga, Z. Cerman, B. F. Striffler, M. Spaeth, and W. Barthlott, "The dream of staying clean: Lotus and biomimetic surfaces," *Bioinspiration & Biomimetics*, vol. 2, no. 4, p. S126, 2007.

[5] R. Blossey, "Self-cleaning surfaces - virtual realities," *Nature Materials*, vol. 2, no. 5, pp. 301 – 306, 2003.

[6] M. Russo, G. Olivieri, A. Marzocchella, P. Salatino, P. Caramuscio, and C. Cavaleiro, "Post-combustion carbon capture mediated by carbonic anhydrase," *Separation and Purification Technology*, no. 0, pp. –, 2012.

[7] A. R. Parker and H. E. Townley, "Biomimetics of photonic nanostructures," *Nature Nanotechnology*, vol. 2, no. 6, pp. 347 – 353, 2007.

[8] Y. Tachibana, L. Vayssieres, and J. R. Durrant, "Artificial photosynthesis for solar water-splitting," *Nature Nanotechnology*, vol. 6, no. 8, pp. 511 – 518, 2012.

[9] Q. Zhang and G. Cao, "Nanostructured photoelectrodes for dye-sensitized solar cells," *Nano Today*, vol. 6, no. 1, pp. 91 – 109, 2011.

[10] A. Yella, H.-W. Lee, H. N. Tsao, C. Yi, A. K. Chandiran, M. Nazeeruddin, E. W.-G. Diau, C.-Y. Yeh, S. M. Zakeeruddin, and M. Grätzel, "Porphyrin-sensitized solar cells with cobalt (ii/iii)-based redox electrolyte exceed 12 percent efficiency," *Science*, vol. 334, no. 6056, pp. 629–634, 2011.

[11] M. K. Nazeeruddin, A. Kay, I. Rodicio, R. Humphry-Baker, E. Mueller, P. Liska, N. Vlachopoulos, and M. Grätzel, "Conversion of light to electricity by cis-x2bis(2,2'-bipyridyl-4,4'-dicarboxylate)ruthenium(ii) charge-transfer sensitizers (x = cl-, br-, i-, cn-, and scn-) on nanocrystalline titanium dioxide electrodes," *Journal of the American Chemical Society*, vol. 115, no. 14, pp. 6382–6390, 1993.

[12] H. Gerischer, M. Michel-Beyerle, F. Rebentrost, and H. Tributsch, "Sensitization of charge injection into semiconductors with large band gap," *Electrochimica Acta*, vol. 13, no. 6, pp. 1509 – 1515, 1968.

[13] B. O. amd Michael Grätzel, "A low-cost, high-efficiency solar cell based on dye-sensitized colloidal tio2 films," *Nature*, vol. 353, no. 8, pp. 737 – 740, 1991.

[14] B. Russo and G. Cao, "Fabrication and characterization of fluorine-doped thin oxide thin films and nanorod arrays via spray pyrolysis," *Applied Physics A: Materials Science & Processing*, vol. 90, pp. 311–315, 2008. 10.1007/s00339-007-4274-4.

[15] M. K. Nazeeruddin, P. Pechy, and M. Grätzel, "Efficient panchromatic sensitization of nanocrystalline tio2 films by a black dye based on a trithiocyanato-ruthenium complex," *Chem. Commun.*, pp. 1705–1706, 1997.

[16] M. K. Nazeeruddin, A. Kay, I. Rodicio, R. Humphry-Baker, E. Mueller, P. Liska, N. Vlachopoulos, and M. Grätzel, "Conversion of light to electricity by cis-x2bis(2,2'-bipyridyl-4,4'-dicarboxylate)ruthenium(ii) charge-transfer sensitizers (x = cl-, br-, i-, cn-, and scn-) on nanocrystalline titanium dioxide electrodes," *Journal of the American Chemical Society*, vol. 115, no. 14, pp. 6382–6390, 1993.

[17] M. K. Nazeeruddin, P. Péchy, T. Renouard, S. M. Zakeeruddin, R. Humphry-Baker, P. Comte, P. Liska, L. Cevey, E. Costa, V. Shklover, L. Spiccia, G. B. Deacon, C. A. Bignozzi, and M. Grätzel, "Engineering of efficient panchromatic sensitizers for nanocrystalline tio2-based solar cells," *Journal of the American Chemical Society*, vol. 123, no. 8, pp. 1613–1624, 2001. PMID: 11456760.

[18] F. Gao, Y. Wang, D. Shi, J. Zhang, M. Wang, X. Jing, R. Humphry-Baker, P. Wang, S. M. Zakeeruddin, and M. Grätzel, "Enhance the optical absorptivity of nanocrystalline tio2 film with high molar extinction coefficient ruthenium sensitizers for high performance dye-sensitized solar cells," *Journal of the American Chemical Society*, vol. 130, no. 32, pp. 10720–10728, 2008.

[19] A. Hagfeldt, G. Boschloo, L. Sun, L. Kloo, and H. Pettersson, "Dye-sensitized solar cells," *Chemical Reviews*, vol. 110, no. 11, pp. 6595–6663, 2010.

[20] A. Listorti, B. O'Regan, and J. R. Durrant, "Electron transfer dynamics in dye-sensitized solar cells," *Chemistry of Materials*, vol. 23, no. 15, pp. 3381–3399, 2011.

[21] S. Ardo and G. J. Meyer, "Photodriven heterogeneous charge transfer with transition-metal compounds anchored to tio2 semiconductor surfaces," *Chem. Soc. Rev.*, vol. 38, pp. 115–164, 2009.

[22] Y. Tachibana, M. Nazeeruddin, M. Gratzel, D. R. Klug, and J. R. Durrant, "Electron injection kinetics for the nanocrystalline tio2 films sensitised with the dye (bu4n)2ru(dcbpyh)2(ncs)2," *Chemical Physics*, vol. 285, no. 1, pp. 127 – 132, 2002. <ce:title>Unconventional Photoactive Systems</ce:title>.

[23] S. A. Haque, E. Palomares, B. M. Cho, A. N. M. Green, N. Hirata, D. R. Klug, and J. R. Durrant, "Charge separation versus recombination in dye-sensitized nanocrystalline solar cells: the minimization of kinetic redundancy," *Journal of the American Chemical Society*, vol. 127, no. 10, pp. 3456–3462, 2005. PMID: 15755165.

[24] G. de Miguel, M. Marchena, M. Ziólek, S. S. Pandey, S. Hayase, and A. Douhal, "Femto- to millisecond photophysical characterization of indole-based squaraines adsorbed on tio2 nanoparticle thin films," *The Journal of Physical Chemistry C*, vol. 116, no. 22, pp. 12137–12148, 2012.

[25] G. de Miguel, M. Ziólek, M. Zitnan, J. A. Organero, S. S. Pandey, S. Hayase, and A. Douhal, "Photophysics of h- and j-aggregates of indole-based squaraines in solid state," *The Journal of Physical Chemistry C*, vol. 116, no. 17, pp. 9379–9389, 2012.

[26] A. Ehret, L. Stuhl, and M. T. Spitler, "Spectral sensitization of tio2 nanocrystalline electrodes with aggregated cyanine dyes," *The Journal of Physical Chemistry B*, vol. 105, no. 41, pp. 9960–9965, 2001.

[27] J. R. Mann, M. K. Gannon, T. C. Fitzgibbons, M. R. Detty, and D. F. Watson, "Optimizing the photocurrent efficiency of dye-sensitized solar cells through the controlled aggregation of chalcogenoxanthylium dyes on nanocrystalline titania films," *The Journal of Physical Chemistry C*, vol. 112, no. 34, pp. 13057–13061, 2008.

[28] H.-P. Lu, C.-Y. Tsai, W.-N. Yen, C.-P. Hsieh, C.-W. Lee, C.-Y. Yeh, and E. W.-G. Diau, "Control of dye aggregation and electron injection for highly efficient porphyrin sensitizers adsorbed on semiconductor films with varying ratios of coadsorbate," *The Journal of Physical Chemistry C*, vol. 113, no. 49, pp. 20990–20997, 2009.

[29] N. R. Neale, N. Kopidakis, J. van de Lagemaat, M. Grätzel, and A. J. Frank, "Effect of a coadsorbent on the performance of dye-sensitized tio2 solar cells: Shielding versus band-edge movement," *The Journal of Physical Chemistry B*, vol. 109, no. 49, pp. 23183–23189, 2005. PMID: 16375281.

[30] J. N. Clifford, E. Martinez-Ferrero, and E. Palomares, "Dye mediated charge recombination dynamics in nanocrystalline tio2 dye sensitized solar cells," *J. Mater. Chem.*, vol. 22, pp. 12415–12422, 2012.

[31] H. Wang, M. Liu, M. Zhang, P. Wang, H. Miura, Y. Cheng, and J. Bell, "Kinetics of electron recombination of dye-sensitized solar cells based on tio2 nanorod arrays sensitized with different dyes," *Phys. Chem. Chem. Phys.*, vol. 13, pp. 17359–17366, 2011.

[32] Y. Yu, K. Wu, and D. Wang, "Dye-sensitized solar cells with modified tio[sub 2] surface chemical states: The role of ti[sup 3 +]," *Applied Physics Letters*, vol. 99, no. 19, p. 192104, 2011.

[33] J. Weidmann, T. Dittrich, E. Konstantinova, I. Lauermann, I. Uhlendorf, and F. Koch, "Influence of oxygen and water related surface defects on the dye sensitized tio2 solar cell," *Solar Energy Materials and Solar Cells*, vol. 56, no. 2, pp. 153 – 165, 1999.

[34] K. H. Ko, Y. C. Lee, and Y. J. Jung, "Enhanced efficiency of dye-sensitized tio2 solar cells (dssc) by doping of metal ions," *Journal of Colloid and Interface Science*, vol. 283, no. 2, pp. 482 – 487, 2005.

[35] Y. Duan, N. Fu, Q. Liu, Y. Fang, X. Zhou, J. Zhang, and Y. Lin, "Sn-doped tio2 photoanode for dye-sensitized solar cells," *The Journal of Physical Chemistry C*, vol. 116, no. 16, pp. 8888–8893, 2012.

[36] F. Gao, Y. Wang, D. Shi, J. Zhang, M. Wang, X. Jing, R. Humphry-Baker, P. Wang, S. M. Zakeeruddin, and M. Grätzel, "Enhance the optical absorptivity of nanocrystalline tio2 film with high molar extinction coefficient ruthenium sensitizers for high performance dye-sensitized solar cells," *Journal of the American Chemical Society*, vol. 130, no. 32, pp. 10720–10728, 2008.

[37] M. K. Nazeeruddin, A. Kay, I. Rodicio, R. Humphry-Baker, E. Mueller, P. Liska, N. Vlachopoulos, and M. Grätzel, "Conversion of light to electricity by cis-x2bis(2,2'-bipyridyl-4,4'-dicarboxylate)ruthenium(ii) charge-transfer sensitizers (x = cl-, br-, i-, cn-, and scn-) on nanocrystalline titanium dioxide electrodes," *Journal of the American Chemical Society*, vol. 115, no. 14, pp. 6382–6390, 1993.

[38] Y. Sun, A. C. Onicha, M. Myahkostupov, and F. N. Castellano, "Viable alternative to n719 for dye-sensitized solar cells," *ACS Applied Materials & Interfaces*, vol. 2, no. 7, pp. 2039–2045, 2010.

[39] S. Ito, S. Zakeeruddin, R. Humphry-Baker, P. Liska, R. Charvet, P. Comte, M. Nazeeruddin, P. PÃ©chy, M. Takata, H. Miura, S. Uchida, and M. Grätzel, "High-efficiency organic-dye- sensitized solar cells controlled by nanocrystalline-tio2 electrode thickness," *Advanced Materials*, vol. 18, no. 9, pp. 1202–1205, 2006.

[40] T. Horiuchi, H. Miura, K. Sumioka, and S. Uchida, "High efficiency of dye-sensitized solar cells based on metal-free indoline dyes," *Journal of the American Chemical Society*, vol. 126, no. 39, pp. 12218–12219, 2004.

[41] J.-H. Yum, P. Walter, S. Huber, D. Rentsch, T. Geiger, F. Nüesch, F. De Angelis, M. Grätzel, and M. K. Nazeeruddin, "Efficient far red sensitization of nanocrystalline tio2 films by an unsymmetrical squaraine dye," *Journal of the American Chemical Society*, vol. 129, no. 34, pp. 10320–10321, 2007.

[42] Y. Ooyama, N. Yamaguchi, I. Imae, K. Komaguchi, J. Ohshita, and Y. Harima, "Dye-sensitized solar cells based on d-[small pi]-a fluorescent dyes with two pyridyl groups as an electron-withdrawing-injecting anchoring group," *Chem. Commun.*, vol. 49, pp. 2548–2550, 2013.

[43] A. Dualeh, F. De Angelis, S. Fantacci, T. Moehl, C. Yi, F. Kessler, E. Baranoff, M. K. Nazeeruddin, and M. Grätzel, "Influence of donor groups of organic d-pi-a dyes on open-circuit voltage in solid-state dye-sensitized solar cells," *The Journal of Physical Chemistry C*, vol. 116, no. 1, pp. 1572–1578, 2012.

[44] S. Kim, J. K. Lee, S. O. Kang, J. Ko, J.-H. Yum, S. Fantacci, F. De Angelis, D. Di Censo, M. K. Nazeeruddin, and M. Grätzel, "Molecular engineering of organic sensitizers for solar cell applications," *Journal of the American Chemical Society*, vol. 128, no. 51, pp. 16701–16707, 2006.

[45] S. Kang, S.-H. Choi, M.-S. Kang, J.-Y. Kim, H.-S. Kim, T. Hyeon, and Y.-E. Sung, "Nanorod-based dye-sensitized solar cells with improved charge collection efficiency," *Advanced Materials*, vol. 20, no. 1, pp. 54–58, 2008.

[46] Y. H. Jung, K.-H. Park, J. S. Oh, D.-H. Kim, and C. K. Hong, "Effect of tio2 rutile nanorods on the photoelectrodes of dye-sensitized solar cells," *Nanoscale Research Letters*, vol. 8, no. 1, p. 37, 2013.

[47] W.-Q. Wu, H.-S. Rao, Y.-F. Xu, Y.-F. Wang, C.-Y. Su, and D.-B. Kuang, "Hierarchical oriented anatase tio2 nanostructure arrays on flexible substrate for efficient dye-sensitized solar cells," *Sci. Rep.*, vol. 3, 2013.

[48] E. Enache-Pommer, J. E. Boercker, and E. S. Aydil, "Electron transport and recombination in polycrystalline tio[sub 2] nanowire dye-sensitized solar cells," *Applied Physics Letters*, vol. 91, no. 12, p. 123116, 2007.

[49] K. H. Ko, Y. C. Lee, and Y. J. Jung, "Enhanced efficiency of dye-sensitized tio2 solar cells (dssc) by doping of metal ions," *Journal of Colloid and Interface Science*, vol. 283, no. 2, pp. 482 – 487, 2005.

[50] Y. Kim, B. J. Yoo, R. Vittal, Y. Lee, N.-G. Park, and K.-J. Kim, "Low-temperature oxygen plasma treatment of tio2 film for enhanced performance of dye-sensitized solar cells," *Journal of Power Sources*, vol. 175, no. 2, pp. 914 – 919, 2008.

[51] P. A. M. Dirac, "Quantum mechanics of many-electron systems," *Proceedings of the Royal Society of London. Series A*, vol. 123, no. 792, pp. 714–733, 1929.

[52] P. Hohenberg and W. Kohn, "Inhomogeneous electron gas," *Phys. Rev.*, vol. 136, pp. B864–B871, Nov 1964.

[53] W. Kohn and L. J. Sham, "Self-consistent equations including exchange and correlation effects," *Phys. Rev.*, vol. 140, pp. A1133–A1138, Nov 1965.

[54] P. A. M. Dirac, "On the annihilation of electrons and protons," *Mathematical Proceedings of the Cambridge Philosophical Society*, vol. 26, pp. 361–375, 6 1930.

[55] D. M. Ceperley and B. J. Alder, "Ground state of the electron gas by a stochastic method," *Phys. Rev. Lett.*, vol. 45, pp. 566–569, Aug 1980.

[56] J. P. Perdew, J. A. Chevary, S. H. Vosko, K. A. Jackson, M. R. Pederson, D. J. Singh, and C. Fiolhais, "Atoms, molecules, solids, and surfaces: Applications of the generalized gradient approximation for exchange and correlation," *Phys. Rev. B*, vol. 46, pp. 6671–6687, Sep 1992.

[57] G. Ortiz and P. Ballone, "Pseudopotentials for non-local-density functionals," *Phys. Rev. B*, vol. 43, pp. 6376–6387, Mar 1991.

[58] J. P. Perdew, K. Burke, and M. Ernzerhof, "Generalized gradient approximation made simple," *Phys. Rev. Lett.*, vol. 77, pp. 3865–3868, Oct 1996.

[59] J. P. Perdew and A. Zunger, "Self-interaction correction to density-functional approximations for many-electron systems," *Phys. Rev. B*, vol. 23, pp. 5048–5079, May 1981.

[60] S. L. Dudarev, G. A. Botton, S. Y. Savrasov, C. J. Humphreys, and A. P. Sutton, "Electron-energy-loss spectra and the structural stability of nickel oxide: an lsda+u study," *Phys. Rev. B*, vol. 57, pp. 1505–1509, Jan 1998.

[61] V. I. Anisimov, F. Aryasetiawan, and A. I. Lichtenstein, "First-principles calculations of the electronic structure and spectra of strongly correlated systems: the lda + u method," *Journal of Physics: Condensed Matter*, vol. 9, no. 4, p. 767, 1997.

[62] A. D. Becke, "A new mixing of hartree–fock and local density-functional theories," *The Journal of Chemical Physics*, vol. 98, no. 2, pp. 1372–1377, 1993.

[63] A. D. Becke, "Density-functional thermochemistry. iii. the role of exact exchange," *The Journal of Chemical Physics*, vol. 98, no. 7, pp. 5648–5652, 1993.

[64] C. Lee, W. Yang, and R. G. Parr, "Development of the colle-salvetti correlation-energy formula into a functional of the electron density," *Phys. Rev. B*, vol. 37, pp. 785–789, Jan 1988.

[65] N. Ashcroft and N. Mermin, *Solid state physics*. Science: Physics, Saunders College, 1976.

[66] H. J. Monkhorst and J. D. Pack, "Special points for brillouin-zone integrations," *Phys. Rev. B*, vol. 13, pp. 5188–5192, Jun 1976.

[67] G. P. Francis and M. C. Payne, "Finite basis set corrections to total energy pseudopotential calculations," *Journal of Physics: Condensed Matter*, vol. 2, no. 19, p. 4395, 1990.

[68] D. Vanderbilt, "Soft self-consistent pseudopotentials in a generalized eigenvalue formalism," *Phys. Rev. B*, vol. 41, pp. 7892–7895, Apr 1990.

[69] A. L. Linsebigler, G. Lu, and J. T. Yates, "Photocatalysis on tio2 surfaces: Principles, mechanisms, and selected results," *Chemical Reviews*, vol. 95, no. 3, pp. 735–758, 1995.

[70] K. Nakata and A. Fujishima, "Tio2 photocatalysis: Design and applications," *Journal of Photochemistry and Photobiology C: Photochemistry Reviews*, vol. 13, no. 3, pp. 169 – 189, 2012.

[71] D. L. Wang, S. S. Watson, L.-P. Sung, I.-H. Tseng, C. J. Bouis, and R. Fernando, "Effect of tio2 pigment type on the uv degradation of filled coatings," *Journal of Coatings Technology and Research*, vol. 8, no. 1, pp. 19–33, 2011.

[72] P.-C. Maness, S. Smolinski, D. M. Blake, Z. Huang, E. J. Wolfrum, and W. A. Jacoby, "Bactericidal activity of photocatalytic tio2 reaction: toward an understanding of its killing mechanism," *Applied and environmental microbiology*, vol. 65, no. 9, pp. 4094–4098, 1999.

[73] A. Mills, R. H. Davies, and D. Worsley, "Water purification by semiconductor photocatalysis," *Chem. Soc. Rev.*, vol. 22, pp. 417–425, 1993.

[74] U. Diebold, "The surface science of titanium dioxide," *Surface Science Reports*, vol. 48, no. 5-8, pp. 53–229, 2003.

[75] A. Listorti, B. O'Regan, and J. R. Durrant, "Electron transfer dynamics in dye-sensitized solar cells," *Chemistry of Materials*, vol. 23, no. 15, pp. 3381–3399, 2011.

[76] M. K. Nazeeruddin, P. Pechy, and M. Grätzel, "Efficient panchromatic sensitization of nanocrystalline tio2 films by a black dye based on a trithiocyanato-ruthenium complex," *Chem. Commun.*, pp. 1705–1706, 1997.

[77] M. K. Nazeeruddin, P. Péchy, T. Renouard, S. M. Zakeeruddin, R. Humphry-Baker, P. Comte, P. Liska, L. Cevey, E. Costa, V. Shklover, L. Spiccia, G. B. Deacon, C. A. Bignozzi, and M. Grätzel, "Engineering of efficient panchromatic sensitizers for nanocrys-

talline tio2-based solar cells," *Journal of the American Chemical Society*, vol. 123, no. 8, pp. 1613–1624, 2001. PMID: 11456760.

[78] M. K. Nazeeruddin, A. Kay, I. Rodicio, R. Humphry-Baker, E. Mueller, P. Liska, N. Vlachopoulos, and M. Grätzel, "Conversion of light to electricity by cis-x2bis(2,2'-bipyridyl-4,4'-dicarboxylate)ruthenium(ii) charge-transfer sensitizers (x = cl-, br-, i-, cn-, and scn-) on nanocrystalline titanium dioxide electrodes," *Journal of the American Chemical Society*, vol. 115, no. 14, pp. 6382–6390, 1993.

[79] H. Zhang and J. F. Banfield, "Thermodynamic analysis of phase stability of nanocrystalline titania," *J. Mater. Chem.*, vol. 8, pp. 2073–2076, 1998.

[80] M. Lazzeri, A. Vittadini, and A. Selloni, "Structure and energetics of stoichiometric $\mathrm{tio_2}$ anatase surfaces," *Phys. Rev. B*, vol. 63, p. 155409, Mar 2001.

[81] A. Vittadini, A. Selloni, F. P. Rotzinger, and M. Grätzel, "Formic acid adsorption on dry and hydrated tio2 anatase (101) surfaces by dft calculations," *The Journal of Physical Chemistry B*, vol. 104, no. 6, pp. 1300–1306, 2000.

[82] M. Xu, H. Noei, M. Buchholz, M. Muhler, C. WÃ¶ll, and Y. Wang, "Dissociation of formic acid on anatase tio2(101) probed by vibrational spectroscopy," *Catalysis Today*, vol. 182, no. 1, pp. 12 – 15, 2012.

[83] S. M. Zakeeruddin, M. K. Nazeeruddin, P. Pechy, F. P. Rotzinger, R. Humphry-Baker, K. Kalyanasundaram, M. Grätzel, V. Shklover, and T. Haibach, "Molecular engineering of photosensitizers for nanocrystalline solar cells: Synthesis and characterization of ru dyes based on phosphonated terpyridines," *Inorganic Chemistry*, vol. 36, no. 25, pp. 5937–5946, 1997.

[84] P. Pechy, F. P. Rotzinger, M. K. Nazeeruddin, O. Kohle, S. M. Zakeeruddin, R. Humphry-Baker, and M. Gratzel, "Preparation of phosphonated polypyridyl ligands to anchor transition-metal complexes on oxide surfaces: application for the conversion of light to electricity with nanocrystalline tio2 films," *J. Chem. Soc., Chem. Commun.*, vol. 0, pp. 65–66, 1995.

[85] S. Altobello, C. Bignozzi, S. Caramori, G. Larramona, S. Quici, G. Marzanni, and R. Lakhmiri, "Sensitization of tio2 with ruthenium complexes containing boronic acid functions," *Journal of Photochemistry and Photobiology A: Chemistry*, vol. 166, no. 1-3, pp. 91 – 98, 2004.

[86] M. Katono, T. Bessho, S. Meng, R. Humphry-Baker, G. Rothenberger, S. M. Zakeeruddin, E. Kaxiras, and M. Grätzel, "D-π-a dye system containing cyano-benzoic acid as anchoring group for dye-sensitized solar cells," *Langmuir*, vol. 27, no. 23, pp. 14248–14252, 2011.

[87] M. Nilsing, P. Persson, S. Lunell, and L. Ojamäe, "Dye-sensitization of the tio2 rutile (110) surface by perylene dyes: Quantum-chemical periodic b3lyp computations," *The Journal of Physical Chemistry C*, vol. 111, no. 32, pp. 12116–12123, 2007.

[88] V. Thavasi, V. Renugopalakrishnan, R. Jose, and S. Ramakrishna, "Controlled electron injection and transport at materials interfaces in dye sensitized solar cells," *Materials Science and Engineering: R: Reports*, vol. 63, no. 3, pp. 81 – 99, 2009.

[89] M. Lv, D. Zheng, M. Ye, L. Sun, J. Xiao, W. Guo, and C. Lin, "Densely aligned rutile tio2 nanorod arrays with high surface area for efficient dye-sensitized solar cells," *Nanoscale*, vol. 4, pp. 5872–5879, 2012.

[90] M. Lv, D. Zheng, M. Ye, J. Xiao, W. Guo, Y. Lai, L. Sun, C. Lin, and J. Zuo, "Optimized porous rutile tio2 nanorod arrays for enhancing the efficiency of dye-sensitized solar cells," *Energy Environ. Sci.*, vol. 6, pp. 1615–1622, 2013.

[91] B. Laskova, M. Zukalova, L. Kavan, A. Chou, P. Liska, Z. Wei, L. Bin, P. Kubat, E. Ghadiri, J. Moser, and M. Grätzel, "Voltage enhancement in dye-sensitized solar cell using (001)-oriented anatase tio2 nanosheets," *Journal of Solid State Electrochemistry*, vol. 16, no. 9, pp. 2993–3001, 2012.

[92] H. Zhang, Y. Han, X. Liu, P. Liu, H. Yu, S. Zhang, X. Yao, and H. Zhao, "Anatase tio2 microspheres with exposed mirror-like plane 001 facets for high performance dye-sensitized solar cells (dsscs)," *Chem. Commun.*, vol. 46, pp. 8395–8397, 2010.

[93] J. Yu, J. Fan, and K. Lv, "Anatase tio2 nanosheets with exposed (001) facets: improved photoelectric conversion efficiency in dye-sensitized solar cells," *Nanoscale*, vol. 2, pp. 2144–2149, 2010.

[94] G. Kresse and J. Furthmüller, "Efficiency of ab-initio total energy calculations for metals and semiconductors using a plane-wave basis set," *Computational Materials Science*, vol. 6, no. 1, pp. 15 – 50, 1996.

[95] J. P. Perdew, J. A. Chevary, S. H. Vosko, K. A. Jackson, M. R. Pederson, D. J. Singh, and C. Fiolhais, "Atoms, molecules, solids, and surfaces: Applications of the generalized

gradient approximation for exchange and correlation," *Phys. Rev. B*, vol. 46, pp. 6671–6687, Sep 1992.

[96] D. Vanderbilt, "Soft self-consistent pseudopotentials in a generalized eigenvalue formalism," *Phys. Rev. B*, vol. 41, pp. 7892–7895, Apr 1990.

[97] P. Pulay, "Convergence acceleration of iterative sequences. the case of scf iteration," *Chemical Physics Letters*, vol. 73, no. 2, pp. 393 – 398, 1980.

[98] J. K. Burdett, T. Hughbanks, G. J. Miller, J. W. Richardson, and J. V. Smith, "Structural-electronic relationships in inorganic solids: powder neutron diffraction studies of the rutile and anatase polymorphs of titanium dioxide at 15 and 295 k," *Journal of the American Chemical Society*, vol. 109, no. 12, pp. 3639–3646, 1987.

[99] R. Colle and O. Salvetti, "A general method for approximating the electronic correlation energy in molecules and solids," *The Journal of Chemical Physics*, vol. 79, no. 3, pp. 1404–1407, 1983.

[100] X.-Q. Gong, A. Selloni, and A. Vittadini, "Density functional theory study of formic acid adsorption on anatase tio2(001): Geometries, energetics, and effects of coverage, hydration, and reconstruction," *The Journal of Physical Chemistry B*, vol. 110, no. 6, pp. 2804–2811, 2006. PMID: 16471889.

[101] X.-Q. Gong and A. Selloni, "Reactivity of anatase tio2 nanoparticles: The role of the minority (001) surface," *The Journal of Physical Chemistry B*, vol. 109, no. 42, pp. 19560–19562, 2005. PMID: 16853530.

[102] T. Ohno, K. Sarukawa, and M. Matsumura, "Crystal faces of rutile and anatase tio2 particles and their roles in photocatalytic reactions," *New J. Chem.*, vol. 26, pp. 1167–1170, 2002.

[103] H. Yu, B. Tian, and J. Zhang, "Layered tio2 composed of anatase nanosheets with exposed 001 facets: Facile synthesis and enhanced photocatalytic activity," *Chemistry - A European Journal*, vol. 17, no. 20, pp. 5499–5502, 2011.

[104] L. Sun, Z. Zhao, Y. Zhou, and L. Liu, "Anatase tio2 nanocrystals with exposed 001 facets on graphene sheets via molecular grafting for enhanced photocatalytic activity," *Nanoscale*, vol. 4, pp. 613–620, 2012.

[105] J. Yu, J. Fan, and K. Lv, "Anatase tio2 nanosheets with exposed (001) facets: improved photoelectric conversion efficiency in dye-sensitized solar cells," *Nanoscale*, vol. 2, pp. 2144–2149, 2010.

[106] X. Wu, Z. Chen, G. Q. M. Lu, and L. Wang, "Nanosized anatase tio2 single crystals with tunable exposed (001) facets for enhanced energy conversion efficiency of dye-sensitized solar cells," *Advanced Functional Materials*, vol. 21, no. 21, pp. 4167–4172, 2011.

[107] J. Zhang, J. Wang, Z. Zhao, T. Yu, J. Feng, Y. Yuan, Z. Tang, Y. Liu, Z. Li, and Z. Zou, "Reconstruction of the (001) surface of tio2 nanosheets induced by the fluorine-surfactant removal process under uv-irradiation for dye-sensitized solar cells," *Phys. Chem. Chem. Phys.*, vol. 14, pp. 4763–4769, 2012.

[108] W. Guo, C. Xu, X. Wang, S. Wang, C. Pan, C. Lin, and Z. L. Wang, "Rectangular bunched rutile tio2 nanorod arrays grown on carbon fiber for dye-sensitized solar cells," *Journal of the American Chemical Society*, vol. 134, no. 9, pp. 4437–4441, 2012.

[109] R. Lindsay, A. Wander, A. Ernst, B. Montanari, G. Thornton, and N. M. Harrison, "Revisiting the surface structure of $\mathrm{tio}_2(110)$: A quantitative low-energy electron diffraction study," *Phys. Rev. Lett.*, vol. 94, p. 246102, Jun 2005.

[110] H. Onishi and Y. Iwasawa, "Reconstruction of tio2(110) surface: Stm study with atomic-scale resolution," *Surface Science*, vol. 313, no. 1-2, pp. L783 – L789, 1994.

[111] F. Nunzi and F. De Angelis, "Dft investigations of formic acid adsorption on single-wall tio2 nanotubes: Effect of the surface curvature," *The Journal of Physical Chemistry C*, vol. 115, no. 5, pp. 2179–2186, 2011.

[112] X.-Q. Gong, A. Selloni, and A. Vittadini, "Density functional theory study of formic acid adsorption on anatase tio2(001): Geometries, energetics, and effects of coverage, hydration, and reconstruction," *The Journal of Physical Chemistry B*, vol. 110, no. 6, pp. 2804–2811, 2006. PMID: 16471889.

[113] S. Bates, G. Kresse, and M. Gillan, "The adsorption and dissociation of roh molecules on tio2(110)," *Surface Science*, vol. 409, no. 2, pp. 336 – 349, 1998.

[114] R. Luschtinetz, J. Frenzel, T. Milek, and G. Seifert, "Adsorption of phosphonic acid at the tio2 anatase (101) and rutile (110) surfaces," *The Journal of Physical Chemistry C*, vol. 113, no. 14, pp. 5730–5740, 2009.

[115] M. Nilsing, S. Lunell, P. Persson, and L. Ojamäe, "Phosphonic acid adsorption at the tio2 anatase (101) surface investigated by periodic hybrid hf-dft computations," *Surface Science*, vol. 582, no. 1-3, pp. 49 – 60, 2005.

[116] G. Popova, T. Andrushkevich, Y. Chesalov, and E. Stoyanov, "In situ ftir study of the adsorption of formaldehyde, formic acid, and methyl formiate at the surface of tio2 (anatase)," *Kinetics and Catalysis*, vol. 41, no. 6, pp. 805–811, 2000.

[117] P. Käckell and K. Terakura, "Dissociative adsorption of formic acid and diffusion of formate on the tio2(110) surface: the role of hydrogen," *Surface Science*, vol. 461, no. 1-3, pp. 191 – 198, 2000.

[118] F. P. Rotzinger, J. M. Kesselman-Truttmann, S. J. Hug, V. Shklover, and M. Grätzel, "Structure and vibrational spectrum of formate and acetate adsorbed from aqueous solution onto the tio2 rutile (110) surface," *The Journal of Physical Chemistry B*, vol. 108, no. 16, pp. 5004–5017, 2004.

[119] G. S. Herman, M. R. Sievers, and Y. Gao, "Structure determination of the two-domain (1×4) anatase $\mathrm{tio}_2(001)$ surface," *Phys. Rev. Lett.*, vol. 84, pp. 3354–3357, Apr 2000.

[120] H. G. Yang, C. H. Sun, S. Z. Qiao, G. Zou, Jinand Liu, S. C. Smith, H. M. Cheng, and G. Q. Lu, "Anatase tio2 single crystals with a large percentage of reactive facets," *Nature*, vol. 453, pp. 638–641, 2007.

[121] S. Selcuk and A. Selloni, "Surface structure and reactivity of anatase tio2 crystals with dominant 001 facets," *The Journal of Physical Chemistry C*, vol. 117, no. 12, pp. 6358–6362, 2013.

[122] B. O. amd Michael Grätzel, "A low-cost, high-efficiency solar cell based on dye-sensitized colloidal tio2 films," *Nature*, vol. 353, no. 8, pp. 737 – 740, 1991.

[123] M. K. Nazeeruddin, A. Kay, I. Rodicio, R. Humphry-Baker, E. Mueller, P. Liska, N. Vlachopoulos, and M. Graetzel, "Conversion of light to electricity by cis-x2bis(2,2'-bipyridyl-4,4'-dicarboxylate)ruthenium(ii) charge-transfer sensitizers (x = cl-, br-, i-, cn-, and scn-) on nanocrystalline titanium dioxide electrodes," *Journal of the American Chemical Society*, vol. 115, no. 14, pp. 6382–6390, 1993.

[124] M. K. Nazeeruddin, F. De Angelis, S. Fantacci, A. Selloni, G. Viscardi, P. Liska, S. Ito, B. Takeru, and M. Grätzel, "Combined experimental and dft-tddft computational study

of photoelectrochemical cell ruthenium sensitizers," *Journal of the American Chemical Society*, vol. 127, no. 48, pp. 16835–16847, 2005.

[125] H. Ozawa, R. Shimizu, and H. Arakawa, "Significant improvement in the conversion efficiency of black-dye-based dye-sensitized solar cells by cosensitization with organic dye," *RSC Adv.*, vol. 2, pp. 3198–3200, 2012.

[126] R. Y. Ogura, S. Nakane, M. Morooka, M. Orihashi, Y. Suzuki, and K. Noda, "High-performance dye-sensitized solar cell with a multiple dye system," *Applied Physics Letters*, vol. 94, no. 7, p. 073308, 2009.

[127] Z.-S. Wang, Y. Cui, Y. Dan-oh, C. Kasada, A. Shinpo, and K. Hara, "Molecular design of coumarin dyes for stable and efficient organic dye-sensitized solar cells," *The Journal of Physical Chemistry C*, vol. 112, no. 43, pp. 17011–17017, 2008.

[128] K. Hara, Z.-S. Wang, T. Sato, A. Furube, R. Katoh, H. Sugihara, Y. Dan-oh, C. Kasada, A. Shinpo, and S. Suga, "Oligothiophene-containing coumarin dyes for efficient dye-sensitized solar cells," *The Journal of Physical Chemistry B*, vol. 109, no. 32, pp. 15476–15482, 2005.

[129] A. C. Khazraji, S. Hotchandani, S. Das, and P. V. Kamat, "Controlling dye (merocyanine-540) aggregation on nanostructured tio2 films. an organized assembly approach for enhancing the efficiency of photosensitization," *The Journal of Physical Chemistry B*, vol. 103, no. 22, pp. 4693–4700, 1999.

[130] K. Sayama, K. Hara, N. Mori, M. Satsuki, S. Suga, S. Tsukagoshi, Y. Abe, H. Sugihara, and H. Arakawa, "Photosensitization of a porous tio electrode with merocyanine dyes containing a carboxyl group and a long alkyl chain," *Chem. Commun.*, pp. 1173–1174, 2000.

[131] H. Qin, S. Wenger, M. Xu, F. Gao, X. Jing, P. Wang, S. M. Zakeeruddin, and M. Grätzel, "An organic sensitizer with a fused dithienothiophene unit for efficient and stable dye-sensitized solar cells," *Journal of the American Chemical Society*, vol. 130, no. 29, pp. 9202–9203, 2008. PMID: 18582041.

[132] X. Jiang, T. Marinado, E. Gabrielsson, D. P. Hagberg, L. Sun, and A. Hagfeldt, "Structural modification of organic dyes for efficient coadsorbent-free dye-sensitized solar cells," *The Journal of Physical Chemistry C*, vol. 114, no. 6, pp. 2799–2805, 2010.

[133] R. Chen, X. Yang, H. Tian, X. Wang, A. Hagfeldt, and L. Sun, "Effect of tetrahydroquinoline dyes structure on the performance of organic dye-sensitized solar cells," *Chemistry of Materials*, vol. 19, no. 16, pp. 4007–4015, 2007.

[134] N. Koumura, Z.-S. Wang, S. Mori, M. Miyashita, E. Suzuki, and K. Hara, "Alkyl-functionalized organic dyes for efficient molecular photovoltaics," *Journal of the American Chemical Society*, vol. 128, no. 44, pp. 14256–14257, 2006.

[135] D. Kim, J. K. Lee, S. O. Kang, and J. Ko, "Molecular engineering of organic dyes containing n-aryl carbazole moiety for solar cell," *Tetrahedron*, vol. 63, no. 9, pp. 1913 – 1922, 2007.

[136] S. Ito, H. Miura, S. Uchida, M. Takata, K. Sumioka, P. Liska, P. Comte, P. Pechy, and M. Gratzel, "High-conversion-efficiency organic dye-sensitized solar cells with a novel indoline dye," *Chem. Commun.*, pp. 5194–5196, 2008.

[137] M. K. Nazeeruddin, P. Pechy, and M. Gratzel, "Efficient panchromatic sensitization of nanocrystalline tio2 films by a black dye based on a trithiocyanato-ruthenium complex," *Chem. Commun.*, pp. 1705–1706, 1997.

[138] G. Benkö, J. Kallioinen, J. E. I. Korppi-Tommola, A. P. Yartsev, and V. SundstrÃ¶m, "Photoinduced ultrafast dye-to-semiconductor electron injection from nonthermalized and thermalized donor states," *Journal of the American Chemical Society*, vol. 124, no. 3, pp. 489–493, 2002. PMID: 11792221.

[139] R. Chen, X. Yang, H. Tian, and L. Sun, "Tetrahydroquinoline dyes with different spacers for organic dye-sensitized solar cells," *Journal of Photochemistry and Photobiology A: Chemistry*, vol. 189, no. 2-3, pp. 295 – 300, 2007.

[140] K. Hara, M. Kurashige, Y. Dan-oh, C. Kasada, A. Shinpo, S. Suga, K. Sayama, and H. Arakawa, "Design of new coumarin dyes having thiophene moieties for highly efficient organic-dye-sensitized solar cells," *New J. Chem.*, vol. 27, pp. 783–785, 2003.

[141] Z.-S. Wang, Y. Cui, Y. Dan-oh, C. Kasada, A. Shinpo, and K. Hara, "Thiophene-functionalized coumarin dye for efficient dye-sensitized solar cells: Electron lifetime improved by coadsorption of deoxycholic acid," *The Journal of Physical Chemistry C*, vol. 111, no. 19, pp. 7224–7230, 2007.

[142] Z.-S. Wang, K. Hara, Y. Dan-oh, C. Kasada, A. Shinpo, S. Suga, H. Arakawa, and H. Sugihara, "Photophysical and (photo)electrochemical properties of a coumarin dye," *The Journal of Physical Chemistry B*, vol. 109, no. 9, pp. 3907–3914, 2005.

[143] G. Kresse and J. Furthmüller, "Efficiency of ab-initio total energy calculations for metals and semiconductors using a plane-wave basis set," *Computational Materials Science*, vol. 6, no. 1, pp. 15 – 50, 1996.

[144] J. P. Perdew, J. A. Chevary, S. H. Vosko, K. A. Jackson, M. R. Pederson, D. J. Singh, and C. Fiolhais, "Atoms, molecules, solids, and surfaces: Applications of the generalized gradient approximation for exchange and correlation," *Phys. Rev. B*, vol. 46, pp. 6671–6687, Sep 1992.

[145] D. Vanderbilt, "Soft self-consistent pseudopotentials in a generalized eigenvalue formalism," *Phys. Rev. B*, vol. 41, pp. 7892–7895, Apr 1990.

[146] P. Pulay, "Convergence acceleration of iterative sequences. the case of scf iteration," *Chemical Physics Letters*, vol. 73, no. 2, pp. 393 – 398, 1980.

[147] S. KristyÃ¡n and P. Pulay, "Can (semi)local density functional theory account for the london dispersion forces?," *Chemical Physics Letters*, vol. 229, no. 3, pp. 175 – 180, 1994.

[148] M. Dion, H. Rydberg, E. Schröder, D. C. Langreth, and B. I. Lundqvist, "Van der waals density functional for general geometries," *Phys. Rev. Lett.*, vol. 92, p. 246401, Jun 2004.

[149] M. Dion, H. Rydberg, E. Schröder, D. C. Langreth, and B. I. Lundqvist, "Erratum: Van der waals density functional for general geometries [phys. rev. lett. 92, 246401 (2004)]," *Phys. Rev. Lett.*, vol. 95, p. 109902, Sep 2005.

[150] T. Thonhauser, V. R. Cooper, S. Li, A. Puzder, P. Hyldgaard, and D. C. Langreth, "Van der waals density functional: Self-consistent potential and the nature of the van der waals bond," *Phys. Rev. B*, vol. 76, p. 125112, Sep 2007.

[151] D. C. Langreth, B. I. Lundqvist, S. D. Chakarova-Käck, V. R. Cooper, M. Dion, P. Hyldgaard, A. Kelkkanen, J. Kleis, L. Kong, S. Li, P. G. Moses, E. Murray, A. Puzder, H. Rydberg, E. Schriöder, and T. Thonhauser, "A density functional for sparse matter," *Journal of Physics: Condensed Matter*, vol. 21, no. 8, p. 084203, 2009.

[152] P. Lazić, N. Atodiresei, M. Alaei, V. Caciuc, S. BlÃ$\frac{1}{4}$gel, and R. Brako, "Junolo - jülich nonlocal code for parallel post-processing evaluation of vdw-df correlation energy," *Computer Physics Communications*, vol. 181, no. 2, pp. 371 – 379, 2010.

[153] K. Hara, T. Sato, R. Katoh, A. Furube, T. Yoshihara, M. Murai, M. Kurashige, S. Ito, A. Shinpo, S. Suga, and H. Arakawa, "Novel conjugated organic dyes for efficient dye-sensitized solar cells," *Advanced Functional Materials*, vol. 15, no. 2, pp. 246–252, 2005.

[154] M. K. Nazeeruddin, R. Humphry-Baker, P. Liska, and M. Grätzel, "Investigation of sensitizer adsorption and the influence of protons on current and voltage of a dye-sensitized nanocrystalline tio2 solar cell," *The Journal of Physical Chemistry B*, vol. 107, no. 34, pp. 8981–8987, 2003.

[155] F. De Angelis, S. Fantacci, A. Selloni, M. Griätzel, and M. K. Nazeeruddin, "Influence of the sensitizer adsorption mode on the open-circuit potential of dye-sensitized solar cells," *Nano Letters*, vol. 7, no. 10, pp. 3189–3195, 2007.

[156] S. Livraghi, M. C. Paganini, E. Giamello, A. Selloni, C. Di Valentin, and G. Pacchioni, "Origin of photoactivity of nitrogen-doped titanium dioxide under visible light," *Journal of the American Chemical Society*, vol. 128, no. 49, pp. 15666–15671, 2006.

[157] C. Di Valentin, G. Pacchioni, A. Selloni, S. Livraghi, and E. Giamello, "Characterization of paramagnetic species in n-doped tio2 powders by epr spectroscopy and dft calculations," *The Journal of Physical Chemistry B*, vol. 109, no. 23, pp. 11414–11419, 2005.

[158] R. Asahi, T. Morikawa, T. Ohwaki, K. Aoki, and Y. Taga, "Visible-light photocatalysis in nitrogen-doped titanium oxides," *Science*, vol. 293, no. 5528, pp. 269–271, 2001.

[159] M. A. Henderson, "Evidence for bicarbonate formation on vacuum annealed tio2(110) resulting from a precursor-mediated interaction between co2 and h2o," *Surface Science*, vol. 400, no. 1-3, pp. 203 – 219, 1998.

[160] U. Terranova and D. R. Bowler, "Effect of hydration of the tio2 anatase (101) substrate on the atomic layer deposition of alumina films," *J. Mater. Chem.*, vol. 21, pp. 4197–4203, 2011.

[161] I. Nakamura, N. Negishi, S. Kutsuna, T. Ihara, S. Sugihara, and K. Takeuchi, "Role of oxygen vacancy in the plasma-treated tio2 photocatalyst with visible light activity for

no removal," *Journal of Molecular Catalysis A: Chemical*, vol. 161, no. 1-2, pp. 205 – 212, 2000.

[162] Z. Lin, A. Orlov, R. M. Lambert, and M. C. Payne, "New insights into the origin of visible light photocatalytic activity of nitrogen-doped and oxygen-deficient anatase tio2," *The Journal of Physical Chemistry B*, vol. 109, no. 44, pp. 20948–20952, 2005.

[163] J. Weidmann, T. Dittrich, E. Konstantinova, I. Lauermann, I. Uhlendorf, and F. Koch, "Influence of oxygen and water related surface defects on the dye sensitized tio2 solar cell," *Solar Energy Materials and Solar Cells*, vol. 56, no. 2, pp. 153 – 165, 1998.

[164] A. Iwaszuk and M. Nolan, "Charge compensation in trivalent cation doped bulk rutile tio 2," *Journal of Physics: Condensed Matter*, vol. 23, no. 33, p. 334207, 2011.

[165] R. Shirley, M. Kraft, and O. R. Inderwildi, "Electronic and optical properties of aluminium-doped anatase and rutile tio_2 from ab initio calculations," *Phys. Rev. B*, vol. 81, p. 075111, Feb 2010.

[166] M. Steveson, T. Bredow, and A. R. Gerson, "Msindo quantum chemical modelling study of the structure of aluminium-doped anatase and rutile titanium dioxide," *Phys. Chem. Chem. Phys.*, vol. 4, pp. 358–365, 2002.

[167] H. Cheng and A. Selloni, "Surface and subsurface oxygen vacancies in anatase tio_2 and differences with rutile," *Phys. Rev. B*, vol. 79, p. 092101, Mar 2009.

[168] Y. He, O. Dulub, H. Cheng, A. Selloni, and U. Diebold, "Evidence for the predominance of subsurface defects on reduced anatase $tio_2(101)$," *Phys. Rev. Lett.*, vol. 102, p. 106105, Mar 2009.

[169] P. Scheiber, M. Fidler, O. Dulub, M. Schmid, U. Diebold, W. Hou, U. Aschauer, and A. Selloni, "(sub)surface mobility of oxygen vacancies at the $\mathrm{tio_2}$ anatase (101) surface," *Phys. Rev. Lett.*, vol. 109, p. 136103, Sep 2012.

[170] H. Zhang and J. F. Banfield, "Thermodynamic analysis of phase stability of nanocrystalline titania," *J. Mater. Chem.*, vol. 8, pp. 2073–2076, 1998.

[171] J. P. Perdew, J. A. Chevary, S. H. Vosko, K. A. Jackson, M. R. Pederson, D. J. Singh, and C. Fiolhais, "Atoms, molecules, solids, and surfaces: Applications of the generalized gradient approximation for exchange and correlation," *Phys. Rev. B*, vol. 46, pp. 6671–6687, Sep 1992.

[172] E. Finazzi, C. D. Valentin, G. Pacchioni, and A. Selloni, "Excess electron states in reduced bulk anatase tio[sub 2]: Comparison of standard gga, gga + u, and hybrid dft calculations," *The Journal of Chemical Physics*, vol. 129, no. 15, p. 154113, 2008.

[173] S. L. Dudarev, G. A. Botton, S. Y. Savrasov, C. J. Humphreys, and A. P. Sutton, "Electron-energy-loss spectra and the structural stability of nickel oxide: an lsda+u study," *Phys. Rev. B*, vol. 57, pp. 1505–1509, Jan 1998.

[174] V. I. Anisimov, F. Aryasetiawan, and A. I. Lichtenstein, "First-principles calculations of the electronic structure and spectra of strongly correlated systems: the lda + u method," *Journal of Physics: Condensed Matter*, vol. 9, no. 4, p. 767, 1997.

[175] G. Kresse and J. Furthmüller, "Efficiency of ab-initio total energy calculations for metals and semiconductors using a plane-wave basis set," *Computational Materials Science*, vol. 6, no. 1, pp. 15 – 50, 1996.

[176] G. Kresse and D. Joubert, "From ultrasoft pseudopotentials to the projector augmented-wave method," *Phys. Rev. B*, vol. 59, pp. 1758–1775, Jan 1999.

[177] J. K. Burdett, T. Hughbanks, G. J. Miller, J. W. Richardson, and J. V. Smith, "Structural-electronic relationships in inorganic solids: powder neutron diffraction studies of the rutile and anatase polymorphs of titanium dioxide at 15 and 295 k," *Journal of the American Chemical Society*, vol. 109, no. 12, pp. 3639–3646, 1987.

[178] C. O'Rourke and D. R. Bowler, "Adsorption of thiophene-conjugated sensitizers on tio2 anatase (101)," *The Journal of Physical Chemistry C*, vol. 114, no. 47, pp. 20240–20248, 2010.

[179] E. Finazzi, C. D. Valentin, G. Pacchioni, and A. Selloni, "Excess electron states in reduced bulk anatase tio[sub 2]: Comparison of standard gga, gga + u, and hybrid dft calculations," *The Journal of Chemical Physics*, vol. 129, no. 15, p. 154113, 2008.

[180] Z. Hu and H. Metiu, "Choice of u for dft+u calculations for titanium oxides," *The Journal of Physical Chemistry C*, vol. 115, no. 13, pp. 5841–5845, 2011.

[181] U. Gesenhues and T. Rentschler, "Crystal growth and defect structure of al3+-doped rutile," *Journal of Solid State Chemistry*, vol. 143, no. 2, pp. 210 – 218, 1999.

[182] U. Gesenhues, "Doping of tio2 pigments by al3+," *Solid State Ionics*, vol. 101Ž013103, Part 2, no. 0, pp. 1171 – 1180, 1997. <ce:title>International Symposium on the Reactivity of Solids</ce:title>.

[183] G. Henkelman, B. Uberuaga, and H. Jónsson, "Climbing image nudged elastic band method for finding saddle points and minimum energy paths," *Journal of Chemical Physics*, vol. 113, no. 22, pp. 9901–9904, 2000.

[184] R. Chen, X. Yang, H. Tian, X. Wang, A. Hagfeldt, and L. Sun, "Effect of tetrahydroquinoline dyes structure on the performance of organic dye-sensitized solar cells," *Chemistry of Materials*, vol. 19, no. 16, pp. 4007–4015, 2007.

[185] P. Hohenberg and W. Kohn, "Inhomogeneous electron gas," *Phys. Rev.*, vol. 136, pp. B864–B871, Nov 1964.

[186] W. Kohn and L. J. Sham, "Self-consistent equations including exchange and correlation effects," *Phys. Rev.*, vol. 140, pp. A1133–A1138, Nov 1965.

[187] E. Runge and E. K. U. Gross, "Density-functional theory for time-dependent systems," *Phys. Rev. Lett.*, vol. 52, pp. 997–1000, Mar 1984.

[188] E. K. U. Gross and W. Kohn, "Local density-functional theory of frequency-dependent linear response," *Phys. Rev. Lett.*, vol. 55, pp. 2850–2852, Dec 1985.

[189] M. E. Casida, *in Recent Developments and Applications of Modern Density Functional Theory*. Amsterdam: Elsevier, 1996.

[190] C. Jamorski, M. E. Casida, and D. R. Salahub, "Dynamic polarizabilities and excitation spectra from a molecular implementation of time-dependent density-functional response theory: N[sub 2] as a case study," *The Journal of Chemical Physics*, vol. 104, no. 13, pp. 5134–5147, 1996.

[191] K. Yabana and G. F. Bertsch, "Time-dependent local-density approximation in real time," *Phys. Rev. B*, vol. 54, pp. 4484–4487, Aug 1996.

[192] D. R. Bowler and T. Miyazaki, "Calculations for millions of atoms with density functional theory: linear scaling shows its potential," *Journal of Physics: Condensed Matter*, vol. 22, no. 7, p. 074207, 2010.

[193] S. Yokojima and G. Chen, "Time domain localized-density-matrix method," *Chemical Physics Letters*, vol. 292, no. 46, pp. 379 – 383, 1998.

[194] S. Yokojima and G. Chen, "Linear scaling calculation of excited-state properties of polyacetylene," *Phys. Rev. B*, vol. 59, pp. 7259–7262, Mar 1999.

[195] S. Yokojima and G. Chen, "Linear-scaling localized-density-matrix method for the ground and excited states of one-dimensional molecular systems," *Chemical Physics Letters*, vol. 300, no. 56, pp. 540 – 544, 1999.

[196] S. Yokojima, D. Zhou, and G. Chen, "Linear-scaling computation of ground state with time-domain localized-density-matrix method," *Chemical Physics Letters*, vol. 302, no. 56, pp. 495 – 498, 1999.

[197] W. Liang, S. Yokojima, and G. Chen, "Generalized linear-scaling localized-density-matrix method," *The Journal of Chemical Physics*, vol. 110, no. 4, pp. 1844–1855, 1999.

[198] W. Liang, S. Yokojima, D. Zhou, and G. Chen, "Localized-density-matrix method and its application to carbon nanotubes," *The Journal of Physical Chemistry A*, vol. 104, no. 11, pp. 2445–2453, 2000.

[199] A. Tsolakidis, D. Sánchez-Portal, and R. M. Martin, "Calculation of the optical response of atomic clusters using time-dependent density functional theory and local orbitals," *Phys. Rev. B*, vol. 66, p. 235416, Dec 2002.

[200] D. R. Bowler and T. Miyazaki, "$\mathcal{O}$(n) methods in electronic structure calculations," *Reports on Progress in Physics*, vol. 75, no. 3, p. 036503, 2012.

[201] E. Prodan and W. Kohn, "Nearsightedness of electronic matter," *Proceedings of the National Academy of Sciences of the United States of America*, vol. 102, no. 33, pp. 11635–11638, 2005.

[202] A. S. Torralba, M. Todorović, V. Brázdová, R. Choudhury, T. Miyazaki, M. J. Gillan, and D. R. Bowler, "Pseudo-atomic orbitals as basis sets for the o(n) dft code conquest," *Journal of Physics: Condensed Matter*, vol. 20, no. 29, p. 294206, 2008.

[203] G. Moore, "Orthogonal polynomial expansions for the matrix exponential," *Linear Algebra and its Applications*, vol. 435, no. 3, pp. 537 – 559, 2011. <ce:title>Special Issue: Dedication to Pete Stewart on the occasion of his 70th birthday</ce:title>.

[204] A. Castro, M. A. L. Marques, and A. Rubio, "Propagators for the time-dependent kohn–sham equations," *The Journal of Chemical Physics*, vol. 121, no. 8, pp. 3425–3433, 2004.

[205] W. Magnus, "On the exponential solution of differential equations for a linear operator," *Communications on Pure and Applied Mathematics*, vol. 7, no. 4, pp. 649–673, 1954.

[206] S. K. Min, Y. Cho, and K. S. Kim, "Efficient electron dynamics with the planewave-based real-time time-dependent density functional theory: Absorption spectra, vibronic electronic spectra, and coupled electron-nucleus dynamics," *The Journal of Chemical Physics*, vol. 135, no. 24, p. 244112, 2011.

[207] J. M. Soler, E. Artacho, J. D. Gale, A. García, J. Junquera, P. Ordejón, and D. Sánchez-Portal, "The siesta method for ab initio order- n materials simulation," *Journal of Physics: Condensed Matter*, vol. 14, no. 11, p. 2745, 2002.

[208] N. N. Matsuzawa, A. Ishitani, D. A. Dixon, and T. Uda, "Time-dependent density functional theory calculations of photoabsorption spectra in the vacuum ultraviolet region," *The Journal of Physical Chemistry A*, vol. 105, no. 20, pp. 4953–4962, 2001.

[209] V. J. Hammond and W. C. Price, "Oscillator strengths of the vacuum ultra-violet absorption bands of benzene and ethylene," *Trans. Faraday Soc.*, vol. 51, pp. 605–610, 1955.

[210] C. Hu, O. Sugino, and Y. Miyamoto, "Modified linear response for time-dependent density-functional theory: Application to rydberg and charge-transfer excitations," *Phys. Rev. A*, vol. 74, p. 032508, Sep 2006.

[211] N. N. Matsuzawa, A. Ishitani, D. A. Dixon, and T. Uda, "Time-dependent density functional theory calculations of photoabsorption spectra in the vacuum ultraviolet region," *The Journal of Physical Chemistry A*, vol. 105, no. 20, pp. 4953–4962, 2001.

[212] M. G. Curtis and I. C. Walker, "Low-energy electron-impact excitation of methane, silane, tetrafluoromethane and tetrafluorosilane," *J. Chem. Soc., Faraday Trans. 2*, vol. 85, pp. 659–670, 1989.

[213] K. Yabana and G. F. Bertsch, "Time-dependent local-density approximation in real time: Application to conjugated molecules," *International Journal of Quantum Chemistry*, vol. 75, no. 1, pp. 55–66, 1999.

[214] J. P. Perdew, K. Burke, and M. Ernzerhof, "Generalized gradient approximation made simple," *Phys. Rev. Lett.*, vol. 77, pp. 3865–3868, Oct 1996.

[215] E. A. Costner, B. K. Long, C. Navar, S. Jockusch, X. Lei, P. Zimmerman, A. Campion, N. J. Turro, and C. G. Willson, "Fundamental optical properties of linear and cyclic alkanes: Vuv absorbance and index of refraction," *The Journal of Physical Chemistry A*, vol. 113, no. 33, pp. 9337–9347, 2009. PMID: 19630422.

[216] M. E. Casida, C. Jamorski, K. C. Casida, and D. R. Salahub, "Molecular excitation energies to high-lying bound states from time-dependent density-functional response theory: Characterization and correction of the time-dependent local density approximation ionization threshold," *The Journal of Chemical Physics*, vol. 108, no. 11, pp. 4439–4449, 1998.

[217] C. Yam, Q. Zhang, F. Wang, and G. Chen, "Linear-scaling quantum mechanical methods for excited states," *Chem. Soc. Rev.*, vol. 41, pp. 3821–3838, 2012.

[218] C. Yam, S. Yokojima, and G. Chen, "Linear-scaling time-dependent density-functional theory," *Phys. Rev. B*, vol. 68, p. 153105, Oct 2003.

[219] A. H. R. Palser and D. E. Manolopoulos, "Canonical purification of the density matrix in electronic-structure theory," *Phys. Rev. B*, vol. 58, pp. 12704–12711, Nov 1998.

[220] A. Fujishima, X. Zhang, and D. A. Tryk, "Tio2 photocatalysis and related surface phenomena," *Surface Science Reports*, vol. 63, no. 12, pp. 515 – 582, 2008.

[221] R. Asahi, T. Morikawa, T. Ohwaki, K. Aoki, and Y. Taga, "Visible-light photocatalysis in nitrogen-doped titanium oxides," *Science*, vol. 293, no. 5528, pp. 269–271, 2001.

[222] B. O'Regan and M. Grätzel, "A low-cost, high-efficiency solar cell based on dye-sensitized colloidal tio2 films," *Nature*, vol. 353, pp. 737–740, 1991.

[223] H. Zhang and J. F. Banfield, "Thermodynamic analysis of phase stability of nanocrystalline titania," *J. Mater. Chem.*, vol. 8, pp. 2073–2076, 1998.

[224] J. M. Pettibone, D. M. Cwiertny, M. Scherer, and V. H. Grassian, "Adsorption of organic acids on tio2 nanoparticles: Effects of ph, nanoparticle size, and nanoparticle aggregation," *Langmuir*, vol. 24, no. 13, pp. 6659–6667, 2008. PMID: 18537279.

[225] N. Satoh, T. Nakashima, K. Kamikura, and K. Yamamoto, "Quantum size effect in tio2 nanoparticles prepared by finely controlled metal assembly on dendrimer templates," *Nat Nano*, vol. 3, pp. 106–111, 2008.

[226] M. Anpo, T. Shima, S. Kodama, and Y. Kubokawa, "Photocatalytic hydrogenation of propyne with water on small-particle titania: size quantization effects and reaction intermediates," *The Journal of Physical Chemistry*, vol. 91, no. 16, pp. 4305–4310, 1987.

[227] S. Monticone, R. Tufeu, A. Kanaev, E. Scolan, and C. Sanchez, "Quantum size effect in tio2 nanoparticles: does it exist?," *Applied Surface Science*, vol. 162¿163, no. 0, pp. 565 – 570, 2000.

[228] D. Pan, N. Zhao, Q. Wang, S. Jiang, X. Ji, and L. An, "Facile synthesis and characterization of luminescent tio2 nanocrystals," *Advanced Materials*, vol. 17, no. 16, pp. 1991–1995, 2005.

[229] V. C. Fuertes, C. F. A. Negre, M. B. Oviedo, F. P. Bonafé, F. Y. Oliva, and C. G. Sánchez, "A theoretical study of the optical properties of nanostructured tio 2," *Journal of Physics: Condensed Matter*, vol. 25, no. 11, p. 115304, 2013.

[230] D. R. Bowler, T. Miyazaki, and M. J. Gillan, "Recent progress in linear scaling ab initio electronic structure techniques," *Journal of Physics: Condensed Matter*, vol. 14, no. 11, p. 2781, 2002.

[231] E. Hernández and M. J. Gillan, "Self-consistent first-principles technique with linear scaling," *Phys. Rev. B*, vol. 51, pp. 10157–10160, Apr 1995.

[232] J. P. Perdew, K. Burke, and M. Ernzerhof, "Generalized gradient approximation made simple," *Phys. Rev. Lett.*, vol. 77, pp. 3865–3868, Oct 1996.

[233] L. S. Blackford, J. Choi, A. Cleary, E. D'Azevedo, J. Demmel, I. Dhillon, J. Dongarra, S. Hammarling, G. Henry, A. Petitet, K. Stanley, D. Walker, and R. C. Whaley, *ScaLAPACK Users' Guide*. Philadelphia, PA: Society for Industrial and Applied Mathematics, 1997.

[234] E. Bitzek, P. Koskinen, F. Gähler, M. Moseler, and P. Gumbsch, "Structural relaxation made simple," *Phys. Rev. Lett.*, vol. 97, p. 170201, Oct 2006.

[235] N. Satoh, T. Nakashima, K. Kamikura, and K. Yamamoto, "Quantum size effect in tio2 nanoparticles prepared by finely controlled metal assembly on dendrimer templates," *Nat Nano*, vol. 3, pp. 106–111, 2008.

[236] R. R. Frontiera, J. Dasgupta, and R. A. Mathies, "Probing interfacial electron transfer in coumarin 343 sensitized tio2 nanoparticles with femtosecond stimulated raman,"

Journal of the American Chemical Society, vol. 131, no. 43, pp. 15630–15632, 2009. PMID: 19860478.

[237] R. Sanchez-de Armas, M. A. San Miguel, J. Oviedo, and J. F. Sanz, "Coumarin derivatives for dye sensitized solar cells: a td-dft study," *Phys. Chem. Chem. Phys.*, vol. 14, pp. 225–233, 2012.

[238] M. B. Oviedo, X. Zarate, C. F. A. Negre, E. Schott, R. Arratia-Pérez, and C. G. Sánchez, "Quantum dynamical simulations as a tool for predicting photoinjection mechanisms in dye-sensitized tio2 solar cells," *The Journal of Physical Chemistry Letters*, vol. 3, no. 18, pp. 2548–2555, 2012.

[239] T. Stein, L. Kronik, and R. Baer, "Prediction of charge-transfer excitations in coumarin-based dyes using a range-separated functional tuned from first principles," *The Journal of Chemical Physics*, vol. 131, no. 24, p. 244119, 2009.

[240] Y. Kurashige, T. Nakajima, S. Kurashige, K. Hirao, and Y. Nishikitani, "Theoretical investigation of the excited states of coumarin dyes for dye-sensitized solar cells," *The Journal of Physical Chemistry A*, vol. 111, no. 25, pp. 5544–5548, 2007.

[241] M. Pastore and F. D. Angelis, "Aggregation of organic dyes on tio2 in dye-sensitized solar cells models: An ab initio investigation," *ACS Nano*, vol. 4, no. 1, pp. 556–562, 2010. PMID: 20020758.

[242] S. Hamad, C. R. A. Catlow, S. M. Woodley, S. Lago, and J. A. Mejías, "Structure and stability of small tio2 nanoparticles," *The Journal of Physical Chemistry B*, vol. 109, no. 33, pp. 15741–15748, 2005.

[243] H. N. Ghosh, "Charge transfer emission in coumarin 343 sensitized tio2 nanoparticle: A direct measurement of back electron transfer," *The Journal of Physical Chemistry B*, vol. 103, no. 47, pp. 10382–10387, 1999.

[244] Z. Guo, W. Liang, Y. Zhao, and G. Chen, "Real-time propagation of the reduced one-electron density matrix in atom-centered orbitals: Application to electron injection dynamics in dye-sensitized tio2 clusters," *The Journal of Physical Chemistry C*, vol. 112, no. 42, pp. 16655–16662, 2008.

[245] A. M. P. Sena, T. Miyazaki, and D. R. Bowler, "Linear scaling constrained density functional theory in conquest," *Journal of Chemical Theory and Computation*, vol. 7, no. 4, pp. 884–889, 2011.